NOTE TO USERS

Juan de Fuca Subducting Plate Geometry and Intraslab Seismicity

Guy Frederick Medema

A dissertation submitted in partial fulfillment
of the requirements for the degree of

Doctor of Philosophy

University of Washington

2006

Program Authorized to Offer Degree: Department of Earth and Space Sciences

UMI Number: 3205869

INFORMATION TO USERS

The quality of this reproduction is dependent upon the quality of the copy submitted. Broken or indistinct print, colored or poor quality illustrations and photographs, print bleed-through, substandard margins, and improper alignment can adversely affect reproduction.

In the unlikely event that the author did not send a complete manuscript and there are missing pages, these will be noted. Also, if unauthorized copyright material had to be removed, a note will indicate the deletion.

University of Washington
Graduate School

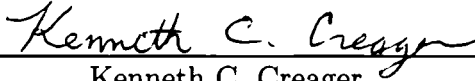This is to certify that I have examined this copy of a doctoral dissertation by

Guy Frederick Medema

and have found that it is complete and satisfactory in all respects,
and that any and all revisions required by the final
examining committee have been made.

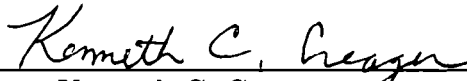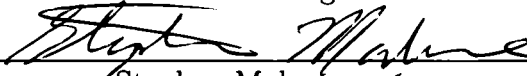Co-Chairs of the Supervisory Committee:

_____

Robert S. Crosson

_____

Kenneth C. Creager

Reading Committee:

_____

Kenneth C. Creager

_____

Stephen Malone

_____

Sean Willett

Date: _____January 12, 2006_____

In presenting this dissertation in partial fulfillment of the requirements for the doctoral degree at the University of Washington, I agree that the Library shall make its copies freely available for inspection. I further agree that extensive copying of this dissertation is allowable only for scholarly purposes, consistent with "fair use" as prescribed in the U.S. Copyright Law. Requests for copying or reproduction of this dissertation may be referred to Proquest Information and Learning, 300 North Zeeb Road, Ann Arbor, MI 48106-1346, 1-800-521-0600, to whom the author has granted "the right to reproduce and sell (a) copies of the manuscript in microform and/or (b) printed copies of the manuscript made from microform."

Signature_____

Date_____01-05-06_____

University of Washington

Abstract

Juan de Fuca Subducting Plate Geometry and Intraslab Seismicity

Guy Frederick Medema

Co-Chairs of the Supervisory Committee:
Professor Robert S. Crosson
Department of Earth and Space Sciences

Professor Kenneth C. Creager
Department of Earth and Space Sciences

The geometry of the subducting Juan de Fuca plate beneath the Olympic Peninsula of Western Washington is modeled using wide-angle P_mP reflections off the slab Moho. Active-source reflection data collected from the 1998 WET SHIPS project were augmented with earthquake-source reflections to increase the spatial distribution of reflection points over the Juan de Fuca arch structure. Approximately 1100 WET SHIPS and 500 earthquake-source reflections were used in our inversion. P_mP travel-times from active sources and $P_mP - P$ differential times from earthquakes sources were simultaneously inverted for slab-Moho depth, using a combination of finite-difference and 3-D ray-tracing methods. Results show a tighter arch structure than in previous models with the shallowest dipping portion ($\sim 10°$ dip) concentrated directly beneath the Olympic Mountains. Comparison of our slab model to intraslab earthquake hypocenters reveals a southwest-northeast trending lineament of seismicity situated just beneath the subducted Moho in the slab mantle. We interpret this seismicity as the manifestation of a subducting pseudofault along which high levels of upper mantle hydration occurred prior to subduction. Most of the remaining intraslab seismicity is concentrated on the northern and southern flanks of the arch

and is likely due to increased strain rates in these regions from the combined effect of slab arch and subsequent steepening of slab dip. Earthquakes in the northern region appear to occur above the slab Moho in the crust of the oceanic plate, while uncertainties in earthquake locations and 3-D velocities in the southern region prevent an unambiguous interpretation at this time. The southern patch is especially important as it contains 3 large (magnitude 6.5 to 7.1) earthquakes during that past 60 years, including the 2001, Mw 6.8, Nisqually earthquake. Earthquakes occurring between 45 and 65 km depth in these two regions also systematically produce an anomalous low-frequency, high-amplitude secondary P arrival on updip stations with an average horizontal velocity of 6.0 km/s. We identified 13 earthquakes producing this anomalous phase. These arrivals are typically observed for rays that pass under the Olympic Mountains. 2-D ray-tracing was used to interpret travel times of these arrivals as S-to-P conversions at the interface between the top of the subducted oceanic crust and mantle wedge. Efficient conversion from S-to-P required high velocity oceanic crust and an anomalously low velocity mantle wedge. We therefore interpret this secondary phase to indicate eclogitization of the oceanic crust and serpentinization of the mantle wedge in the vicinity of earthquakes producing the phase. Along paths where these phases are observed, 3-D tomography models exhibit a dipping low-velocity zone formed by accretionary sediments underthrusting high-velocity Eocene volcanics. 2-D ray tracing indicates that this acts as a wave guide along which high-amplitude, low-frequency waves can propagate great distances to the seismic stations.

TABLE OF CONTENTS

i

LIST OF FIGURES

LIST OF TABLES

ACKNOWLEDGMENTS

DEDICATION

In Memory of
Anthony Qamar

Chapter 1

INTRODUCTION

Ever since *McKenzie and Parker* (1967) first suggested that crust is being "destroyed" at the margin between the Juan de Fuca microplate and North America, there has been tremendous interest within the scientific and seismic hazard communities regarding the Juan de Fuca (Cascadia) subduction zone (CSZ). Arguably, the most interesting section of the subducting slab is in the vicinity of a bend in the plate margin off the coast of Washington state (Figure 1.1). The bend causes a warp or "arch" in the plate to conserve volume making this the most geometrically complex section. Furthermore, the highest rate of onshore intraslab seismicity occurs in this region, sharply decreasing to the north and south (Figure 1.3). In this study, we address two fundamental questions regarding the Juan de Fuca subduction zone in this region: 1) "What is the geometry of the plate as it subducts?" and 2) "What is the nature of the intraslab seismicity?".

We modeled the plate geometry by inverting wide-angle reflections off the subducted slab moho from active and earthquake sources. By including earthquake data, we improved the geometry model along the poorly constrained southern flank of the arch, displaying a more narrow arch than suggested in previous models. We then compared our model with earthquake hypocenters to place them either above or below the moho. Doing so revealed distinct patterns in the distributions of the two types. Earthquake above the moho occur primarily on the flanks of the arch between 45 and 60 km depth, where the slab dip begins to steepen, while most of earthquakes below the moho lie along a northeast trend, coincident with a subducted pseudofault.
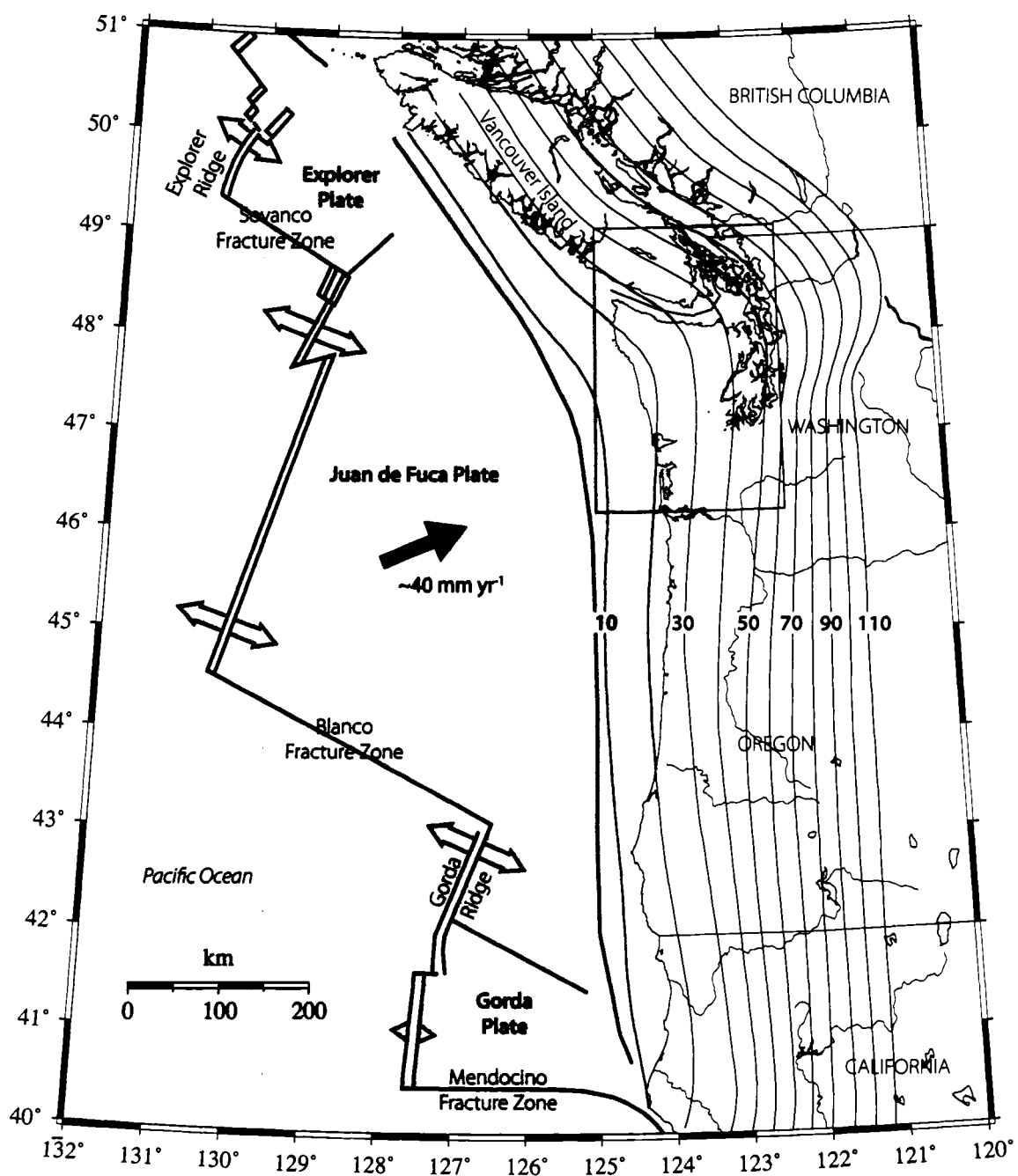
Figure 1.1: Map of Cascadia Subduction Zone. The Juan de Fuca plate is obliquely subducting beneath the North American plate to the northeast at approximately 40 mm yr^{-1}. Depth contours to top of JDF plate are indicated (*McCrory et al.*, 2004). Red box indicates our approximate region of study.

Preston et al. (2003a) concluded that earthquakes occurring in the crust are the result of the basalt to eclogite phase change and the upper mantle events are due to dehydration embrittlement of upper mantle peridotite (*Kirby et al.*, 2002). Since basalt to eclogite must occur everywhere in the downgoing crust, we propose that increased stress in the upper plate caused by a combination of slab arch and increased dip is allowing this phase change to occur seismically. With regard to the upper mantle seismicity, we propose that excess upper mantle hydration along the pseudofault prior to subduction is manifesting as high seismicity rates along the observed lineation.

Finally, a strong secondary P wave is observed from a small number of intraslab earthquakes, but only on Olympic Peninsula stations. We used 2-D ray-tracing to model these arrivals as SP conversions at the plate-mantle wedge interface that are then guided by a low-velocity layer formed by accreted sediments underthrusting high-velocity Eocene basalts.

1.1 Cascadia Tectonics

The Juan de Fuca microplate lies off the coast of the Pacific Northwest (Figure 1.1) and is the last remnant of the subducted Farallon plate, becoming an independent plate when the Farallon ridge collided with North America about 20 Ma (*Riddihough*, 1984). It extends approximately 1000 km from the Mendicino triple junction off northern California to the Explorer microplate off the northwest coast of Vancouver Island and is currently subducting obliquely beneath the North American plate at an estimated convergence rate of $\sim$40 mm yr^{-1}. Convergence direction estimates average $\sim$N60E (*Riddihough*, 1984; *DeMets et al.*, 1990; *Wilson*, 1993, 2002). The strike of the plate margin is nearly north-south off the California-Oregon coast changing to northwest-southeast off Vancouver Island. To conserve volume as the plate bends, it arches upward primarily beneath western Washington (*Crosson and Owens*, 1987; *Weaver and Baker*, 1988; *Michaelson and Weaver*, 1986).

1.2 Previous Juan de Fuca Plate Modeling

The existence of a Wadati-Benioff zone beneath western Washington was first demonstrated by *Crosson* (1977) and later refined by *Taber and Smith* (1985) revealing a slab dipping easterly at 10-12° to approximately 50 km depth where seismicity suggests an increase in dip (*Crosson*, 1977, 1983; *Taber and Smith*, 1985). Seismicity, where it exists, can give a first-order slab geometry model, but this assumes earthquakes always occur in the same relative position in the slab (e.g. in the oceanic crust) which breaks down if earthquakes are occurring in both the oceanic crust and upper mantle. Several other methods for modeling the slab have therefore been used.

Results from teleseismic P-wave residual analysis agree with a shallow slab dip beneath western Washington, steepening to ~45-55° east of Puget Sound (*Lin*, 1973; *Michaelson and Weaver*, 1986). A number of offshore and offshore-onshore active experiments have constrained the slab depth and dip below the margin and coastal regions at several latitudes (e.g., *Tatel and Tuve*, 1955; *Taber and Lewis*, 1986; *Flueh et al.*, 1998; *Calvert and Clowes*, 1990; *Parsons et al.*, 1998). Land-based active source transects have also added to slab constraint and velocity structure of the forearc (*Trehu et al.*, 1994; *Miller et al.*, 1997) although slab Moho reflections from active sources are not generally observed below ~ 40 km depth (*Brocher et al.*, 2003). Passive source arrays for receiver function analysis have been used on Vancouver Island (*Cassidy and Ellis*, 1993), southwest Washington (*Owens et al.*, 1988; *Lapp et al.*, 1990) and notably in central Oregon where a dense, east-west 2D transect extending from the coast into the backarc shows a low-velocity layer, presumed to be oceanic crust, extending down to ~ 40 km (*Bostock et al.*, 2002). The SHIPS active source project in 1998 produced wide-angle reflections off the slab Moho beneath the northern part of the Olympic Peninsula and Strait of Juan de Fuca (*Trehu et al.*, 2002) which were used in slab model inversions (*Trehu et al.*, 2002; *Preston*, 2003b). Finally, *McCrory et al.* (2004) started with a slab geometry derived from a 3D dislocation

model *Flück et al.* (1997) then made adjustments according to seismicity profiles, active and passive source experiments, and a resistivity profile (*Wannamaker et al.*, 1989) to produce a composite slab model along the entire strike. Contours from the McCrory model are shown in Figures 1.1 and 1.4.

To accommodate the "excess" slab material caused by the landward convex plate boundary off the coast of Washington, several possible models were considered by *Rogers* (1983). Rogers argued that densification of the oceanic crust and upper mantle due to phase changes between 40 and 70 km could absorb the excess volume such that no bending or warping of the plate would be necessary in this depth range. At shallower and deeper depths where phase changes were presumed to not take place, plate warping (arching) was suggested as the mode of accomodation.

Chiao and Creager (2002) used membrane strain modeling to predict slab geometry based on strain rate accomodation. They concluded that an arch approximately where one is observed reduces the necesary amount of strain accomodation to levels in agreement with observed seismic moment release. Their model also predicts a $10-12°$ dipping slab beneath the Olympic Mountains (Figure 1.2), in very good agreement with our geometry model.

Michaelson and Weaver (1986) first showed evidence of such an arch from tele-seismic P-wave residual analysis, concluding that slab dip transitions from southeast beneath southwest Washington to northeast beneath the northern Puget Sound region and that the dip shallows in the center part of the slab. Further evidence came from receiver function analyses in southwest Washington that showed a southeasterly dipping slab, consistent with being on the southern flank of an arch (*Crosson and Owens*, 1987; *Owens et al.*, 1988; *Lapp et al.*, 1990). Additional support for an arch came from detailed intraslab earthquake hypocenter analysis (*Weaver and Baker*, 1988).

In their model, *Michaelson and Weaver* (1986) suggested a possible upward warping of the plate on the northern flank but a slab tear on the southern flank. A slab tear
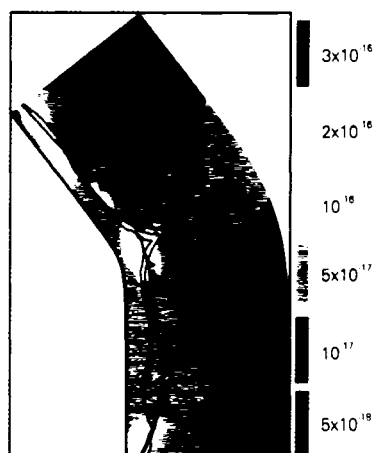
Figure 1.2: Strain rates predicted from membrane strain modeling (*Chiao and Creager*, 2002). The model predicts an arch in the slab, dipping 10 − 12° beneath the Olympic Mountains. 10 and 12° dip contours are shown.

roughly coinciding with the southern limit of intraslab seismicity near 47° has also been suggested by *McCrory et al.* (2001) but to date has not been shown conclusively.

1.3 Seismicity

The Cascadia system is classified as a young, warm subduction environment, being only ∼9 Ma at the trench (*Kirby et al.*, 2002; *Wilson*, 2002). As is typical in young, warm subduction zones, e.g. Nankai in SW Japan (Philippine plate) and Southeast Costa Rica (Cocos plate), Cascadia intraslab seismicity is sparse and confined to shallow depths (< 100 km). Intraslab earthquakes are distributed into two bands (Figure 1.3) (*Rogers and Crosson*, 2002). One band with hypocenters < 40 km depth runs beneath the Vancouver Island coast, extending to the Olympic Peninsula. The other is beneath Puget Sound and the Strait of Georgia having hypocenters between 40 and 70 km (Figure 1.4) with the highest activity rate occurring between 40 and 50 km (Figure 1.5). Very little seismicity below 70 km depth exists, but a lineament of small events extends to depths near 100 km east of Puget Sound.
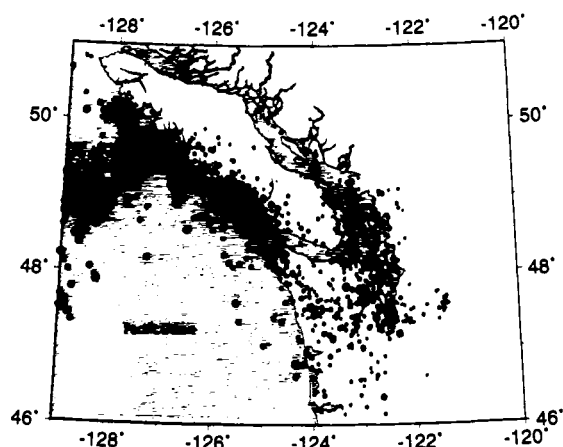
Figure 1.3: Cascadia intraslab seismicity map (*Rogers and Crosson*, 2002). Earthquakes (red circles) occur in two bands. The shallower band is predominantly along the west coast of Vancouver Island and extends southward to the Olympic Peninsula where it appears to merge with the deeper band. The deeper band is concentrated beneath Puget Sound and the Georgia Strait. The deeper band contains the largest recorded Cascadia intraslab events.

1.4 Seismic Hazards

Cascadia is the only active subduction zone in the continental U.S and Canada and, as is common for subduction zones globally, is directly beneath heavily populated areas (*Bebout et al.*, 1996) (e.g. Vancouver, British Columbia; Seattle, Washington; Portland, Oregon). The recent megathrust event off the coast of Sumatra (December 26, 2004; $M_w9.3$) and the resulting tsunami killed nearly 300,000 people and displaced over 1 million (*http://www.eeri.org*), increasing concern about the possibility and potential hazards of a similar event in the Pacific Northwest. For comparison, Figure 1.6 shows the Sumatra rupture surface relative to the CSZ. While no interplate earthquakes have been recorded from instrumentation in the CSZ, there are several lines of evidence to support recurring megathrust events, most recently a M9.0 (estimated) (*Satake et al.*, 2003) in 1700, with an average recurrence interval ~600 yrs (*Goldfinger et al.*, 2003).

8
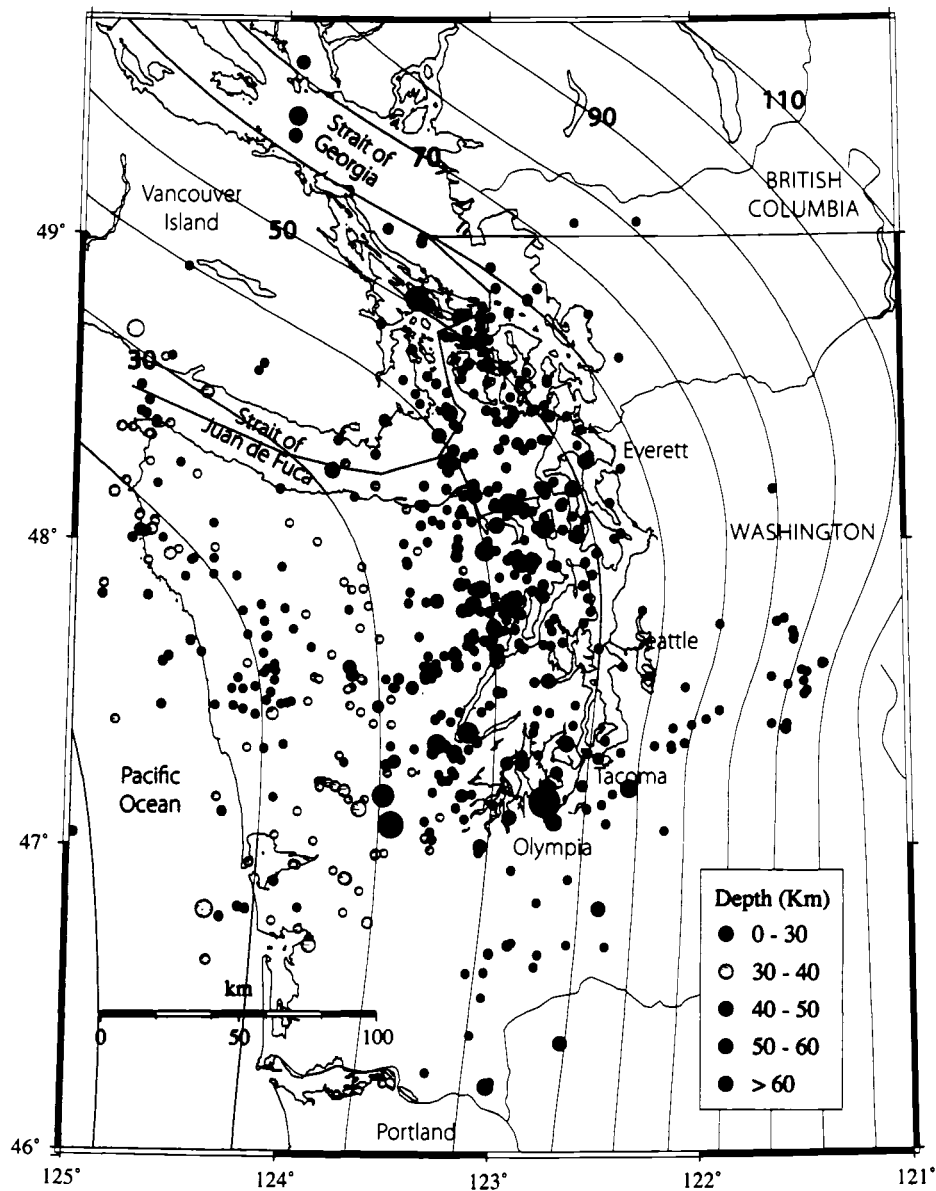
Figure 1.4: Intraslab seismicity (circles) beneath Western Washington color coded by depth. Depth contours are to the top of the dubducted plate (*McCrory et al.*, 2004). Seismicity rates drop sharply south of Olympia and is virtually nonexistent beneath Oregon. Very little seismicity occurs below 60 km depth but a NE trending lineament extends to 100 km depth east of Seattle.
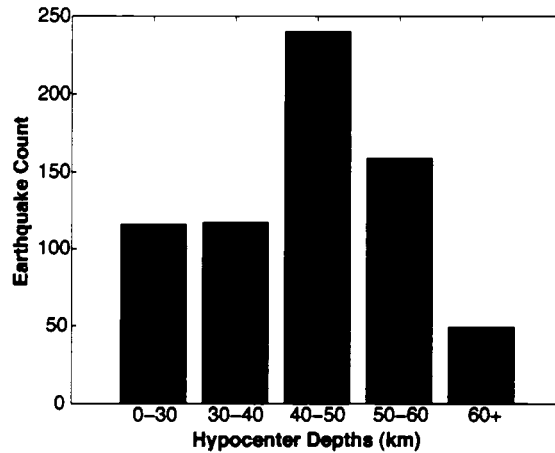
Figure 1.5: Depth distribution of Cascadia intraslab earthquakes beneath Western Washington (Figure 1.4) from 1980 to 2004.

An important reason for having good slab geometry models is that critically reflected P_mP waves from a Cascadia megathrust event have been predicted to produce significant ground motion (*Cohee et al.*, 1991; *Shragge et al.*, 2002; *McNeill et al.*, 2004). Focusing or defocusing effects on these reflections might be expected due to the arching geometry of the plate. Improved ground motion modeling from P_mP energy is therefore inherently related to the accuracy of the reflector model used.

In addition to megathrust events, large (>M6) intraslab earthquakes occur in the CSZ approximately every 30 years, e.g. 1949 M7.1 (*Baker and Langston*, 1987), 1965 M6.5 (*Langston and Blum*, 1977), 2001, M6.8 (*Pacific Northwest Seismograph Network*). These events, while smaller in magnitude than megathrusts, occur directly beneath population centers and recur at an order of magnitude higher rate, making them a considerable hazard to life and property in the Pacific Northwest. Indeed, the 2001 Nisqually earthquake caused ~400 injuries and an estimated $2 billion in damage[1] (*http://www.eeri.org*).

---

[1]Approximately 1/3 of this estimate is from inspection and repairs to the Alaska Way viaduct, a mile-long elevated double-deck highway through downtown Seattle. Completed in 1952, the aging structure is considered to be at risk of failure during another large earthquake in the region,
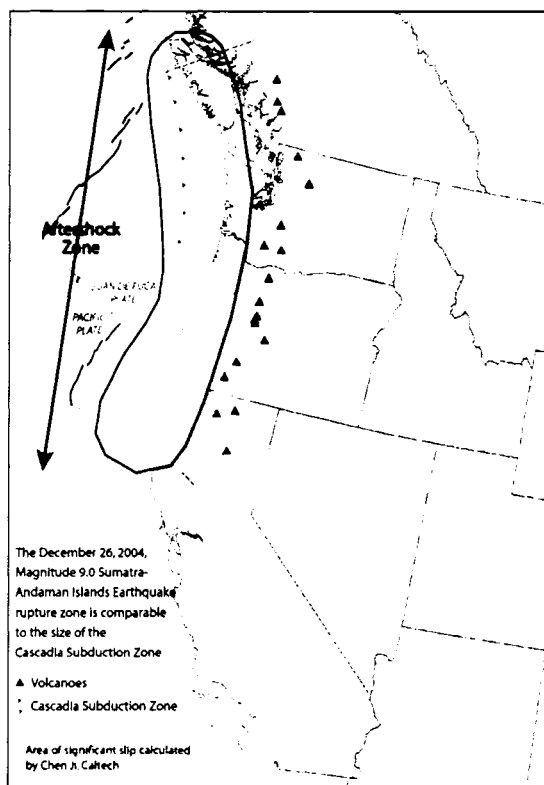
Figure 1.6: 2004 M_w9.3 Sumatra megathrust earthquake rupture are compared with Cascadia subduction margin. This demonstrates the potential for a similar magnitude event in Cascadia.

As previously stated, Cascadia intraslab earthquakes occur in both the subducted oceanic crust and upper mantle (*Preston et al.*, 2003a; *Cassidy and Waldhauser*, 2003) although uncertainty in slab models and hypocenter locations prevents making this distinction for all earthquakes. In order to understand the nature of Cascadia intraslab seismicity, it is important to make this distinction as the mechanisms and conditions for seismicity in the two regions are different (e.g., *Kirby et al.*, 1996; *Wang and Rogers*, 1994; *Wang*, 2002; *R. et al.*, 2003b). This has hazard implications in terms of upper magnitude limits. If the largest events rupture entirely within

similar to the San Francisco-Oakland Bay Bridge collapse during the 1989 Loma Prieta earthquake [*http://www.wsdot.wa.gov*].

the oceanic crust, physical dimensions limit magnitudes to approximately 7 (*Preston et al.*, 2003a) but no such geometric limits exist if rupture occurs either entirely or partially in the upper mantle. According to the magnitude-recurrence model from the Geological Survery of Canada, maximum magnitudes for Cascadia intraslab events are M7.3 $\pm$ 0.3 if rupture extends into the mantle (*Adams and Halchuk*, 2000).

The largest recorded Cascadia intraslab earthquakes over the last century, including the 2001 Nisqually M6.8 event, have occurred below the southern end of Puget Sound. The Nisqually earthquake locates very near the slab moho and it is not clear if it ruptured in the crust, the mantle, or both. This is a fundamental question. Where in the slab are the largest Cascadia intraslab occurring? We present evidence that in the regions containing the largest events, earthquakes predominantly occur in the oceanic crust. We cannot, however be certain that the largest events (e.g. Nisqually) are entirely confined to the crust.

Chapter 2

SLAB GEOMETRY: DATA AND ANALYSIS METHODS

2.1 Introduction

P_mP reflections off the Juan de Fuca slab were observed beneath the upper Olympic Peninsula and Strait of Juan de Fuca from the 1998 SHIPS experiment (*Trehu et al.*, 2002)(Figure 2.1). *Trehu et al.* (2002) and *Preston et al.* (2003a) inverted these data for reflector depth, showing a northeast dipping slab consistent with the northern flank of the arch. Unfortunately, P_mP was not observed from SHIPS further south to include the top and southern flank of the arch. As we attempt to understand the nature of western Washington intraslab seismicity, e.g. the localization of the largest intraslab earthquakes beneath southern Puget Sound and the sharp decrease in seismicity beneath southwest Washington and Oregon, it is important to constrain this portion of slab position and geometry. For example, strain rates within the plate vary with geometry (*Chiao and Creager*, 2002) and presumably influence seismicity rates. Differentiating earthquakes that occur in the oceanic crust from those in the upper mantle is also fundamental to understanding seismicity as the mechanisms in each regime differ (Chapter 1). Therefore, for this study we collected P_mP observations from regional earthquakes occurring between 1980 and 2003 to augment the existing reflection data set and extend the slab model to include more of the afore mentioned region.

2.2 Data

I examined approximately 3000 regional earthquakes that occurred between 1980 and 2003 and identified, $\sim$950 P_mP arrivals from $\sim$300 earthquakes. An addtional 93
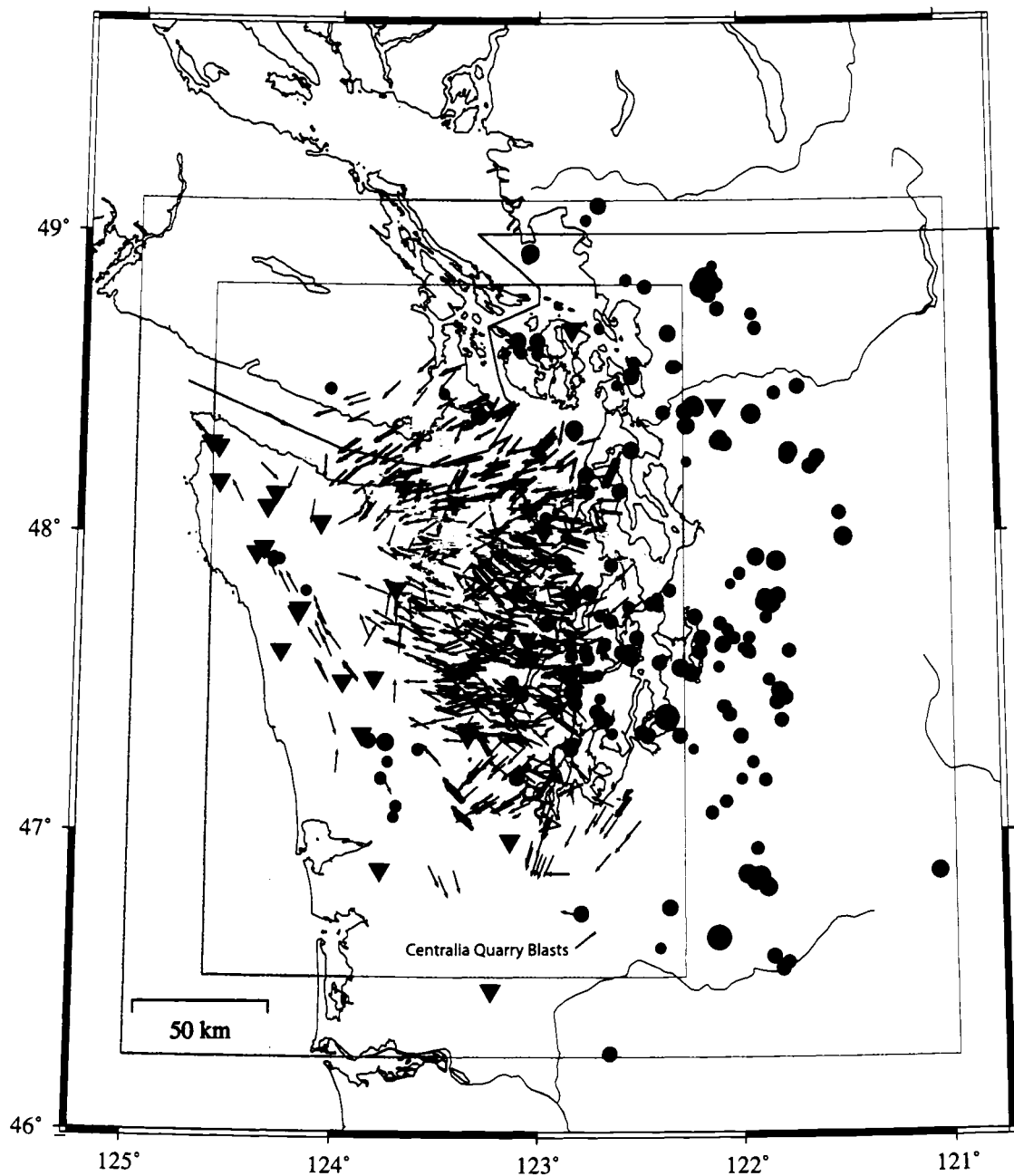
Figure 2.1: Crustal earthquakes (red circles) from 1990 to 2003 producing wide-angle reflections off the Juan de Fuca slab on PNSN stations (green triangles). Midpoints are plotted (blue arrows) to approximate reflection points with arrow direction indicating source to receiver azimuth. SHIPS wide-angle relfections are shown as yellow plus symbols. Outer red box indicates velocity model boundaries. Inner box indicates our reflector model inversion area. Addition of earthquake data allows a southward extension of the slab model to include the southern flank of the arch.

observations were made from quarry blasts near Centralia, Washington, 122.76W, 46.70N (Figure 2.1). To eliminate origin time uncertainty inherent with earthquake data, we used the differential times, P_mP - P, which is sensitive to reflector depth but not origin time. P_mP - P is also sensitive to earthquake location, particularly depth, so, where available, we used hypocenters relocated using the same 3-D velocity model used for travel-time computation. P and P_mP phase times were hand-picked. Sources and receivers were required to be within the velocity model space and earthquakes deeper than 30 km were excluded to avoid inclusion of intraslab events. Because correct identification of the secondary arrivals as P_mP is fundamental to the meaningfulness of the resultant reflector model, some discussion of that evidence is presented here.

Figure 2.2 is a record section of a mid-crustal earthquake that produced clear secondary arrivals on four Olympic Peninsula stations. Travel-time curves predicted from a simple dipping reflector model show agreement with the phase time picks, and the energetic nature of the phase is characteristic of critical reflections. Critical reflections require an increasing velocity discontinuity. Receiver function analysis of a 2-D transect across the forearc in central Oregon shows the largest positive velocity gradient as a dipping layer between 30 and 50 km depth, interpreted as the Juan de Fuca moho (*Bostock et al.*, 2002) (Figure 2.3). We therefore assume our observed reflections are off the moho, at the base of the oceanic crust.

I compared observed $P_mP - P$ times to those predicted using the reflector and velocity model of *Preston et al.* (2003a) to validate our P_mP interpretation. Figure 2.4 displays the travel-time residuals $((P_mP - P)_{obs}) - (P_mP - P)_{pred})$ using the Preston model and shows overall agreement with a mean of 0.08 s and rms of 0.47 s. A 0.5 s residual corresponds to approximately a 3-4 km difference in reflector depth, based on typical travel-time derivatives (Section 2.3.5), so it is reasonable to assume the bulk of our observations are correctly interpreted as P_mP rather than reflections off some other interface, e.g. a mid-crustal reflector. We compared residuals for reflections in
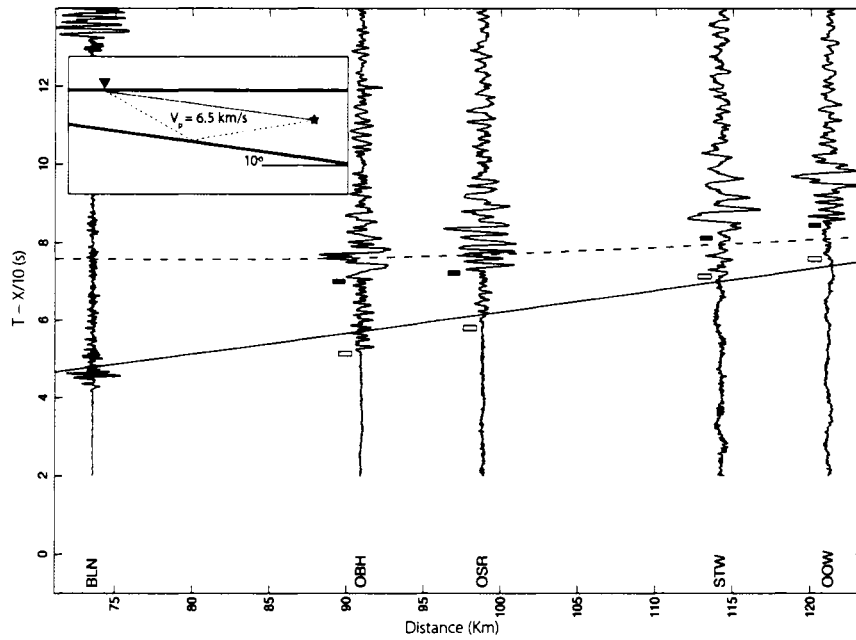
Figure 2.2: Sample record section from midcrustal earthquake to Olympic Peninsula stations showing prominent slab moho reflections (P_mP). First and secondary arrivals are denoted by open and solid bars, respectively. The solid and dashed lines are direct and reflected travel-time curves, respectively, computed using the simple model shown (inset) and support a P_mP interpretation.

the northern half of our model area where the Preston model has data constraint with those in the previously unconstrained southern half. Rms values is both regions are approximately 0.47 s but the southern data residuals have a positive bias (mean) of 0.23 s corresponding to an approximately 2 km deeper model.

As a final test, as sources are closer to the reflector (deeper), $P_mP - P$ should decrease and be observed at nearer stations. Figure 2.5 shows $P_mP - P$ times plotted against source-receiver distance, binned by vertical distance (approximate) from source to reflector and in general shows the expected behavior.
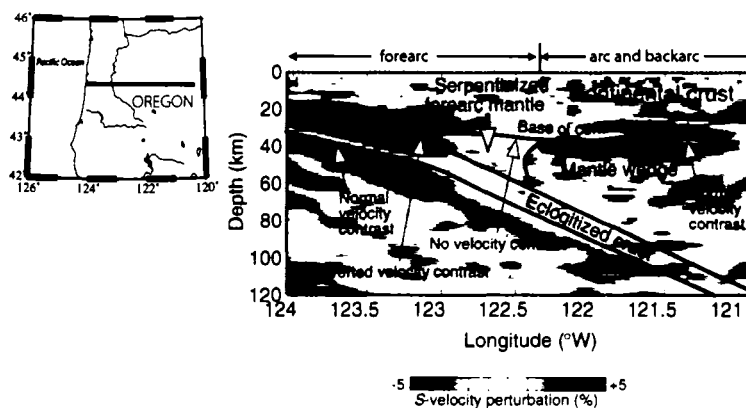
Figure 2.3: Receiver function results showing velocity perturbations from a standard 1-D model for an E-W transsect across central Oregon (red line on map) (modified from *Bostock et al.* (2002)). The largest positive velocity contrast (red over blue) in the forearc is a dipping interface interpreted as the Juan de Fuca moho.

2.2.1 Active Source Data

The SHIPS experiment produced ~1100 high-quality P_mP reflection times using slant-stacked seismograms (*Preston et al.*, 2003a) that were included in this study (Figure 2.1). *Preston et al.* (2003a) used these data as part of a joint inversion for velocity structure, hypocenter locations and reflector depth. Because source location and origin time are known precisely, absolute P_mP travel times are known and we need not use the $P - P_mP$ differential times.

2.2.2 Data Uncertainty

Picking errors resulted from secondary phase misidentification and uncertainty in phase onset. Phase misidentification is potentially the most egregious source of error as doing so assigns a Moho reflection between a source and receiver where perhaps none exists. Many of these data were culled, however, during the inversion process as anomalously high data residuals were identified. For the earthquake data, pick uncertainties due to uncertainty in phase onset averaged 0.08 s and 0.13 s for P and
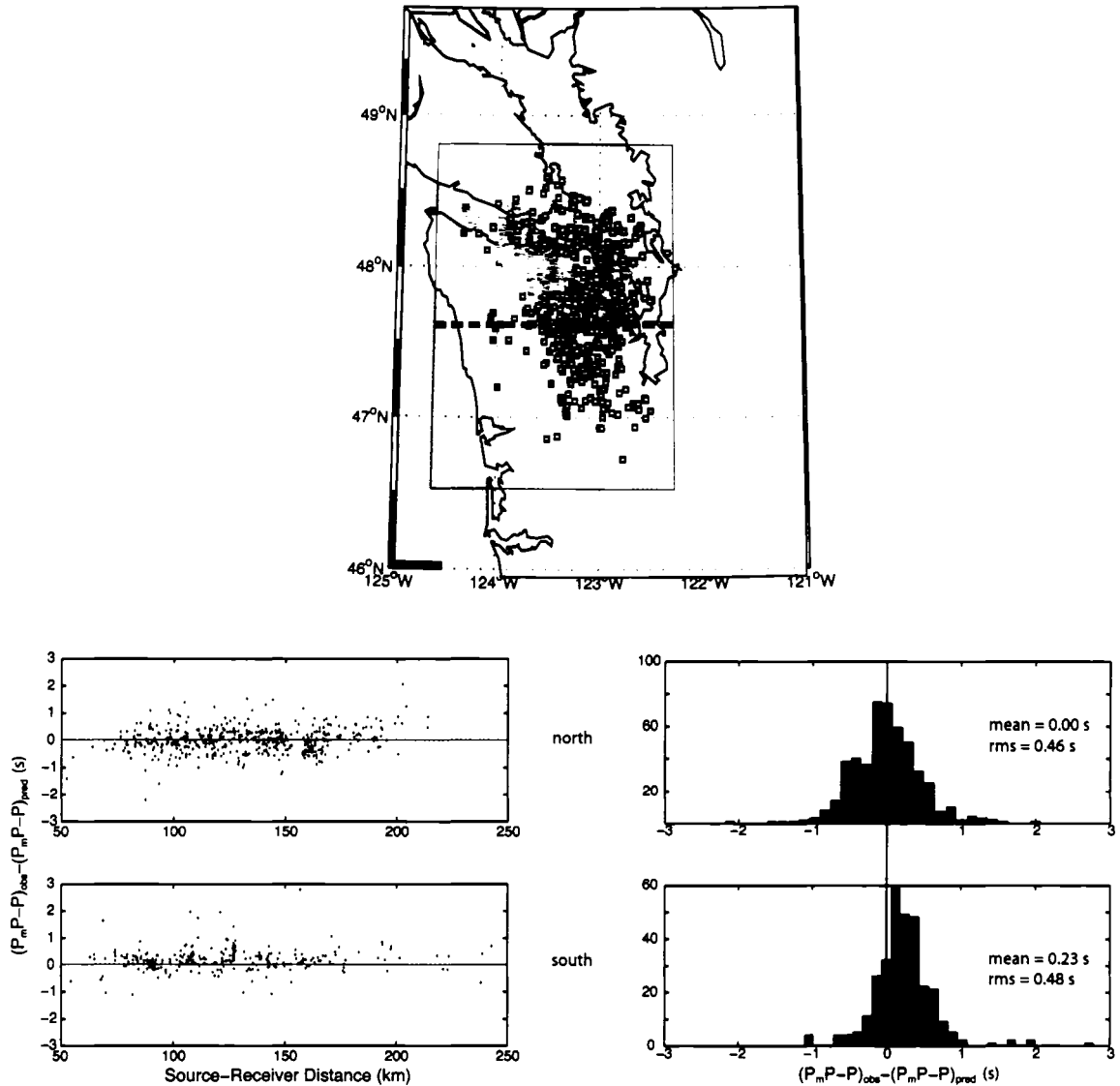
Figure 2.4: (top) $(P_m P - P)_{obs}) - (P_m P - P)_{pred}$ residuals using the velocity and reflector model of *Preston et al.* (2003a) are shown as colored squares. Blue and red squares indicate positive and negative residuals, respectively. A positive residual ($t_{obs} > t_{pred}$) suggests a deeper reflector. SHIPS reflections are shown (yellow plus-symbols). (bottom) Residuals plotted against source-receiver offset (left). Bar graphs (right) indicate mean and rms values for north and south subsets. Positive bias in southern data indicates a deeper slab than the Preston model.
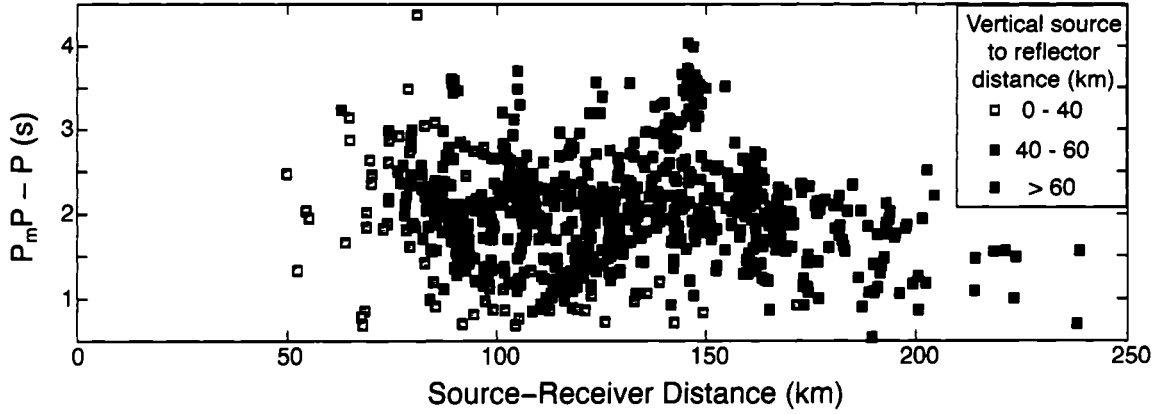
Figure 2.5: $P_mP - P$ times binned by approximate vertical distance above reflector assuming a 15° eastward dipping reflector plane. Earthquakes closest to the reflector (yellow) produce wide-angle reflections at the shortest offsets and $P_mP - P$ times are generally less than for earthquakes farther from the reflector (green and red). A decrease in $P_mP - P$ for each group is also observed with offset distance. These trends are all consistent with reflected arrivals.

P_mP, respectively. While summation of the uncertainties for P and P_mP to estimate total uncertainty is not strictly correct in a statistical sense, it is not unreasonable to assume an average uncertainty of $\approx 0.2s$, given that pick uncertainties were likely underestimated. For the SHIPS data, an uncertainty of 0.10 s was estimated for all P_mP picks.

2.3 Inversion Process

A Moho surface model, **m**, of the subducted Juan de Fuca slab beneath western Washington is sought using differential travel times $P_mP - P$ from earthquake sources and absolute P_mP times from SHIPS active source data. Our non-linear inversion determines the smoothest (minimum Laplacian) slab moho model that adequately satisfies the wide-angle reflection times weighted by their uncertainties. We used a 3-D velocity model (*Preston et al.*, 2003a) and earthquake locations determined using that model when available and standard catalog locations otherwise. We used

a finite-difference solution to the Eikonal equation to calculate P times and a 2-point ray-shooting method to calculate P_mP times. Cholesky decompositon was used to solve a linear system at each iteration for the change vector $\delta\mathbf{m}$ that was added to the model of the previous iteration.

2.3.1 Travel-Time Calculations

To calculate times for first arrivals we used used a finite-difference method for solving the Eikonal equation based on the algorithm by *Vidale* (1990) and computer code by Zelt [year]. Reciprocity allowed the computation of travel-time grids from stations rather than sources and trilinear interpolation was then used to find travel times to each earthquake. I implemented a 3-D ray-tracing program called Trabox, coded by Malcolm Sambridge and based on the algorithm in *Sambridge and Kennett* (1990). Initial rays are traced through a 3-D gridded velocity model to the horizontal plane of the receiver then a modified Newton's method algorithm adjusts the ray parameter until target convergence is achieved or a maximum iteration limit is exceeded. Trabox computes reflected and transmitted rays at an arbitrary interface defined as depths on an x-y grid. I modified the code to compute only reflected rays and to reject rays that converge on the target but did not reflect.

Because of significant lateral heterogeneity in the velocity model, target convergence failed for > 50% of the source-receiver combinations, even when the reflector was a dipping plane. After much trial-and-error, I implemented an algorithm that sprays a cone of rays about the source-receiver azimuth then stores the 10 reflecting rays nearest the receiver. Newton's method was then attempted with each of these as initial rays. This improved convergence to > 95% for the starting model (dipping plane), decreasing to ~ 80% as the reflector geometry became more complex.

The convergence tolerance was set to 50 m, but if the maximum allowed iterations of Newton's method was exhausted without convergence, the nearest ray found during that attempt was examined. If it landed within 5 km, it was saved and included in

the final travel-time solution. For each saved ray (those within 5 km) a plane-wave assumption was made to compute the travel time at the target (station) using the ray parameter and backazimuth to the target. For a given source-receiver pair, the differences between travel-times of convergent rays and those interpolated from 5 km away using a plane-wave assumption were typically 0.01 to 0.03 s. This range is well within the uncertainty of our picks so allowing rays within 5 km proved reasonable. These travel times were then summed in a weighted average, linearly weighted by distance^{-1} to the target. Likewise, a weighted average of reflection points was also computed.

2.3.2 Model Parameterization

The reflector model is parameterized as depths on an x-y grid in a left-hand system (+x = east). Grid spacing was defined by placing a 102 x 107 node grid on the velocity model space used for travel-time calculations (Figure 2.1). The velocity model has origin at (125.0W, 46.25N) and extends 302 km east and 318 km north using a UTM projection resulting in grid spacing $\Delta l = 3.0$ km. To reduce computational expense and the size of the null space from unsampled grid squares, a subset of this grid large enough to include all reflection points was selected for the model space to be inverted for. A 60 x 85 node grid with origin at 124.6190W, 46.5260N and $\Delta l = 3.0$ km therefore defines the modeled reflector surface.

2.3.3 Governing Equations

In general, travel time from source to receiver for a reflected ray, r, is given by the analytic equation

$$t_r = \int_{S_r} u(\mathbf{x})d(\mathbf{x}) \tag{2.1}$$

where $u(\mathbf{x}) \equiv$ slowness (1 divided by the compressional wave speed) at $\mathbf{x}$ along raypath S_r. Given a reflector depth model $\mathbf{m}$, t_r is non-linear in $\mathbf{m}$ for non-vertical raypaths

as can be easily seen for the simple case of a sub-parallel reflector at depth Z in a medium of constant slowness U and source-receiver distance X.

$$T_r = 2U\sqrt{Z^2 + \frac{X^2}{4}}$$

This nonlinearity necessitates an iterative inversion. Equation 2.1 is therefore linearized in the usual way with a first-order Taylor expansion.

$$t_r(\mathbf{m}) = \int_{S_r(\mathbf{m}_o)} u(\mathbf{x})d\mathbf{x} + \frac{dt_r}{d\mathbf{m}}\delta\mathbf{m} \tag{2.2}$$

and if we recognize that the left side is an observed travel time and the integral term is a predicted travel time for reflector model $\mathbf{m_o}$, then rearranging terms gives

$$\frac{dt_r}{d\mathbf{m}}\delta\mathbf{m} = t_{obs} - t_{pred} \tag{2.3}$$

where t here is generic, either representing absolute reflection travel times (SHIPS reflections) or reflected minus first-arrival times (earthquake reflections). Equation 2.3 is constructed for each observation, producing a linear system from which we may solve for the model correction, $\delta\mathbf{m}$. An updated model is then produced by adding $\delta\mathbf{m}$ to the previous model iteration or $\mathbf{m}^i = \mathbf{m}^{i-1} + \delta\mathbf{m}$. Computation of the travel-time derivatives and construction of the linear system is described in Section 2.3.5.

2.3.4   a priori Constraints

The edges of our model were constrained by interpolation of the slab model by *McCrory et al.* (2004) at 3 km intervals along each edge. Implementation of *a priori* point constraints was achieved by including equations of the form

$$\delta\mathbf{m} = \mathbf{m}_c - \mathbf{m}^{i-1} \equiv \delta c \tag{2.4}$$

where

   $\mathbf{m}_c \equiv$ constraint depth

   $\mathbf{m}^{i-1} \equiv$ model depth from last iteration.

   Construction of these equations is also discussed in Section 2.3.5.

2.3.5 Linear System Construction

Equations 2.3 and 2.4 can be expressed in matrix form as

$$
\left| \begin{array}{c} \mathbf{\Theta_a A} \\ \mathbf{\Theta_c C} \end{array} \right| \delta \mathbf{m} = \left| \begin{array}{c} \mathbf{\Theta}_a \left(\begin{array}{c} \delta \mathbf{t}_e \\ \delta \mathbf{t}_a \end{array} \right) \\ \mathbf{\Theta}_c \delta \mathbf{c} \end{array} \right| \tag{2.5}
$$

Recall that our model, $\mathbf{m}$ is parameterized as 5100 (60 x 85) discrete depth nodes on an x-y grid as is the correction vector, $\delta \mathbf{m}$. Submatrix $\mathbf{A}$ is an n x m matrix with n observations and m model parameters containing the travel-time derivatives defined in Equation 2.6. Construction of a row of $\mathbf{A}$ is as follows. For a given observation (reflection), the travel-time derivative with respect to reflector depth, $\frac{dt_r}{dm}$, is computed at the reflection point, $\mathbf{x}_r$ using

$$
\frac{dt_r}{dm}(\mathbf{x}_r, \phi) = u(\mathbf{x}_r)(cos(\phi_{inc}) + cos(\phi_{refl})) \tag{2.6}
$$

where u is the model slowness interpolated at $\mathbf{x}$ and ϕ_{inc} and ϕ_{refl} are the incident and reflected angles relative to vertical, respectively. Bilinear weighting is then applied to distribute $\frac{dt_r}{dm}$ to the four surrounding model nodes. Thus, each row of $\mathbf{A}$ contains 4 non-zero elements, corresponding to the 4 surrounding nodes.

Similarly, each row of matrix $\mathbf{C}$ contains 4 non-zero elements corresponding to the 4 nodes surrounding a particular *a priori* point constraint. For a given point constraint, bilinear weighting is again used to distribute that depth to surrounding nodes.

$\mathbf{\Theta}_a$ and $\mathbf{\Theta}_c$ are diagonal matricies containing equation weight values. Data equation weighting coefficients in $\mathbf{\Theta}_a$ are determined from pick uncertainty values, r. For earthquake data, r is defined as the sum of P and $P_{jdf}P$ uncertainties. For SHIPS data, r is assumed to be $0.1s$ for all $P_{jdf}P$ travel times. Weighting coefficients are then given by Kr^{-1} where K is a scaling value applied to maintain reasonable scaling of the linear system. The weighting coefficients in $\mathbf{\Theta}_c$ were determined through trial

and error such that the *a priori* constraints did not significantly increase data misfit. The right-side sub-vectors ($\delta \mathbf{t}_e$, $\delta \mathbf{t}_s$, $\delta \mathbf{c}$) are the travel-times residuals for earthquake and SHIPS data sets, and *a priori* constraint residuals defined in section 2.3.4, respectively.

2.3.6 Regularization

A smooth reflector model is determined by minimization of second-order spatial derivatives calculated by a finite-difference approximation to a 2-D Laplacian operator. To smooth the final model $\mathbf{m}_o + \delta \mathbf{m}$, a surface Laplacian is applied simultaneously to the current correction vector being solved for, and the model vector from the previous iteration, giving the equations

$$\nabla^2 \delta \mathbf{m} = -\kappa \nabla^2 \mathbf{m}^{i-1} \qquad (2.7)$$

where $\kappa \equiv$ feedback multiplier ($0 < \kappa < 1$) that allows adjustment to the smoothing of the model $\mathbf{m}$ and help maintain stability during inversion. A value of $\kappa = 0.5$ was used although experimentation showed no significant changes in the final model with other κ values. Implementation of a 2-D Laplacian functional $\mathbf{L}$ to a discritized function f=f(x,y) is given by

$$\mathbf{L}\left[f_{x,y}\right] = \frac{1}{\Delta l^2}\left[f_{x,y} - \frac{1}{4}\left(f_{x+1,y} + f_{x-1,y} + f_{x,y+1} + f_{x,y-1}\right)\right] \qquad (2.8)$$

if $\Delta x = \Delta y = \Delta l$

and equation 2.5 then becomes

$$\begin{vmatrix} \Theta_a \mathbf{A} \\ \Theta_c \mathbf{C} \\ \alpha \mathbf{L} \end{vmatrix} \delta \mathbf{m} = \begin{vmatrix} \Theta_a \begin{pmatrix} \delta \mathbf{t}_e \\ \delta \mathbf{t}_a \end{pmatrix} \\ \Theta_c \delta \mathbf{c} \\ -\alpha \kappa \mathbf{L}[\mathbf{m}^{i-1}] \end{vmatrix} \qquad (2.9)$$

where $\alpha \equiv$ smoothing weight.

2.3.7 Inversion

A least-squares solution to the linear system in Equation 2.9 for the correction vector $\delta\mathbf{m}$ is sought. The model size is 60 x 85 = 5100 nodes which is small enough to allow for direct solution methods without resorting to sparse matrix techniques. For this discussion, Equation 2.9 is collapsed to the standard form of a linear system

$$\mathbf{G}\delta\mathbf{m} = \mathbf{d} \qquad (2.10)$$

After each iteration, the reflector model is updated by adding the new correction vector

$$\mathbf{m}^i = \mathbf{m}^{i-1} + \delta\mathbf{m} \qquad (2.11)$$

and used to predict travel times for the next iteration. A least-squares solution requires the construction of the normal equations.

$$\mathbf{G}^T\mathbf{G}\delta\mathbf{m} = \mathbf{G}^T\mathbf{d} \qquad (2.12)$$

$\mathbf{G}^T\mathbf{G}$ is guaranteed to be positive definite which allows for a solution to be found using Cholesky decomposition and back-substitution (*Strang*, 1980). The data residual rms was computed at each iteration until its reduction from one iteration to the next becomes < 5% which typically required five or six iterations. Model results are presented in Chapter 3.

Chapter 3

SLAB GEOMETRY AND INTRASLAB SEISMICITY RELATIVE TO SLAB MOHO

Slab geometry results are presented in Section 3.1 and reveal a less broad arch than in previous models, with the shallowest dipping portion lying beneath the northern Olympic Peninsula. Trade-off between model regularization and data fit are shown in Section 3.2 where we justify of our choice of regularization. Similarities and key differences between our model and previous model results are discussed in Section 3.3. Finally, earthquake locations relative to the subducting Moho are presented in Section 3.4 and show distinct regions of upper mantle and oceanic crustal seismicity.

3.1 Slab geometry

Slab geometry is well constrained in the northern half of the model by active source data showing a northeast dipping slab averaging $\sim 19°$ beneath the Juan de Fuca Strait (Figure 3.1), consistent with the model produced by Preston et al. Inclusion of the earthquake reflections constrained the model farther south and refines arch geometry showing a "tighter" arch than observed in previous models, in the sense that the shallowest dipping ($\sim 10°$) portion lies beneath the upper Olympic Peninsula coincident with the Olympic Mountains (Figure 3.2). The southern flank dips southwest but less steep, averaging $\sim 15°$. Depth contours are provided in Table 3.1.
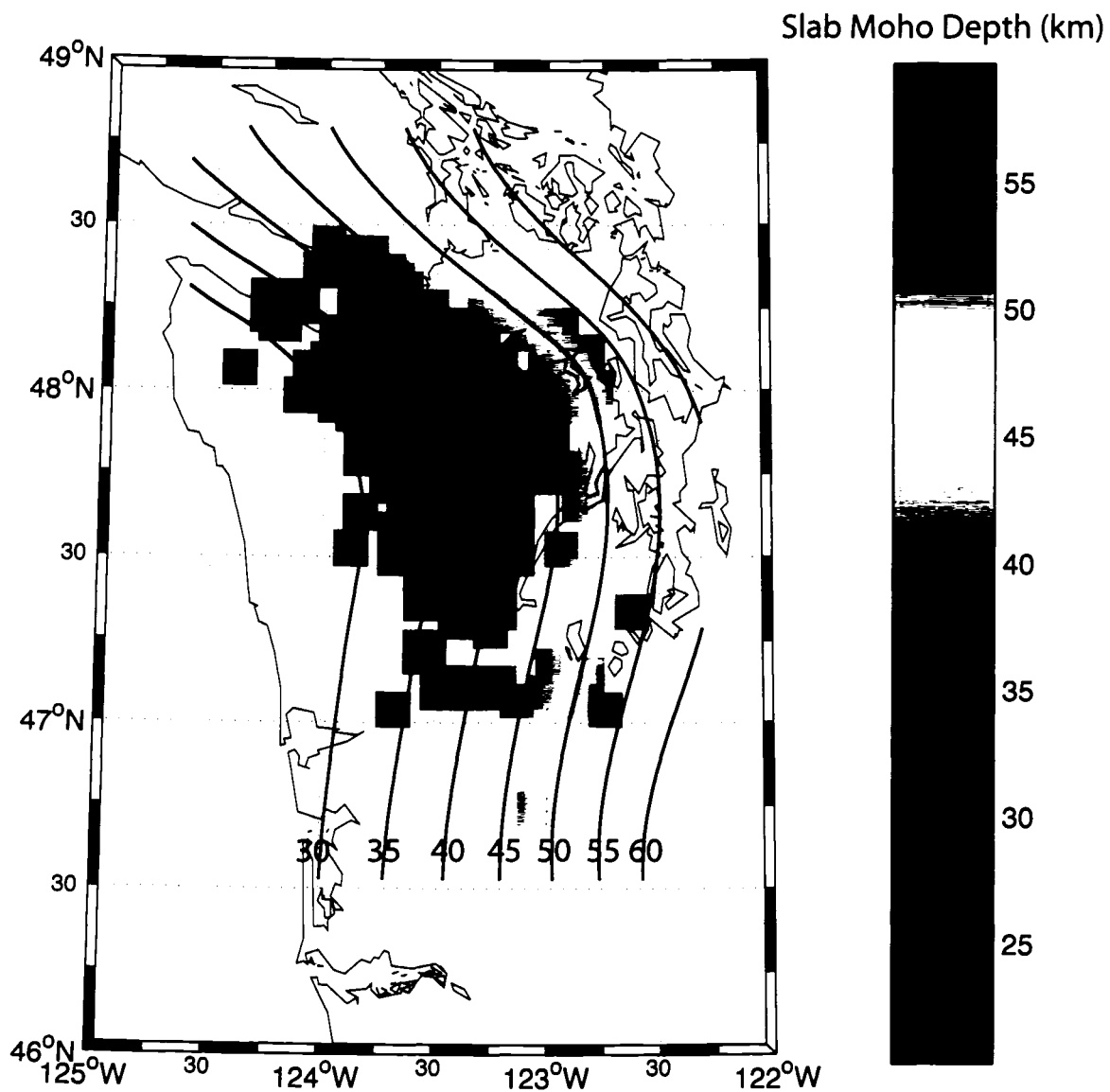
Figure 3.1: Favored slab moho model with depth contours shown and slab dips indicated. The arch structure is clearly seen and is asymmetric with a more steeply dipping northern flank. The top of the arch dips at about 10° in agreement with previous estimates.

Table 3.1: Depth contours of Juan de Fuca slab Moho (long/lat)

30 km		35 km		40 km		45 km		50 km		55 km		60 km	
-123.997	46.533	-123.719	46.535	-123.454	46.537	-124.424	48.796	-123.680	48.803	-124.034	48.800	-123.357	48.804
-123.990	46.641	-123.702	46.697	-123.438	46.699	-124.283	48.690	-123.583	48.695	-123.913	48.687	-123.318	48.751
-123.976	46.776	-123.679	46.832	-123.408	46.861	-124.150	48.610	-123.446	48.588	-123.771	48.586	-123.268	48.697
-123.960	46.892	-123.646	46.981	-123.367	47.023	-123.991	48.521	-123.300	48.496	-123.625	48.497	-123.220	48.653
-123.941	47.020	-123.615	47.130	-123.324	47.185	-123.827	48.434	-123.137	48.405	-123.462	48.409	-123.175	48.616
-123.925	47.128	-123.585	47.265	-123.272	47.347	-123.664	48.349	-122.975	48.319	-123.299	48.329	-123.101	48.562
-123.901	47.263	-123.535	47.400	-123.215	47.499	-123.501	48.271	-122.830	48.238	-123.137	48.247	-123.056	48.533
-123.878	47.371	-123.491	47.508	-123.175	47.659	-123.339	48.198	-122.693	48.139	-122.975	48.163	-122.975	48.481
-123.852	47.489	-123.451	47.643	-123.195	47.806	-123.177	48.105	-122.591	48.021	-122.849	48.076	-122.930	48.454
-123.837	47.614	-123.496	47.778	-123.297	47.940	-123.056	48.019	-122.526	47.886	-122.769	47.941	-122.854	48.410
-123.856	47.727	-123.577	47.861	-123.389	48.049	-122.976	47.874	-122.490	47.724	-122.732	47.779	-122.791	48.373
-123.902	47.830	-123.659	47.971	-123.540	48.134	-122.953	47.698	-122.496	47.535	-122.729	47.590	-122.732	48.338
-123.975	47.937	-123.746	48.074	-123.702	48.226	-122.972	47.509	-122.535	47.373	-122.759	47.428	-122.658	48.292
-124.058	48.017	-123.863	48.160	-123.865	48.307	-123.015	47.360	-122.584	47.239	-122.811	47.266	-122.612	48.261
-124.143	48.073	-124.026	48.227	-124.029	48.378	-123.066	47.212	-122.650	47.077	-122.859	47.131	-122.543	48.210
-124.266	48.140	-124.160	48.286	-124.192	48.455	-123.117	47.050	-122.703	46.942	-122.914	46.969	-122.491	48.167
-124.388	48.200	-124.311	48.349	-124.357	48.529	-123.161	46.888	-122.750	46.780	-122.956	46.807	-122.450	48.129
-124.511	48.245	-124.475	48.412	-124.522	48.606	-123.192	46.726	-122.769	46.591	-122.976	46.618	-122.400	48.075
-124.634	48.293	-124.619	48.470	-124.687	48.693	-123.204	46.537					-122.357	48.020
												-122.321	47.966
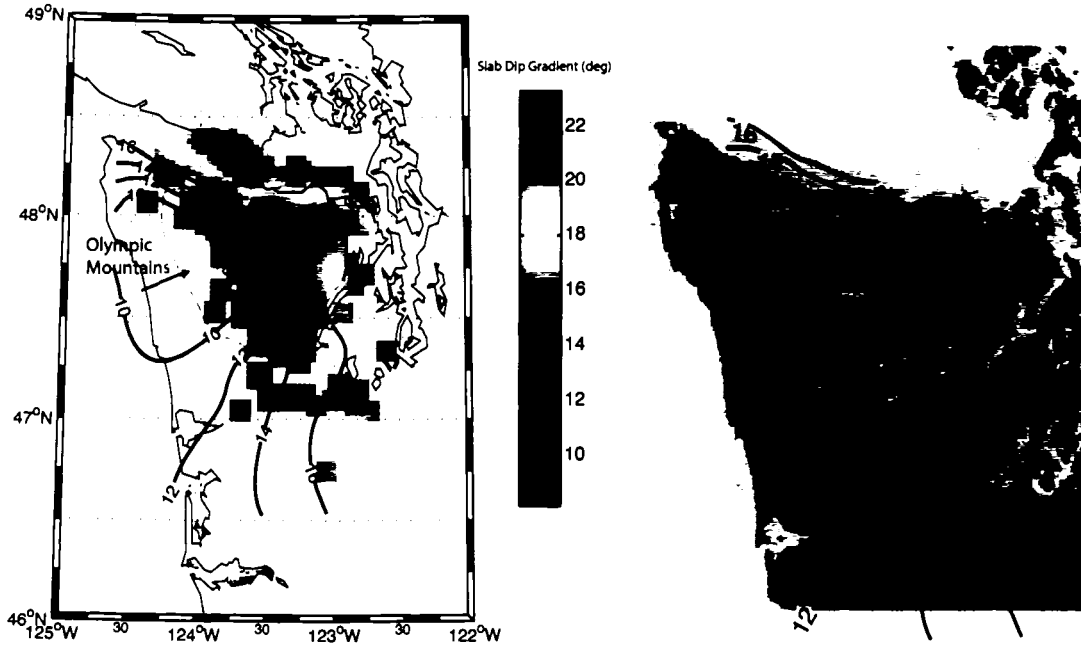
Figure 3.2: Slab dip contours show the shallowest dipping portion ($\sim 10°$) is localized beneath the northern Olympic Peninsula (left). This shallow dip is strikingly coincident with the Olympic Mountains (right)

3.2 Trade-Off Parameter

Our model is non-unique. Prior to regularization, the system of normal equations (Sections 2.3.5 - 2.3.7)

$$\mathbf{G}^T\mathbf{G}\delta m = \mathbf{G}^T\delta t \qquad (3.1)$$

is underdetermined with the number of model parameters outnumbering linearly independent equations as not all reflector nodes are sampled by reflection points. Noisy data produces an unrealistically complex reflector surface in the constrained regions and the null space of Equation 3.1 allows erratic behavior in the unconstrained portions. A smooth model was therefore assumed and imposed with a 2-D modified Laplacian (Section 2.3.6) to ensure stability during inversion and a more realistic result. A trade-off exists between the ability to fit the data and minimize model

"roughness", modulated by scaling the regularization equations with the trade-off parameter α (Equation 2.9).

In general, we seek a model that fits the data only to estimated uncertainties as model "improvements" made by fitting the data to precisions less than uncertainties are meaningless. A common measure of data misfit is chi-squared. Given N observations,

$$\chi^2 = \sum_{i=1}^{N} \frac{r_i{}^2}{e_i{}^2} \tag{3.2}$$

where r_i and e_i are the data residual $t_{obs} - t_{pred}$ and estimated uncertainty for observation i, respectively. If data errors are precisely known and are perfectly random having a gaussian distribution with zero mean, then ideally we should seek a trade-off parameter that produces a model such that distribution of data residuals is also random and that the standard deviations of uncertainties and residuals are equal $(\sigma_r = \sigma_e)$. The expected value of χ^2 is then $< \chi^2 > \approx N$. In practice, uncertainties are not typically known or estimated correctly, nor are they perfectly random. If uncertainties have been underestimated, as is likely for this experiment, then $\chi^2 > N$ for all models and we can only seek to minimize χ^2 by allowing model roughness to increase, but only to reasonable point. This balance is typically found by plotting χ^2/N against model roughness, defined in this case as the size of the model Laplacian, $\|Lm\|^2$, and looking for a "corner" in the curve. Figure 3.3 shows the results from a series of models produced with a range of α values labeled on the curve. A sharp corner exists near the $\alpha = 5$ and $\alpha = 10$ models. Models produced using $\alpha = 10$ maintained the same large scale features as $\alpha = 5$, but ray-tracing behaved better with the slightly smoother reflector. Therefore, $\alpha = 10$ was chosen as the preferred trade-off parameter.
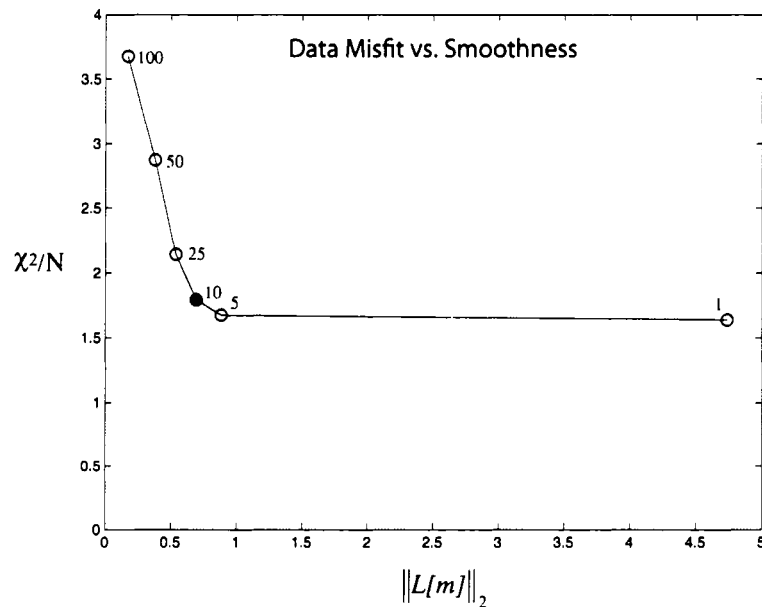
Figure 3.3: Data misfit plotted against model smoothness with trade-off parameters indicated. A sharp corner in the curve suggests a "best" model has a trade-off parameter between 5 and 10. The model produced using $\alpha = 10$ had better ray-tracing behavior while maintaining large-scale structure and was therefore chosen.

3.3 Model Comparisons

Previous slab geometry models and localized constraints were discussed in Section 1.2 and comparisons between our model and these studies are presented here. While some general features consistently emerge from the various studies, no two models agree everywhere so it is instructive to identify regions where our model agrees and departs from other models.

3.3.1 Preston, et al.

Comparison with the Preston model is arguably the most important as the SHIPS reflections used in Preston were incorporated into our model. A significant departure of the models in the region of data overlap would signify a possible problem with
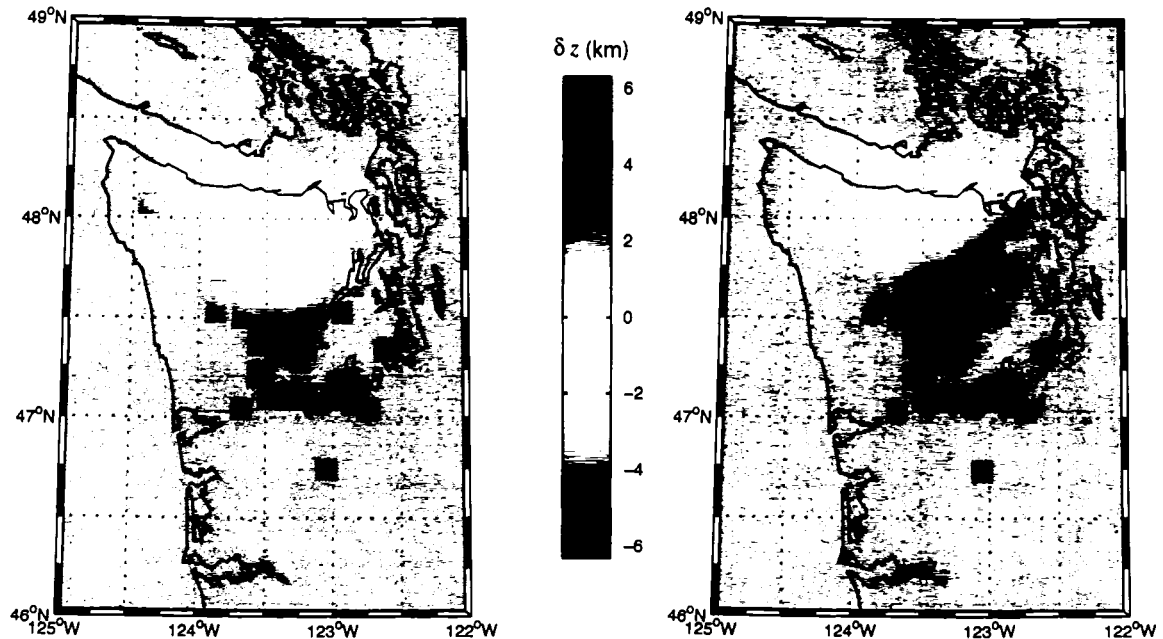
Figure 3.4: Difference between our model and the Preston et al. model. Blue and red shading indicates our model is deeper and more shallow, respectively. (Left) Our model minus the Preston model shows good agreement in the northern portion of the model with our model being deeper to the south. (Right) Our model using only earthquake data (no active source) minus Preston shows our model even deeper to the south with a slightly more shallow reflector at the northern edge.

methodology or with one data set or the other. Figure 3.4 shows the depth difference between the two models and generally shows our model to be deeper but not with a uniform bias. In the northern region where the data sets overlap, our model averages approximately 0.5 km deeper, while in the southern region our model averages nearly 4 km deeper with the most southern parts being over 8 km deeper. The deeper model to the south was expected from the data residuals presented in Section 2.2 but the 0.5 km difference to the north does not have an immediate explanation.

To test the methodologies, the SHIPS data only were inverted (Figure 3.5) which ideally should produce a model identical to the Preston model. The two models generally agree but the model we compute is still $\sim$ 0.3 km deeper on average with
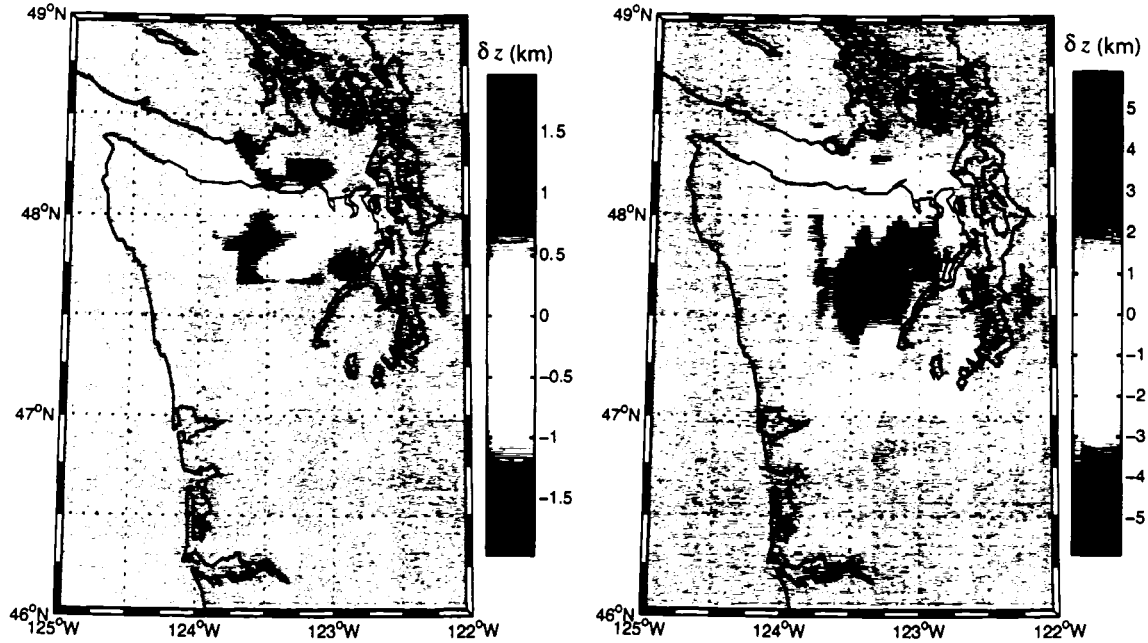
Figure 3.5: (Left) Our model using only active source data minus the Preston model. As expected, these two models show good agreement with most regions agreeing to with a few hundred meters (note the different scaling). Some local differences of up to 1-2 km are likely due to our more relaxed smoothing constraints. (Right) Our model minus the McCrory model shows our model approximately 2-4 km more shallow. This may be due to the influence upper mantle seismicity had on the McCrory model.

some parts being over 1.5 km different including a conspicuous area where our model is over 1 km shallower. The overall deepening of our model suggests a bias in the methods of computing reflected travel-times with the ray-tracing method we used predicting slightly shorter times for the same source-receiver pair than the finite-difference based method used by Preston. We estimate that a 0.3 km difference in reflector depth would result from a $\sim$ 0.1 s difference in reflected travel-time. This is less than estimated data uncertainties and so is not a serious concern, but does suggest a small systematic difference between the two travel-time calculators.

The region where our model pops-up was traced to a collection of reflections from shots in the Juan de Fuca Strait to stations near Hood Canal. It is not clear why

this feature does not appear in the Preston model, but it may be due to the more stringent smoothing constraints imposed by Preston.

Finally, we compared the model produced using only earthquake data to the Preston model (Figure 3.4). Again, we see good agreement on the northern coast of the Olympic Peninsula and a deeper reflector to the south. However, our model shallows to north which is likely either the result of differing regularizations or strategies used to constrain the model edges since earthquake reflections are sparse here. We conclude that the two models generally agree in the northern region of data overlap and that our model shows a more narrow arch, beginning its southeasterly dip further to the north than previously modeled.

3.3.2 McCrory, et al.

The model by McCrory et al. shows good agreement with our model geometry but is approximately 2 km deeper (Figure 3.5). They model the top of the plate rather than the slab moho so to compare the two models a 7 km thick oceanic crust was assumed. Many previous studies were compiled by *McCrory et al.* (2004) and assimilated to produce their model including some seismicity profiles in western Washington. This could produce the observed bias toward a deeper model if earthquakes occurring in the subducted mantle were used and assumed to be nearer to the top of the plate than they actually were.

3.3.3 Receiver Function Studies

Two receiver function studies in southwest Washington (Section 1.2) placed constraints on slab dip and direction near the southern end of our model region. *Owens et al.* (1988) estimated a $20° \pm 3°$ dip in the direction $110° \pm 20°$ near 46.8N, 123.4W. Similarly, *Lapp et al.* (1990) estimated a $16° \pm 5°$ dip in the direction $125° \pm 15°$ near 46.8N, 122.7W. Our dip of $\sim 16°$ in this part of the model agrees with Lapp et al., but
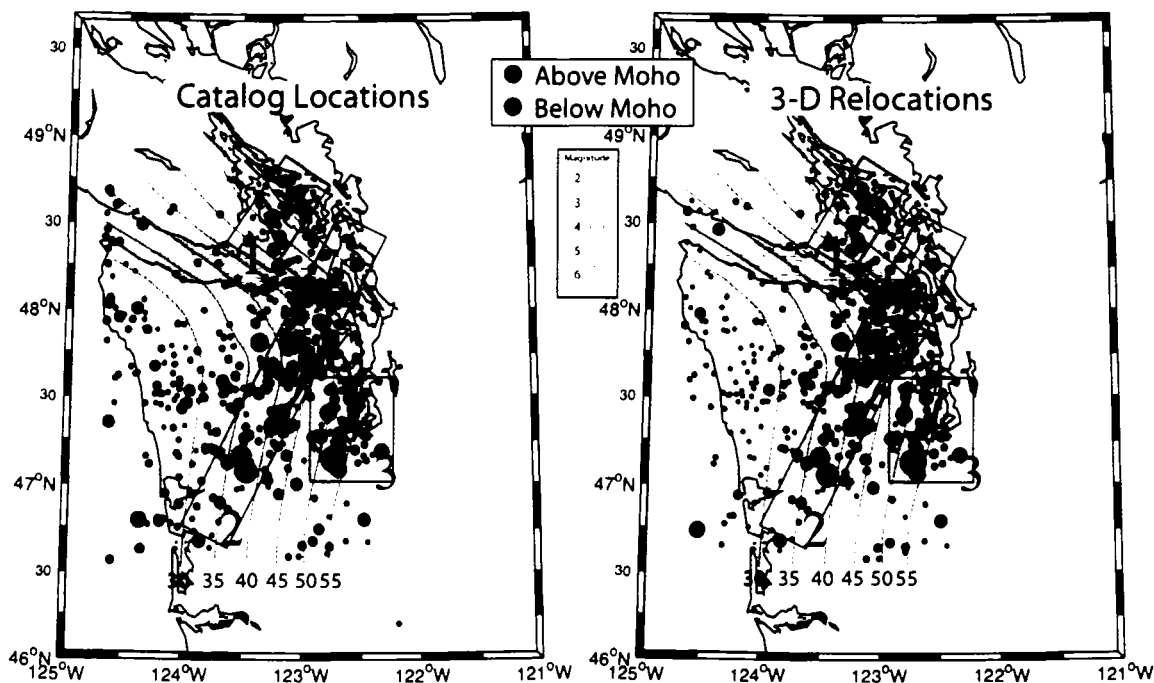
Figure 3.6: Cascadia intraslab earthquake locations from the PNSN catalog (top left) and relocated hypocenters using a 3-D velocity model (top right) color-coded by above (red) or below (blue) our Moho model. A NE trend of upper mantle events is evident in both sets (Region 2). Seismicity above the Moho is evident in Region 1 but is ambiguous in Region 3 as relocated events are systematically deeper and below the Moho.

is slightly less than the Owens and Crosson estimate. Our model also dips southeast but in the direction $100° \pm 5°$ which is more easterly than the other two studies.

3.4 Earthquakes Relative to Slab Moho

Fundamental to understanding the nature of Cascadia intraslab seismicity is the relative position of earthquakes to the slab as source processes differ for earthquakes occurring in the oceanic crust and upper mantle (Section 1.4). We sorted all intraslab seismicity by their relative position to our Moho model (above or below) (Figure 3.6). We used both catalog locations and earthquakes relocated using our 3-D velocity
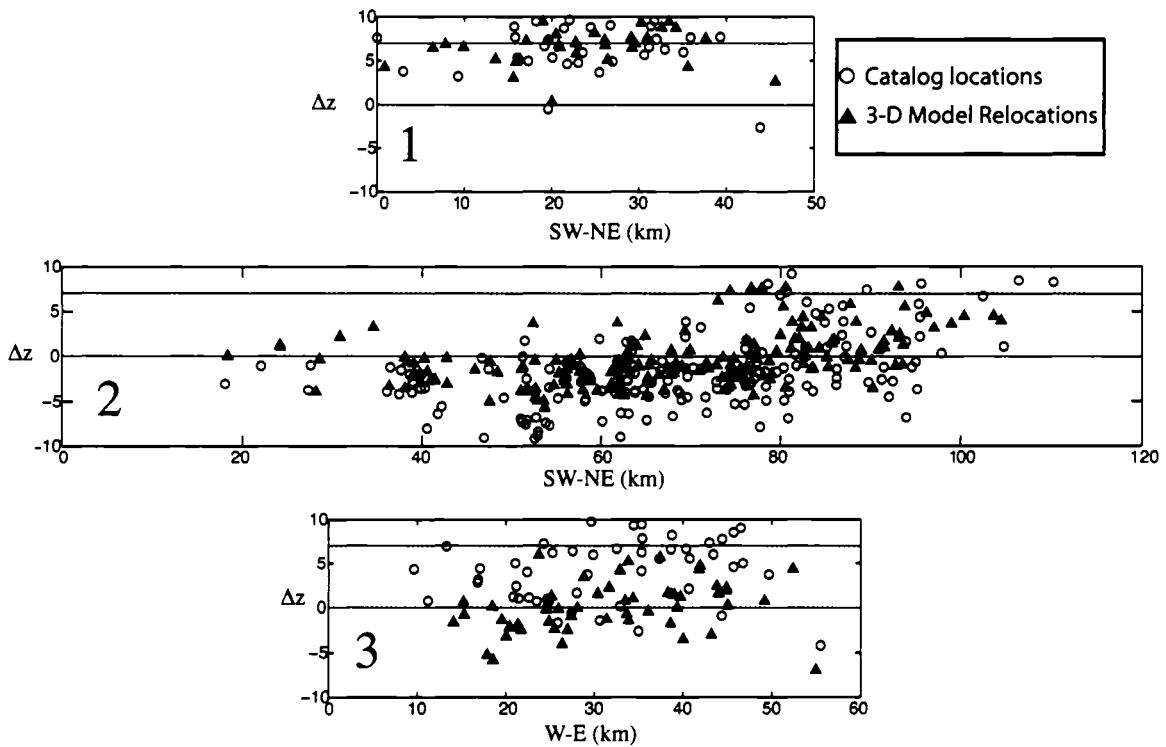
Figure 3.7: Earthquake depths relative to our Moho model (lower blue line) from the three regions in Figure 3.6. Upper blue line represents approximate top of plate assuming 7 km thick oceanic crust. Open circles and filled triangles represent catalog and relocated hypocenters, respectively. Note the systematically deeper relocated events in Region 3.

model[1]. While there are differences between the two location sets, we may conclude two points: 1) Earthquakes are occurring in the oceanic crust and in the upper mantle and 2) the distribution of each type is not random. Upper mantle seismicity is concentrated along a northeast linear trend across the Olympic Peninsula, oblique to the arch contours (region 2 in Figure 3.6) and most of the remaining seismicity occurs in two regions on the flanks of the arch between 45 and 60 km depth (regions 2 and 3). Catalog locations suggest the latter seismicity is occurring in the oceanic crust

---

[1]Only earthquakes within our model region were catagorized as either above or below the moho and the following discussion refers only to this subset. However, seismicity is sparse beyond our model boundaries and so would not change our conclusions.

but relocated events in the southern group locate in the upper mantle. Figure 3.7 shows the relative vertical position of earthrquakes to the Moho for both location sets (catalog and relocated). Earthquake locations in Region 1 display no obvious systematic difference between sets with most earthquakes occurring between 5 and 10 km above our Moho. Assuming these are intraslab earthquakes and assuming a 7 km oceanic crust, our model is either too deep here or the earthquakes are systematically locating too shallow. Seismicity in the southwest and central portions of Region 2 is primarily in the upper mantle with relocated earthquakes tending to collapse toward the Moho. In the northeast portion of Region 2, beneath the northeast tip of the Olympic Peninsula and northern Puget sound, seismicity occurs in the oceanic crust beginning near 45 km depth (Figure 3.8) and magnitudes are generally lower than the Region 2 upper mantle events (Figure 3.9). Region 3 shows the largest systematic difference between catalog locations and relocated hypocenters with the relocated events being $\sim$ 5 km deeper. This places many of these events in the upper mantle, including the M6.8 Nisqually event and its largest aftershock. Because we have very low reflector model resolution here and the 3-D model used to locate events has poor resolution in this region, we are unable to conclude unambigously where earthquakes in this very important seismic region are occurring relative to the plate. In Chapter 5 we do, however, present evidence that seismicity in the two "flank" regions (1 and 3) are similar.
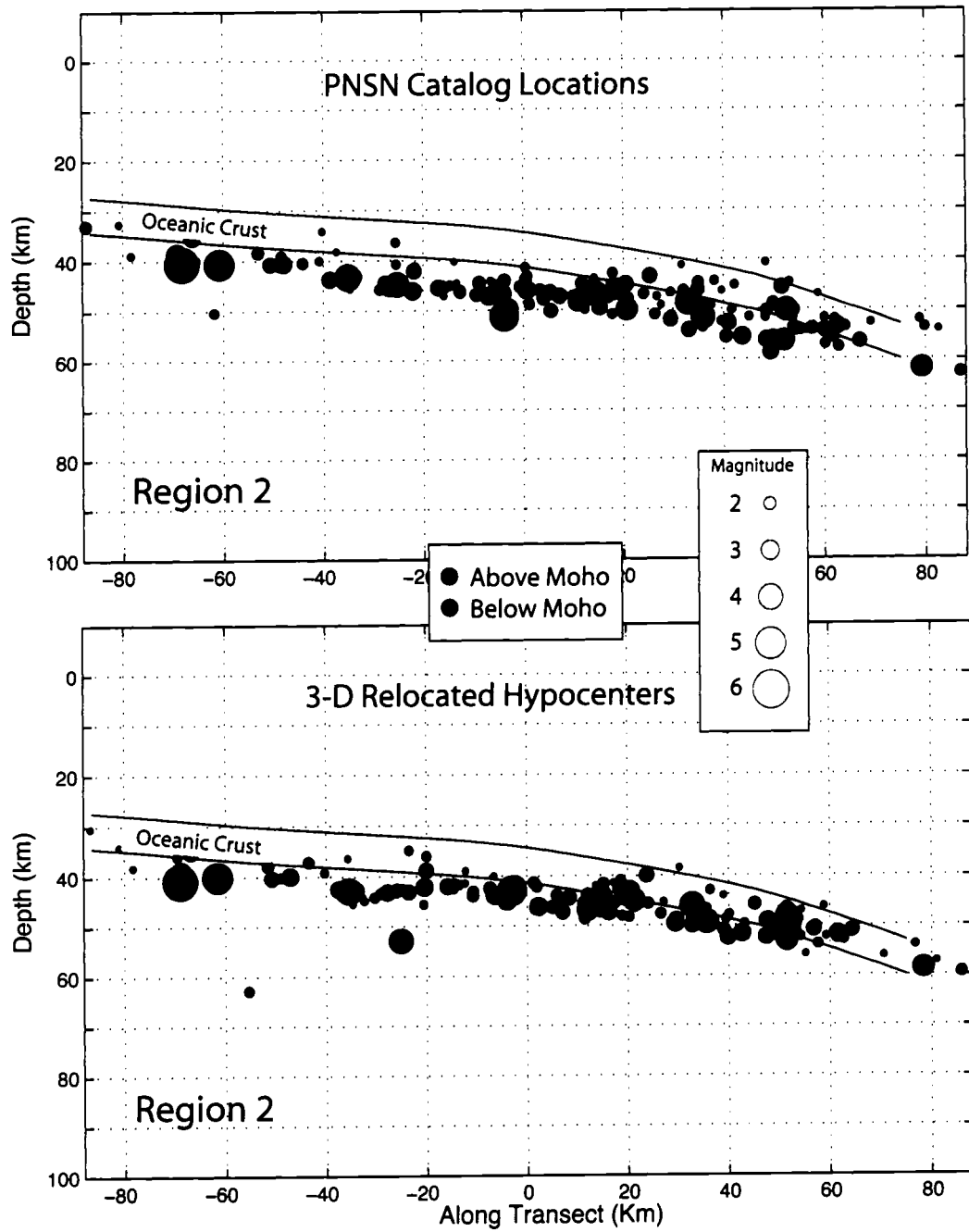
Figure 3.8: Cross-section of Region 2 from Figure 3.6 shows little difference between catalog and relocated events. Earthquakes begin occurring above the Moho in the oceanic crust near 45 km depth.
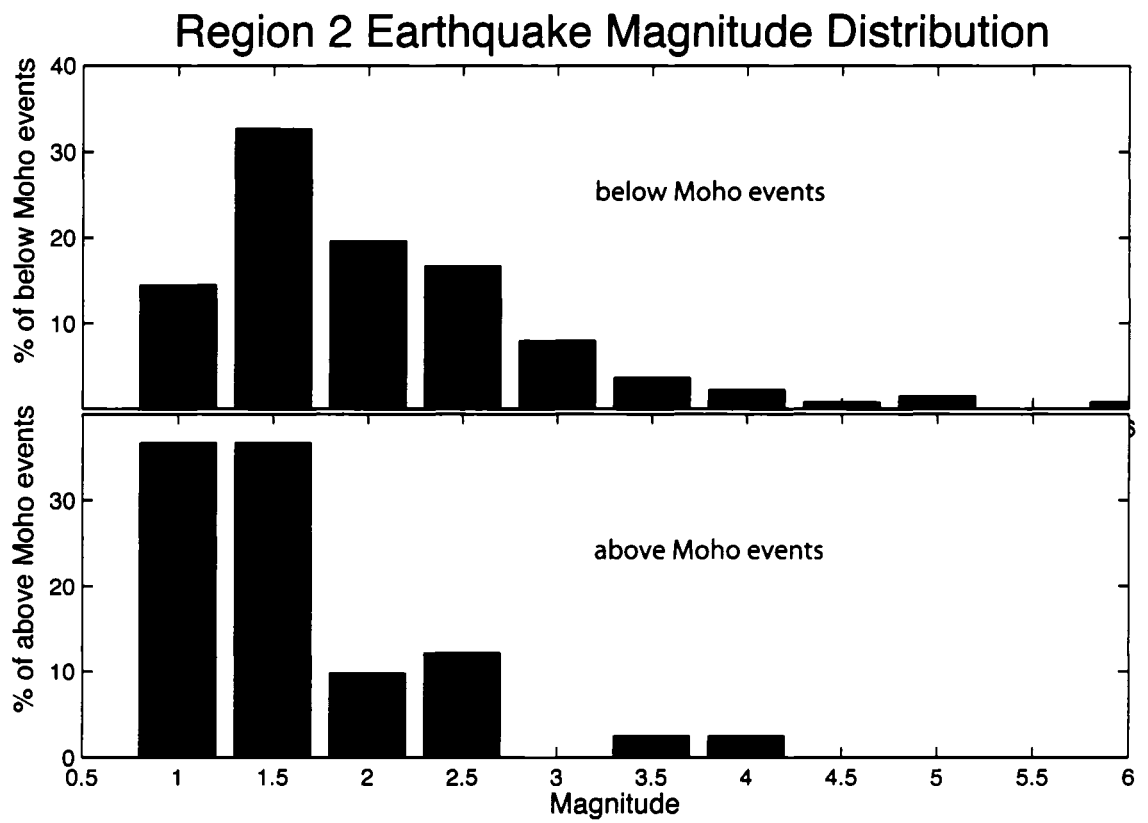
Figure 3.9: Magnitude histograms for events in Region 2. Earthquakes occurring in the crust tend to cluster at lower magnitudes ($M < 2$) than those in the upper mantle.

Chapter 4

ANOMALOUS SECONDARY P FROM INTRASLAB EARTHQUAKES

An anomalous but prominent secondary P phase is observed from a small number of Cascadia intraslab earthquakes. Earthquakes producing this anomalous phase are located in the two "flank" regions discussed in Section 3.4 (Figure 3.6) and is only observed on Olympic Peninsula stations. Figure 4.1 shows the locations of these events and sample record sections from an event showing the phase and from one without the phase. These anomalous phases were first observed by *Mundal et al.* (1990) during an investigation of Cascadia intraslab first-arrival apparent velocities. At the time of the Mundal study, approximately 350 Cascadia intraslab earthquakes had been located by the Pacific Northwest Seismograph Network (PNSN), but only 7 earthquakes were identified as having the phase, two of which have been rejected for this study.[1] Approximately 800 intraslab earthquakes were located by the PNSN between 1980 and 2004 and examined for this study, producing a total of 13 events that have been identified as having the secondary phase including 5 from the Mundal study (Table 4.1). Record sections for all 13 events are shown in Appendix A.

---

[1] Two events near the Washington-Oregon border show evidence of a secondary arrival on Olympic Peninsula stations, but are $\sim$ 100 km more distant. The secondary phase apparent velocity for one event is consistent with the apparent velocity reported here while the other was indeterminate. While the observations could be related to the phase in question, the larger offset distances and lack of other events in the area for which apparent velocities could be measured created a lack of confidence that this is the same phenomenon.
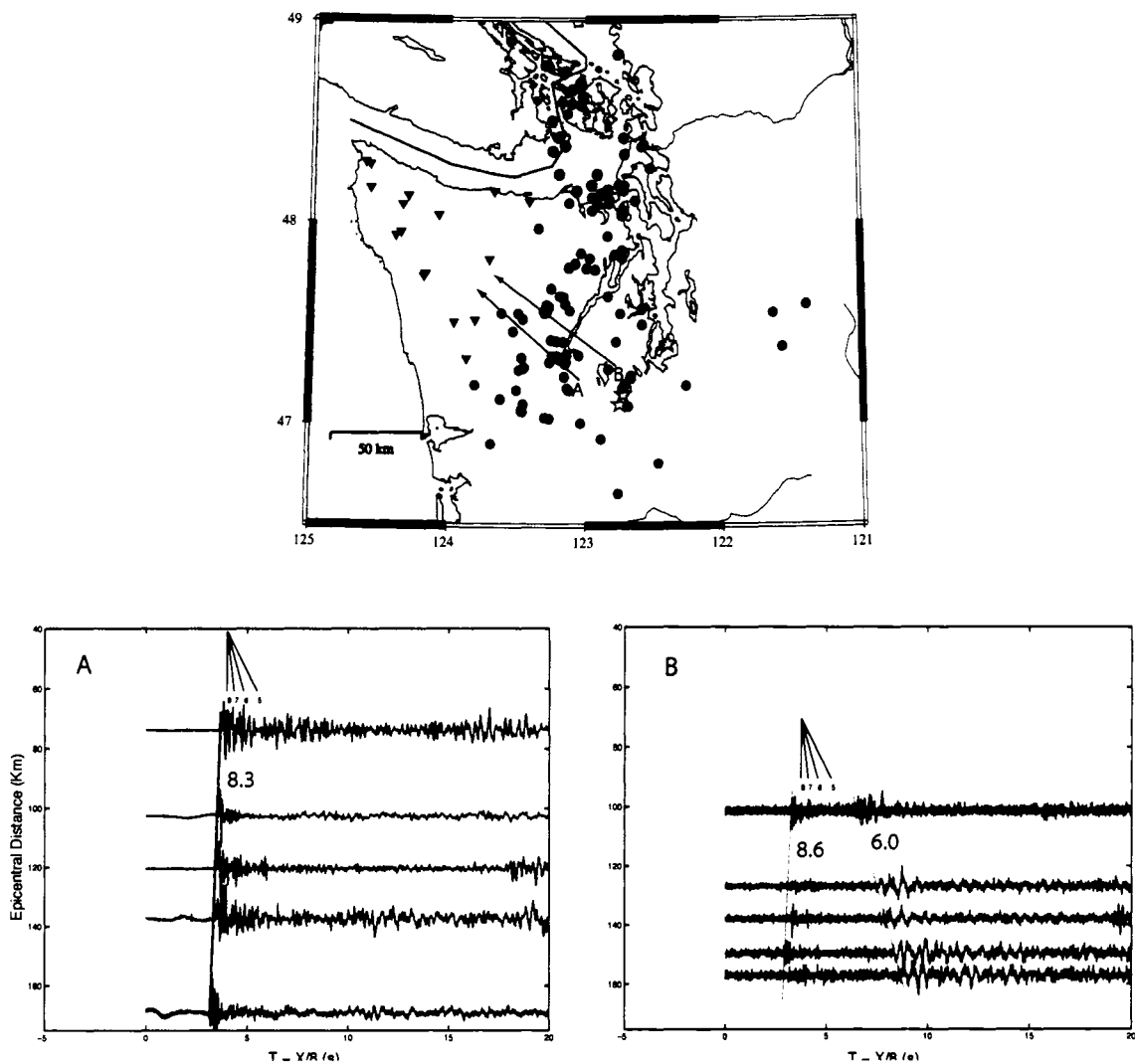
Figure 4.1: Example record sections of an intraslab earthquake without X (A) and one with X (B). The largest population of type I events (those with X) is in the southern Puget Sound (red circles). Three type I events are also off the SE tip of Vancouver Island. Type II events are shown as blue circles. X often has a large amplitude relative to the first arrival with an apparent velocity near 6 km s^{-1}. In both cases, the first arrivals have an apparent velocity consistent with P waves traveling updip in the upper mantle.

Table 4.1: Type I events separated into the northern and southern groups.

Type I Events								
		Event	Lon	Lat	Depth (km)	M	Obs	Vp(app) km/s	Vx(app) km/s
south group	1	84121708300	-122.8315	47.2737	46.3	3.2	4	-	-
	2	85022817015	-122.5848	47.5013	52.6	3.7	5	8.55 ± 0.20	5.72 ± 0.17
	3	88031110011	-122.3222	47.1907	64.7	3.9	2	-	-
	4	89061820382	-122.7758	47.4097	44.8	4.4	4	-	-
	5	91031620165	-122.6688	47.2422	49.5	2.6	7	8.39 ± 0.25	6.01 ± 0.25
	6	01030109102	-122.7133	47.1970	54.3	3.4	6	8.43 ± 0.12	6.06 ± 0.50
	7	01030114233	-122.7293	47.1802	51.4	2.7	6	8.64 ± 0.12	6.24 ± 0.15
	8	01072215135	-122.6855	47.0880	52.4	4.3	5	8.22 ± 0.07	6.04 ± 0.30
	9	04011608181	-122.5862	47.5763	60.4	3.6	7	8.95 ± 0.21	5.69 ± 0.50
							Avg*	8.30 ± 0.50	5.92 ± 0.40
north group	10	99040317292	-123.2437	48.3503	46.3	3.1	4	-	-
	11	00091014533	-123.1903	48.4240	49.3	3.2	7	8.67 ± 0.08	5.67 ± 0.32
	12	01101504570	-123.0630	48.1523	44.4	2.9	3	-	-
	13	03101203423	-123.2230	48.4402	46.6	2.6	3	-	-
* Averages include picks from all events							Avg*	8.33 ± 0.30	5.76 ± 0.30

4.1 Secondary Phase

In this section, observations about this phase are cataloged and discussed. The limited source-receiver geometries from which the phase is observed, apparent velocities, polarization and spectral content are key observations necessary to make a correct interpretation.

4.1.1 Nomenclature

The nomenclature of *Fukao et al.* (1983) for secondary phases observed in southwest Japan is borrowed, referring to the secondary phase as 'X'. Events with a clearly observed X phase are labeled type I and those without X as type II. It is important to note that type II events are not simply the converse of type I, i.e. an event without an observed X was not automatically classified as type II. A majority of the events examined had magnitudes too low to make any judgment about the existence of X. In other cases, earthquakes were too large, producing clipped seismograms that could

not be confidently classified. For still others, there was the suggestion of secondary energy, but it either had a low signal-to-noise ratio or was emergent making a clear classification difficult. For this study, a type II classification means that a coherent X phase is clearly absent.

4.1.2 Earthquake and Station Distribution

The spatial distribution of the 13 type I events is localized in the two flank regions of the arch. Nine of the events occurred beneath southern Puget Sound and 4 off the southeast tip of Vancouver Island (Figure 4.1). The southern region is especially interesting because it contains the largest recorded Cascadia intraslab earthquakes. Indeed, two type I events are the largest aftershocks of the 2001 M6.8 Nisqually earthquake. The Nisqually main shock was too large to classify.

X is only observed at stations on the Olympic Peninsula, ranging in epicentral distance from 80 to 190 km (Figure 4.2). This is demonstrated in Figure 4.3 with seismograms from Event 1 arranged by station azimuth. This region is characterized by the geologically distinct Olympic Core Complex, comprised of relatively low-velocity sedimentary and metasedimentary units accreted and uplifted as a result of Juan de Fuca subduction. X is not consistently observed on other Olympic Peninsula stations positioned over the higher velocity Eocene basalts, locally the Cresent Formation, or other recent volcanics.

4.1.3 Apparent Velocities

The apparent velocity of first-arrival P-waves are consistent with updip traveling upper mantle refracted waves or head waves, averaging ~ 8.3 km/s for both the southern and northern groups. X arrives between ~ 1.5 and 7 seconds after the first arrivals with apparent velocities ranging from 5.7 to 6.2 km/s (Table 4.1 and Figure 4.4). These velocities are comparable to Olympic Core rock intrinsic compressional wave
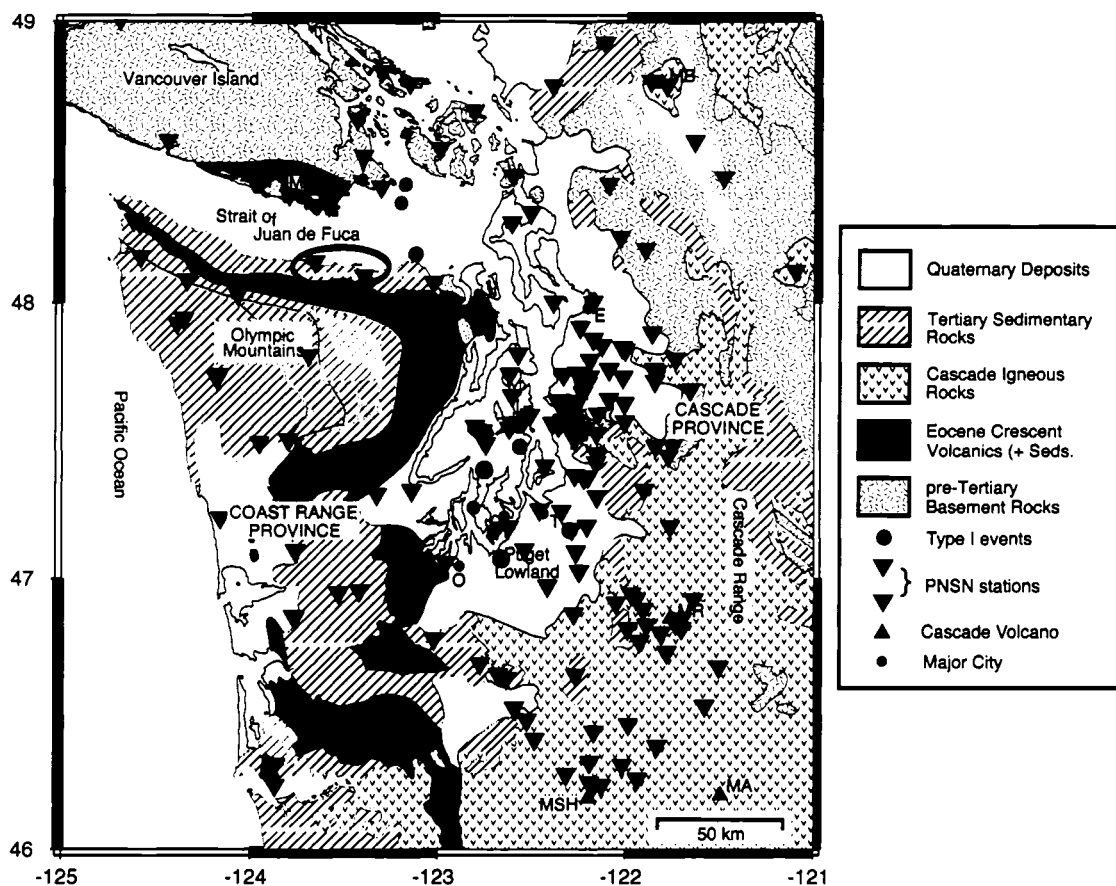
Figure 4.2: X is only observed on stations of the Olympic Peninsula positioned over the Olympic Core (magenta triangles). Other PNSN stations not showing X are also shown (green triangles). The 13 type I events are shown as red circles. The two circled stations at the top of the Olympic Peninsula often display what appears to be X arriving earlier than on the other stations. This is likely due to X partially traveling through the high-velocity Cresent Basalts (dark shaded).

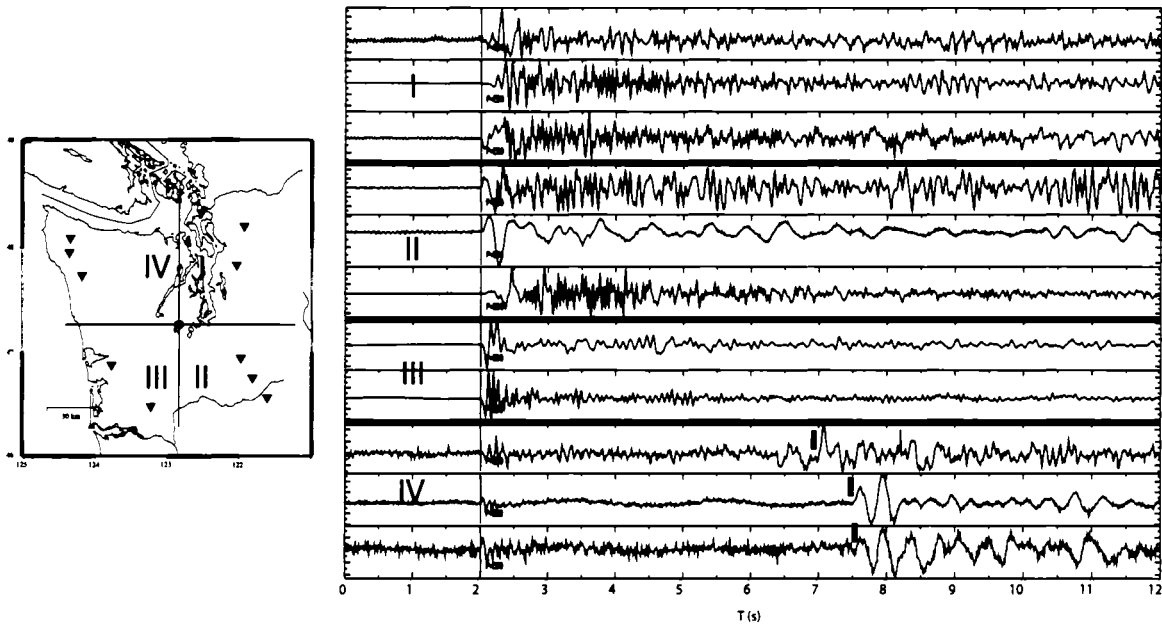Figure 4.3: Seismograms from Event 1 at stations in different azimuthal directions. Traces are aligned on first arrivals. X is only observed at stations in quadrant IV (solid bars).

speeds and are somewhat less than estimates of untransformed oceanic crust (6.5 - 6.9 km/s) beneath western Washington (*Taber and Lewis*, 1986).

4.1.4 Polarization

Large vertical to horizontal amplitude ratios indicate X is a P-wave. Rotated seismograms from two type I events are shown in figure 4.5 . Unfortunately, no 3-component instruments were installed on the Olympic Peninsula prior to 1994 so polarization analysis of the the 5 type I events occurring between 1984 and 1991 was not possible. First motion phase polarities of X arrivals relative to first arrivals could not be determined due to interference from first arrival coda.
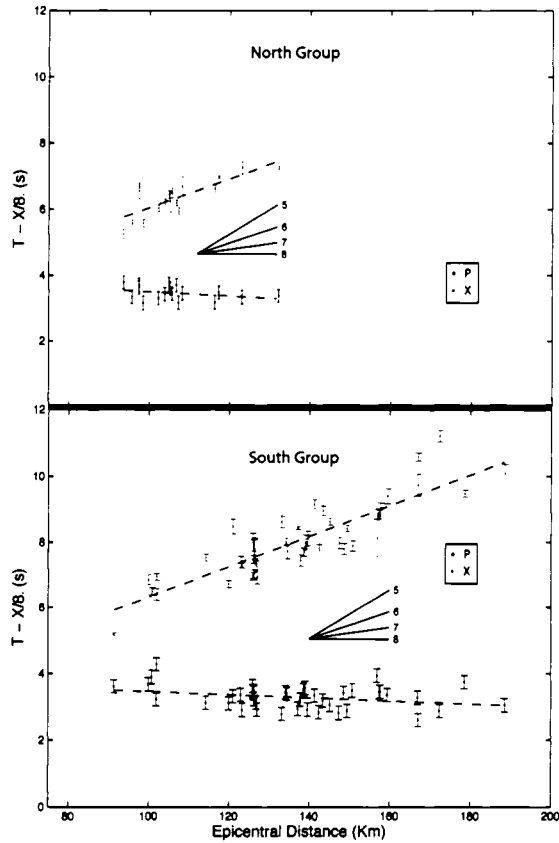
Figure 4.4: Reduced travel-time plots for the northern (upper) and southern (lower) groups of type I events with error bars representing uncertainty in the phase pick. The two regions display approximately the same average apparent velocities for first arrivals and X (Table 4.1).

4.1.5   No Secondary S

S arrivals with apparent velocities consistent with upper mantle paths (> 4.5 km/s) are clearly visible, but no secondary S is observed (Figure 4.6) . Since P and S typically follow very nearly the same path, this suggests that X is either an SP converted phase, or takes a path through material with low enough Q values (high attenuation) to dampen the secondary S to levels below the noise. Given that there is some variability in focal mechanisms for type I events, it seems unlikely that the
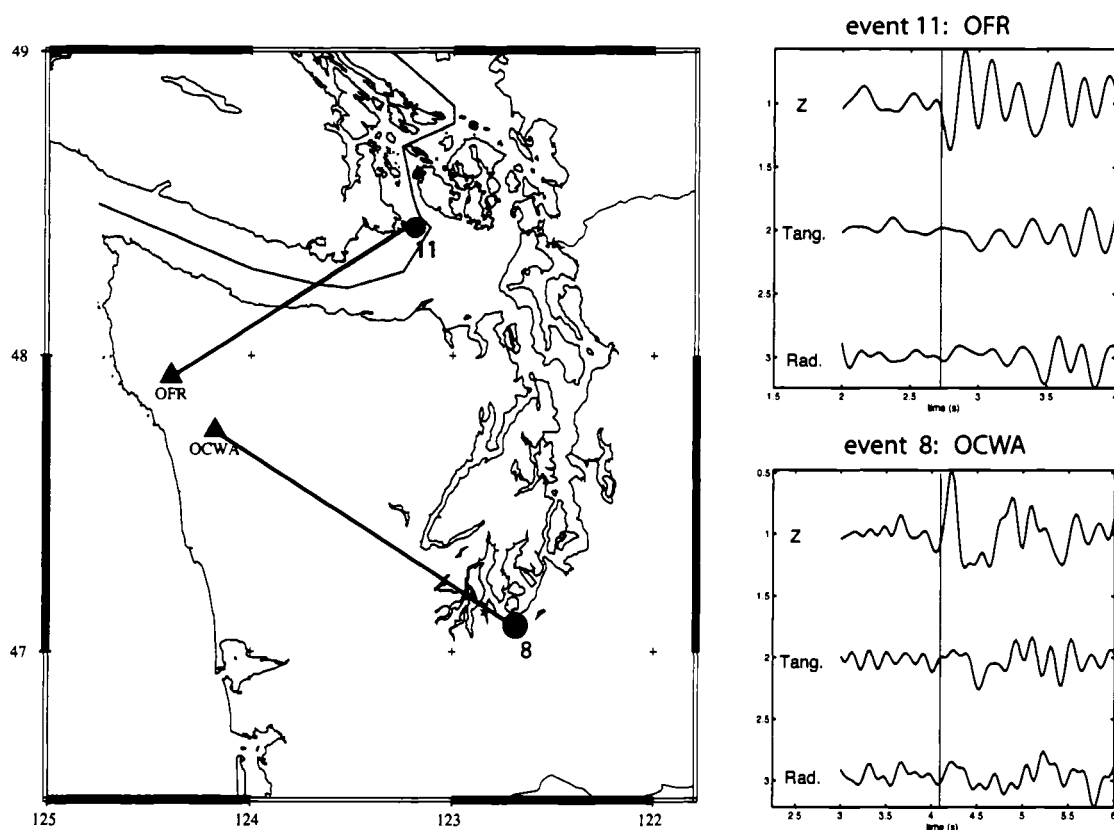
Figure 4.5: Seismograms from event 11 to station OFR and event 8 to station OCWA, rotated into their source-receiver coordinate systems. Blue lines indicates onset of X in each case. The large vertical-to-horizontal amplitude ratio is indicative of X arriving as a P-wave.

lack of secondary S could be explained by source radiation effects.

4.1.6   Low Dominant Frequency

A prominent characteristic of X is a low dominant frequency near 1.5 Hz (Figures 4.7 and 4.8) compared with a 5-7 Hz dominant P-wave frequency.
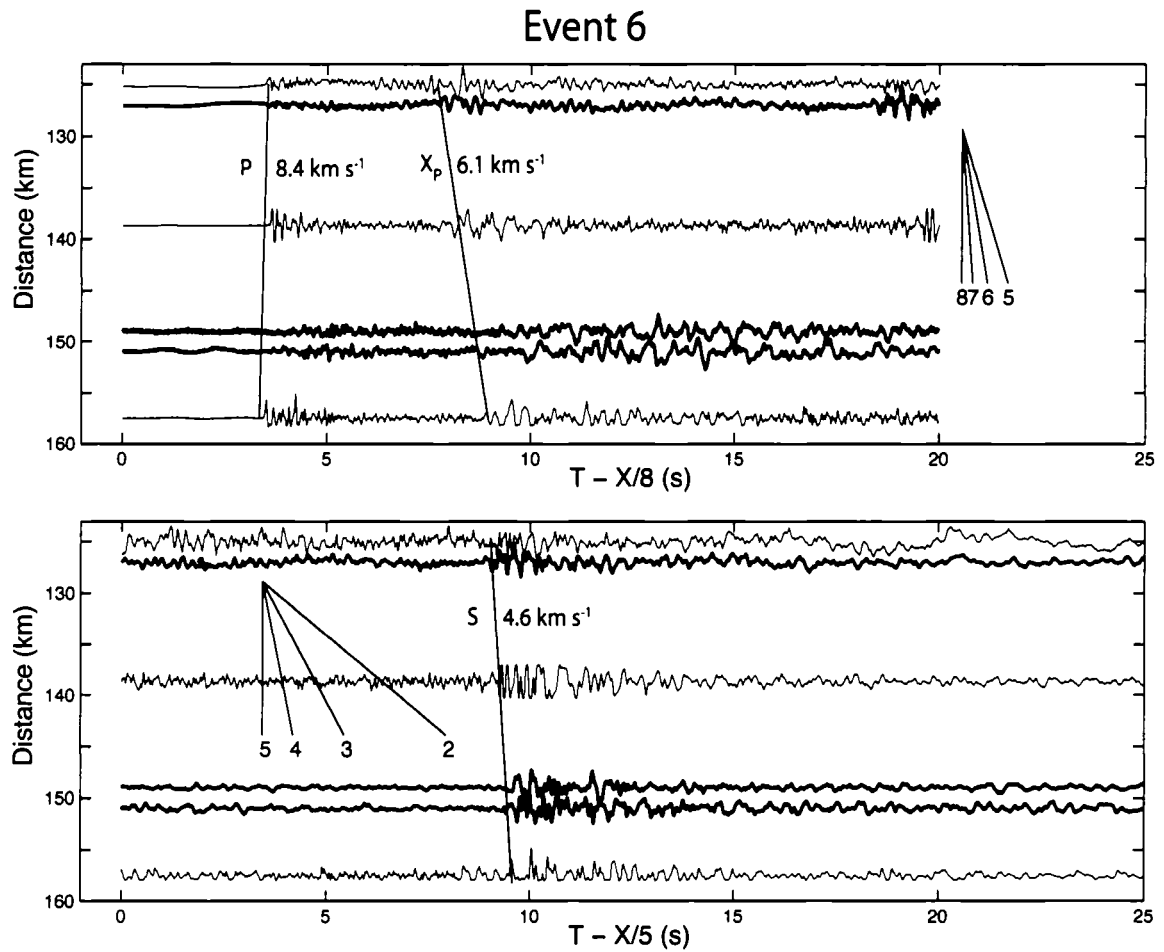
Event 6

Figure 4.6: Reduced velocity seismograms around the P-wave (top) and S-wave (bottom) for event 6. While a clear secondary P is observed, no corresponding secondary S is observable, contrary to the X phase observed in southwest Japan (Figure 4.11). Trace data from horizontally oriented seismometers are bold.
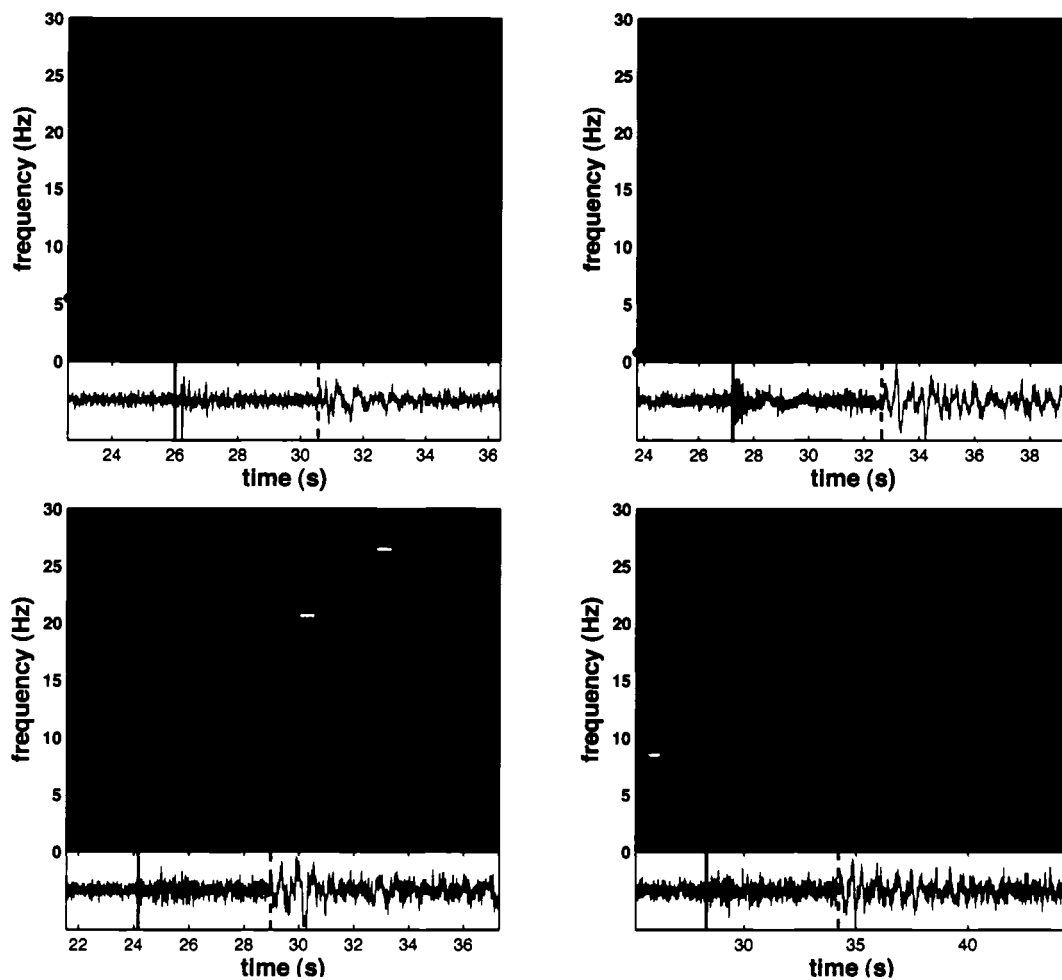
Figure 4.7: Spectrograms from Event 5 on four Olympic Peninsula stations. The low frequency content of X (vertical dashed line) compared to P (vertical solid line) is evident in the seismograms. P typically has a dominant frequency between 5 and 8 Hz while X has dominant frequency of about 1.5 Hz.

Figure 4.8: Spectrograms from Event 11 on four Olympic Peninsula stations. The low frequency content of X (vertical dashed line) compared to P (vertical solid line) is evident in the seismograms. P typically has a dominant frequency between 5 and 8 Hz while X has dominant frequency of about 1.5 Hz.
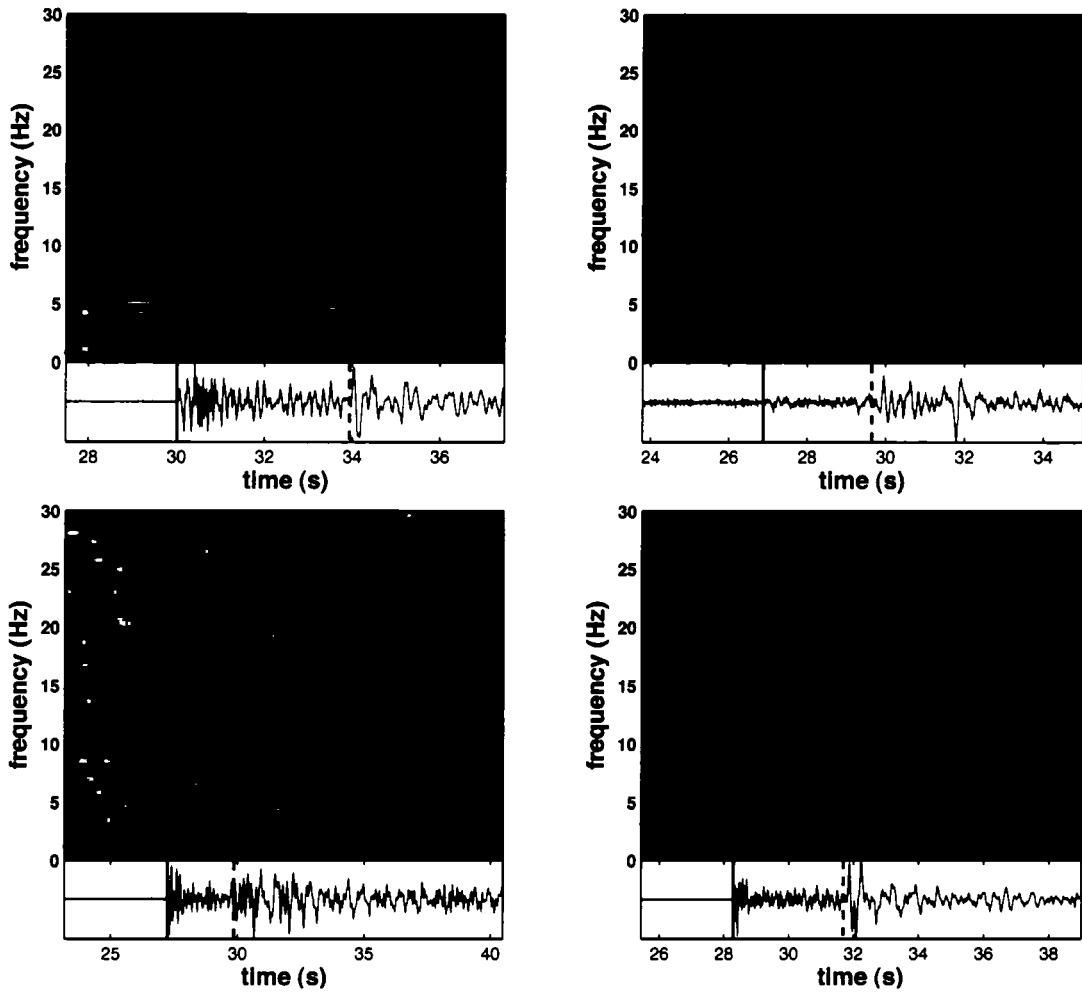
4.2 Travel-Time Modeling

2-D ray-tracing was the primary method used to interpret X as this allowed for efficient testing of many possible phase interpretations and velocity models. We forward modeled our velocity model to maximize agreement with observed travel-time data for a given phase. While the velocity models are not unique, the general behavior of different phases could be examined and approximate bounds on velocity values and gradients estimated.

4.2.1 Rayinvr

Rayinvr, a 2-D ray-tracing and inversion code by Colin Zelt (methodology described in (*Zelt and Smith*, 1992)) was chosen to compute rays and travel-times for its flexibility in model design and ability to compute refracted, reflected and head waves. Layer boundaries within the velocity model are parameterized as connected segments, each having arbitrary dip, along which velocity nodes may be assigned. Each layer is divided by vertical segments at the velocity node positions forming trapezoidal blocks. Horizontal and vertical linear gradients are assumed within each block to interpolate a velocity field and user determined Poisson ratios for each block are allowed. Rays are traced at regularly spaced take-off angles or a 2-pt option may be employed.

4.2.2 Model Construction

For interpretation purposes, we modeled travel-times from five type I events (1,5,6,7,8) that are in the southern group and lie approximately along the same line toward the Olympic Peninsula. A 2-D profile taken from a 3-D tomographic model (Crosson, pers. comm.) was used to construct a simplified 2-D model (Figure 4.9). The key features of the model are the low-velocity accretionary complex to the west, buttressed against the relatively high-velocity Cresent formation basalts. Tomography also suggests accretionary material being thrust under the Cresent basalts during
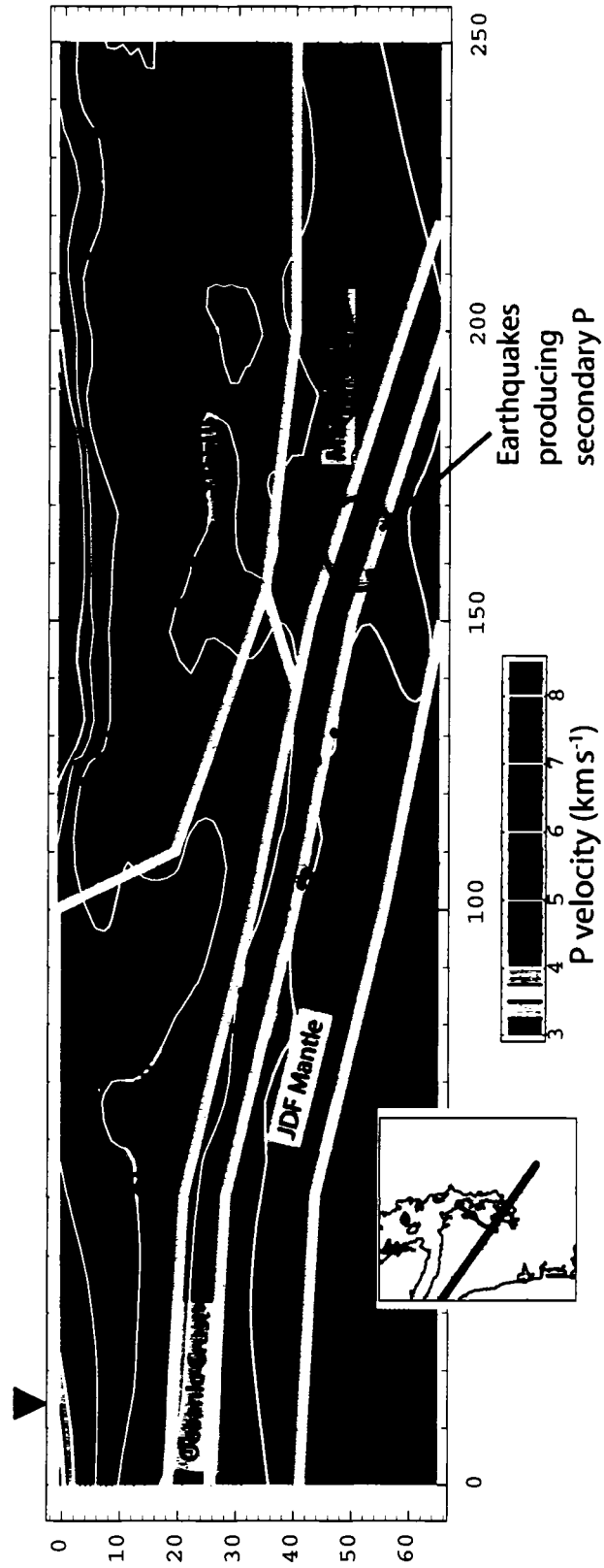
Figure 4.9: The cross-section shown was used as the basis for our 2-D model through which we ray-traced to compute travel-times and ray paths.
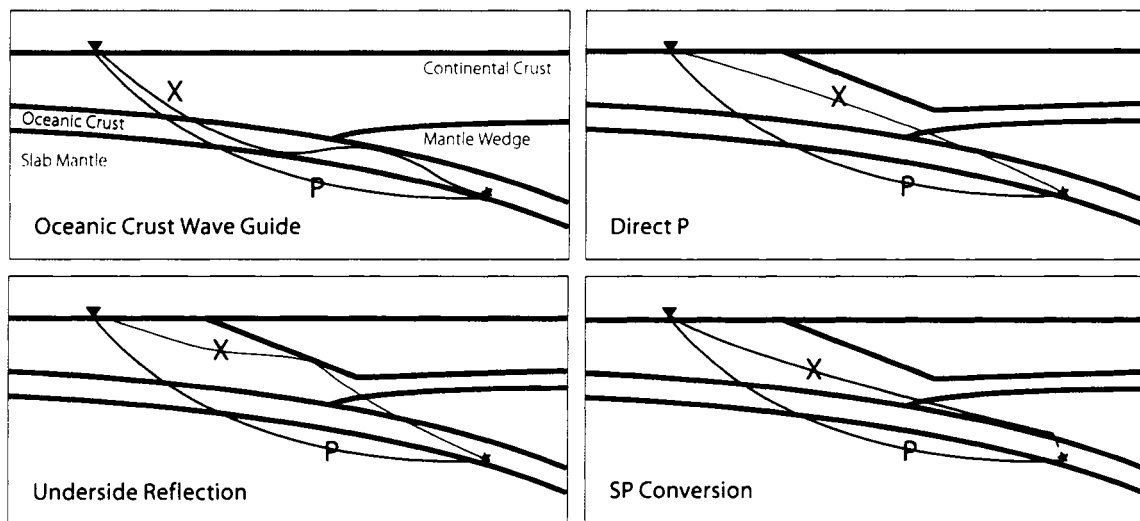
Figure 4.10: Each of the four X interpretations shown were considered. Ultimately, the SP conversion in case 4 fit all our observations the best and is our interpretation.

subduction, forming a negative velocity gradient in the lower continental crust. This negative gradient proved to be an important element for delivering energy to the observed station distances which is discussed further in Section 4.2.3. The location of the subducting Juan de Fuca plate interface is not well constrained from tomography, so the slab model from this study was used to define a slab Moho. A constant 7 km thick oceanic crust was assumed.

4.2.3 Possible Interpretations

Four possible interpretations of X were considered. 1) P-waves trapped in the oceanic crust acting as a low-velocity wave-guide 2) P-waves taking a direct path through the mantle wedge and continental crust 3) underside reflections off the Olympic Core-Cresent Basalt interface and 4) an SP conversion at the top of the JDF plate. Cartoons of each model are shown in Figure 4.10. For each case, rays are traced from each of the 5 event locations listed in the previous section and adjustments made to the velocity model to achieve good data fit in a qualitative sense.

Case 1: Oceanic Crustal Wave-Guide

Secondary P arrivals from intraslab earthquakes in southwest Japan and Alaska have been interpreted as energy trapped in untransformed oceanic crust, acting as a low-velocity wave-guide as the slab descends into the mantle (*Fukao et al.*, 1983; *Hori et al.*, 1985; *Abers and Sarker*, 1996) (Figure 4.11). In this model, trapped energy travels updip in the relatively low-velocity basalt and gabbro of the crust, bounded by the higher velocity slab mantle below, and the aesthenospheric wedge above, escaping to the surface in regions where oceanic crust-continental crust contact eliminates the wave-guide effect. Type I events in Cascadia occur at depths where the slab is presumably below the mantle wedge so this model is viable assuming the oceanic crust has a sufficiently lower velocity than the wedge to internally reflect a significant fraction of incident energy. Indeed, this interpretation was suggested by *Mundal et al.* (1990) for Cascadia X arrivals in his study.

A good fit to travel times was achieved for a oceanic crustal wave-guide having average velocity near 5.9 km/s, considerably lower than expected for typical oceanic crust (Figure 4.12) In contrast, the secondary arrivals observed in southwest Japan had apparent velocities of $\sim$ 6.7 km/s, much closer to the expected velocities of un-transformed basalt and gabbro. One may suppose that the oceanic crust in Cascadia has anomalously low velocities, perhaps due to a thick sediment layer or high H_2O concentrations. However, *Preston et al.* (2003a) tested the resolution of their tomographic inversion to see if a -6% low-velocity oceanic crust would have been detected if it existed beneath western Washington. They concluded that down to depths near 50 km, such a low-velocity layer would have appeared in the tomography, but one is not observed.

The other problem with the wave-guide hypothesis for Cascadia is the lack of secondary S, which were prominently observed in Japan and are expected since P and S paths will be nearly identical.
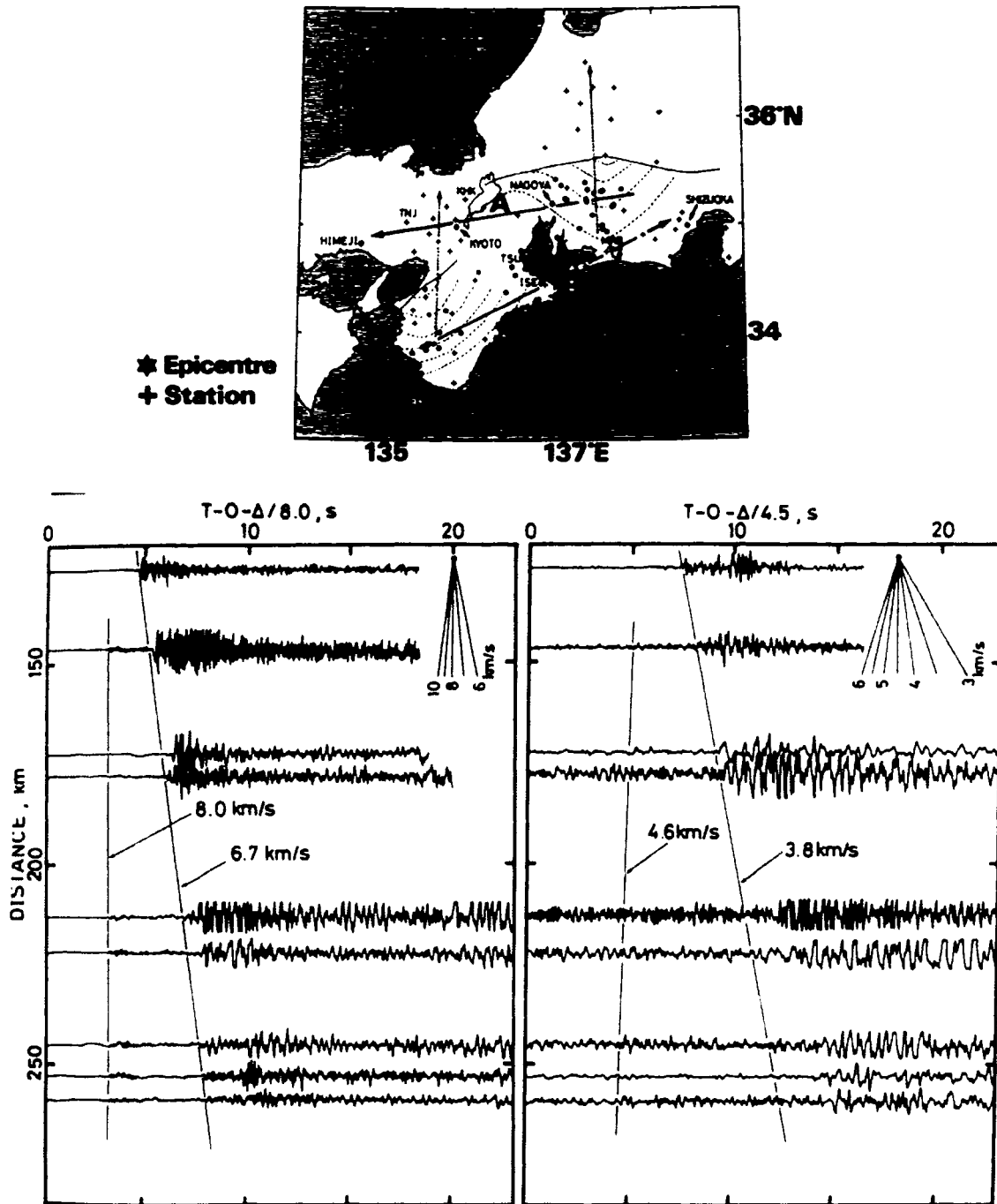
Figure 4.11: Secondary P arrivals in southwest Japan (left) were interpreted to be energy trapped in low-velocity oceanic crust. Note the prominent secondary S (right).
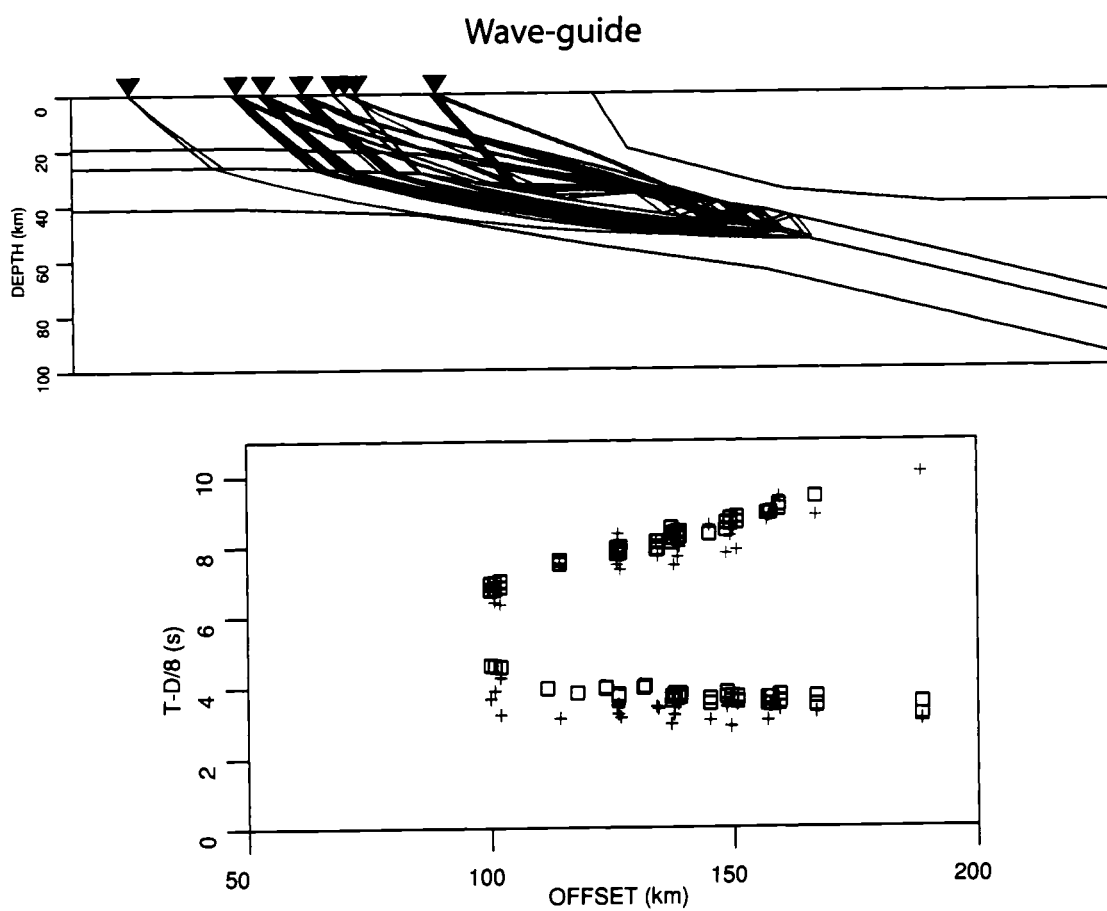
Wave-guide

Figure 4.12: Good fit to the travel times was achieved with this model but the oceanic crust required an average velocity < 6 km/s.

Case 2: Direct P

If the mantle wedge has velocities equal to or lower than the oceanic crust in the vicinity of type I earthquakes, the oceanic crust cannot act as a wave-guide since no energy will be critically reflected. The possibility then exists for P-waves to take a direct path through the mantle wedge and continental crust. This case is essentially the P_n/P_g pair commonly observed from shallow and mid-crustal earthquakes. Petrologically, this scenario could exist if eclogitization has increased the average velocity of the oceanic crust.

Ray tracing showed that in order for direct P to reach observed station distances and still be confined to the wedge and continental crust, a mechanism for directing rays to near horizontal paths in the mid to lower crust was needed (Figure 4.13). The negative velocity gradient, $\frac{\partial v}{\partial z}$, described in Section 4.2.2 causes upgoing rays emerging from the ocean crust to turn away from vertical, but not to the extent necessary. Trial and error adjustments to the negative gradient region were made until rays were refracted sufficiently downward to reach the required station distances. This ultimately required increasing velocities in the mid-crust (the top of the negative gradient region) to upper mantle values ($\sim$ 8 km/s) which is not observed in tomographic models. Additionally, while apparent velocities could be well fit to observations, the X-P delay time was 1-2 seconds less than observed. Many combinations of velocities in the oceanic crust, mantle wedge and continental crust were tried, but none produced good fit to the data.

Case 3: Underside Reflection

Another possibility for directing P waves to near horizontal paths through the Olympic Core Rocks is an underside reflection. The dipping interface between the low-velocity Olympic Core rocks and the high-velocity Cresent basalts could provide the necessary discontinuity. Excellent travel-time fit was achieved using this model for earthquakes
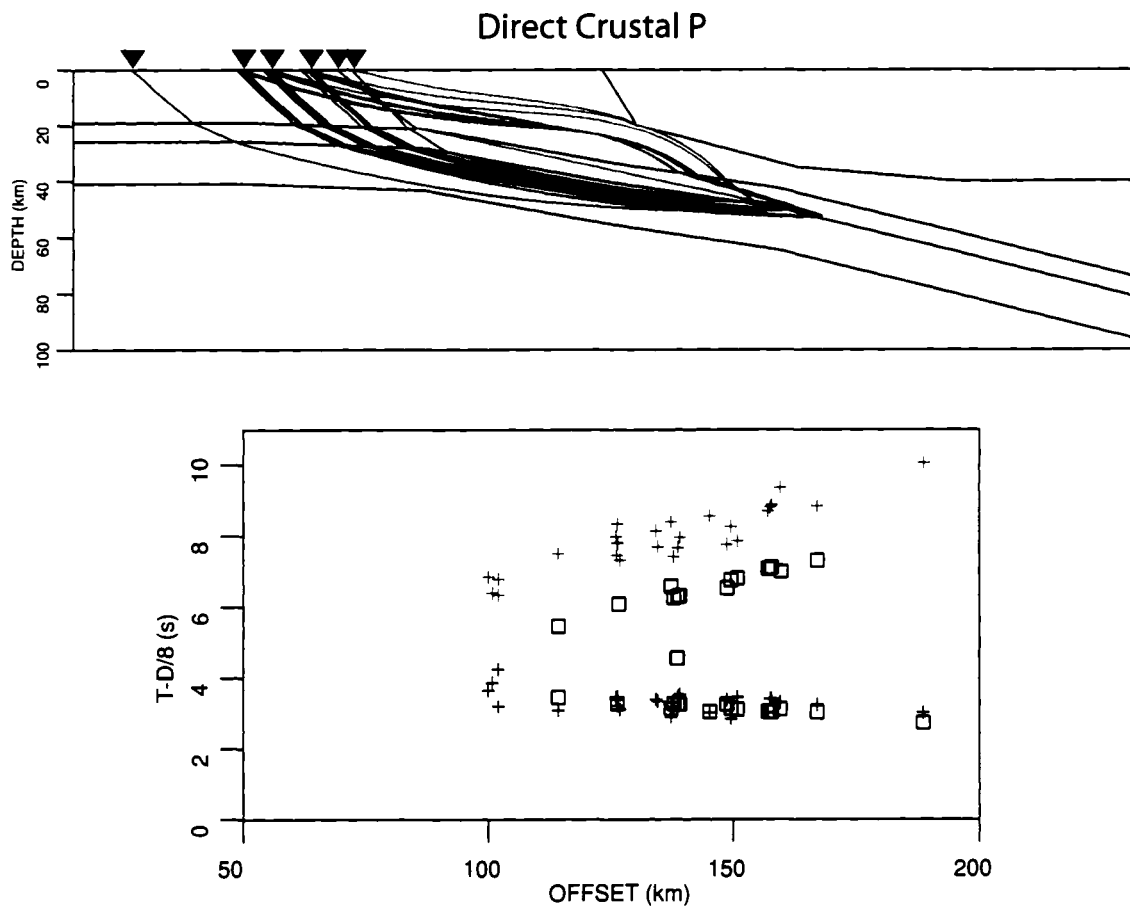
Direct Crustal P

Figure 4.13: Unrealistic velocity gradients were necessary to direct energy out to the required station distances and although the apparent velocity could be fit, travel times are $\sim$ 2 s early.

directly beneath the reflector, but ray paths from events further downdip could not be easily produced that would reflect off the steeply dipping layer (Figure 4.14). This hypothesis can be tested by examination of station-common apparent velocities to a suite of earthquakes, essentially reversing the designation of sources and receivers. In Figure 4.15 , "receivers" are assumed to be collinear, dipping parallel to the subducted plate so that the station-common apparent velocity is the speed which energy would appear to travel parallel to the slab from a surface "source". Assuming the reflector is directly above the "receivers", rays are steeply incident to the "receivers" producing high apparent velocities. For the case shown in Figure 4.15, station-common apparent velocity is predicted to be > 9 km/s, but station-common travel-time data for the three stations shown are significantly lower, ranging from approximately 6 to 8 km/s. While it was assumed that earthquakes ("receivers") were collinear and slab parallel, in truth, type I earthquakes vary somewhat in their relative position to the slab. However, observed minus predicted travel times approach 2 seconds for the farthest source-receiver offsets. To achieve agreement would require shallowing earthquakes by as much as 15 km which is not possible. This test therefore shows that X cannot be an underside reflection as modeled. Again, as with the wave-guide model, any interpretation that involves a P wave taking some alternate path than the one taken by first arrival requires a mechanism by which a corresponding secondary S is not observed.

Case 4: SP Conversion at Slab-Wedge Interface

A near-source SP conversion is a fourth possibility and is consistent with the lack of observed secondary S. This model results in the best travel-time fit of all the models tested that use reasonable crustal velocities (Figure 4.16). Converted SP waves emerge with nearly horizontal paths and are further turned downward or trapped in the low-velocity zone formed by Olympic Core rocks underthrusting Cresest basalts (Section 4.2.2). The correct delay time between P and X is achieved by the ray
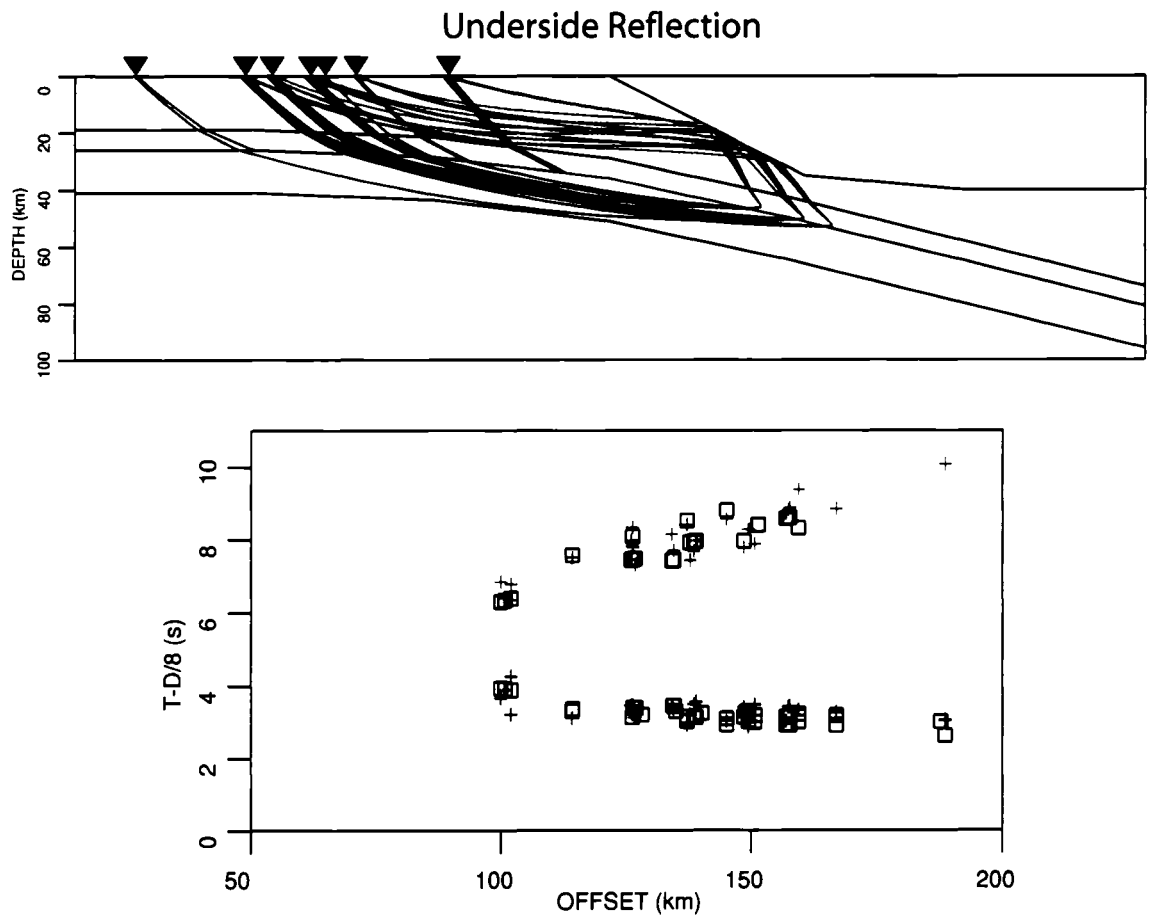
Underside Reflection

Figure 4.14: We model here reflections off the Olympic Core - Cresent Basalt interface. Very good travel-time fit is achieved but an explanation for the lack of secondary S is needed. Further, as shown in Figure 4.15, station-common apparent velocity does not fit observed times.
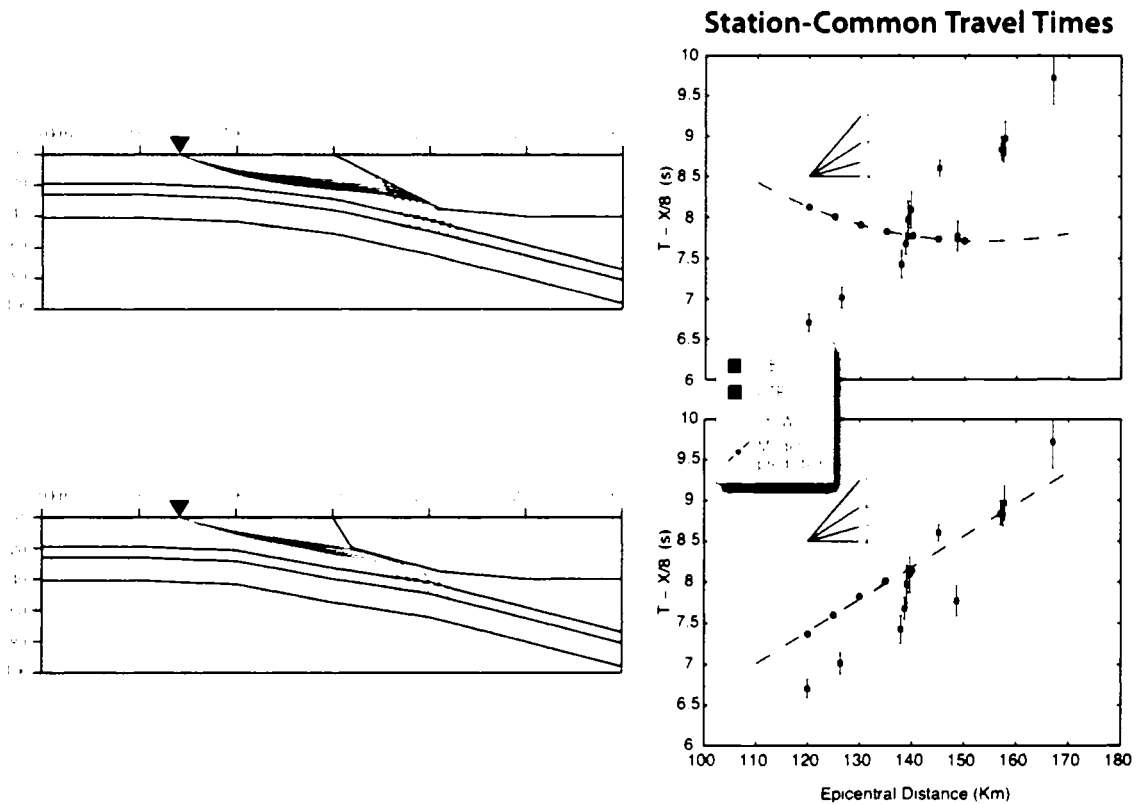
Station-Common Travel Times

Figure 4.15: Station-common apparent velocities for 3 stations are 6.0, 6.0 and 7.0, re-spectively. Ray-tracing for SP conversion shows good agreement with station-common apparent velocity, but underside reflections predicts apparent velocity > 9 km/s.

traveling for part of its path as S. Station-common apparent velocities predicted by an SP conversion are also consistent with observations.

X amplitudes are quite large, often several times that of P, requiring a substantial fraction of S energy to convert to P at the interface. Assuming mid 7 oceanic crust P velocities, low 6 mantle wedge velocities, densities of 3.3 and 2.7 g/cm^3, respectively, and a high Poisson's ratio (~ 0.30) for the mantle wedge (*Christensen*, 1996), near critically refracted S to P waves reach approximately 45% conversion efficiency, dropping sharply as incident waves diverge from the critical angle of incidence. Earthquakes typically produces approximately 6 times more S energy than P energy (*Aki*
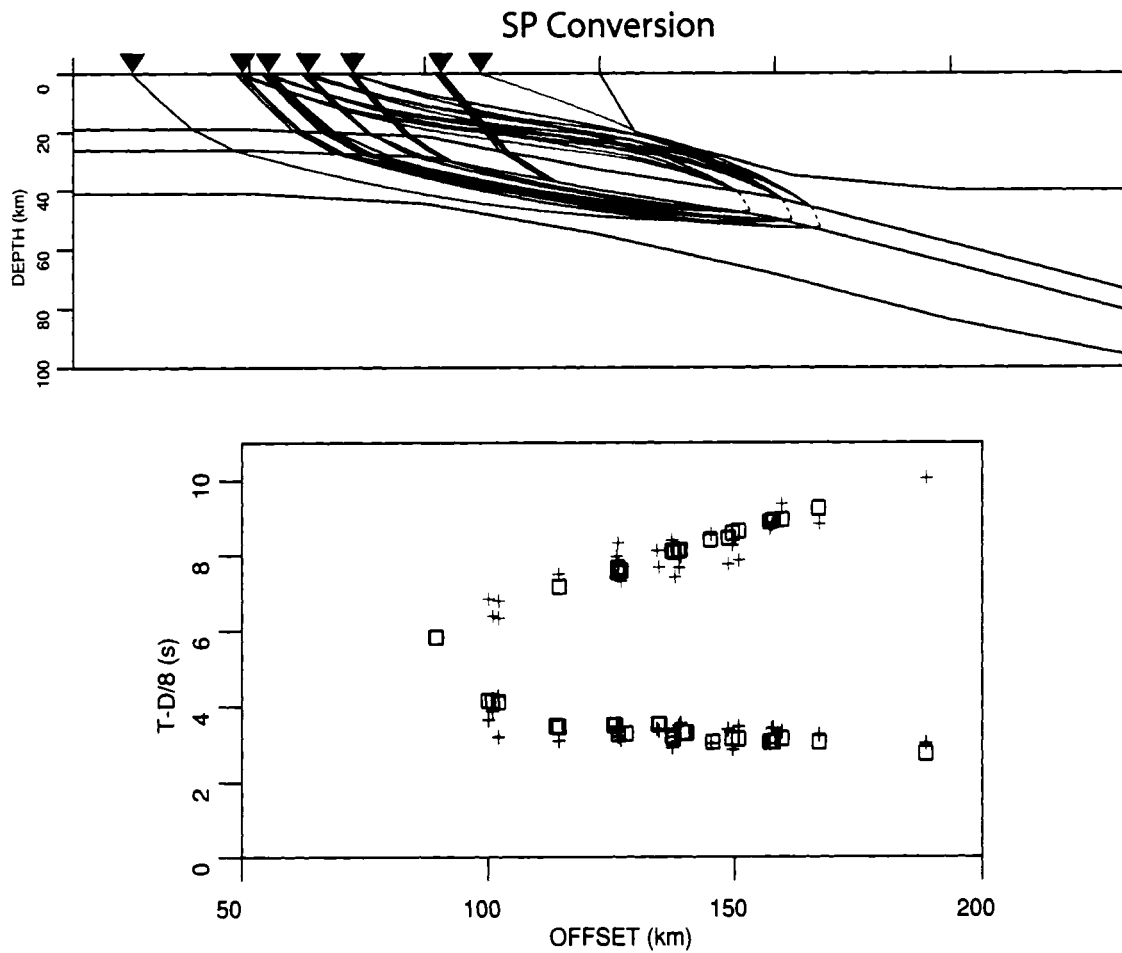
Figure 4.16: This is our favored model as travel-times is fit well with reasonable crustal velocity estimates and explains the absence of secondary S. Figure 4.15 also shows good agreement to station-common apparent velocity.

and Richards, 2002, Equation 4.96) so this level of conversion would likely produce a large amplitude converted P if incident angles are near critical. Figure 4.17 shows
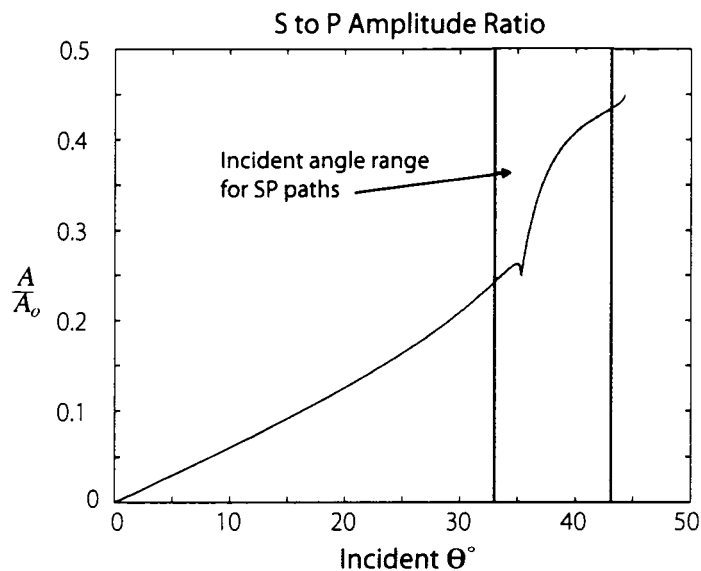
Figure 4.17: Assuming eclogitization of the oceanic crust and serpentinization of the lower mantle wedge, a discontinuity exists that transmits approximately 45% of incident S to P at the S critical incident angle. Results from ray-tracing show incident angles approaching critical, producing between 25 to 43% SP conversion.

that the range of S incident angles on the converting interface measured from ray tracing will result in 25 to 43% conversion to P. While this is an appreciable fraction, X amplitudes are often 5-10 times that of P. This may be because P first arrivals are head waves, which typically have low amplitude, or there is additional amplification of the converted P waves as they are wave-guided in the low-velocity Olympic Core Rocks.

Chapter 5

INTERPRETATION AND DISCUSSION

The additional constraints we placed on the subducting Juan de Fuca slab beneath Western Washington have provided a more clear picture of Cascadia seismicity in terms of the location of intraslab earthquakes relative to the plate, particularly the clear pattern of upper mantle seismicity discussed in Section 3.4. We present evidence for a new interpretation of Cascadia upper mantle seismicity: the manifestion of a subducted pseudofault.

Additionally, the "tighter" arch places the shallowest dipping portion of the slab directly beneath the Olympic Mountains which suggests a relationship between these two structures. Finally, our interpretation of the secondary phase observed from some of the intraslab earthquakes as an SP conversion at the top of the plate requires a velocity discontinuity that we interpret as evidence of eclogitization of the oceanic crust and serpentinization of the lower mantle wedge.

5.1 Upper Mantle Earthquakes: Evidence of a Subducted Pseudofault

The linear trend along which most of the upper mantle seismicity occurs (Figure 3.6) trends more northerly than the convergence direction and does not coincide with any obvious feature in slab geometry. This suggests that this lineament is not a permanent feature such that seismicity in the plate occurs as it passes through this region, but rather an anomaly in the plate fabric. In other subduction zones (e.g. Chile, Costa Rica and NE Japan), lineaments of intraslab earthquakes have been linked to subducted seamount chains (*Yamazaki*, 2000) but no such features are evident in the bathymetry of the Juan de Fuca plate.

Offsets in magnetic anomalies are, however, observed (*Wilson*, 2002) and interpreted as pseudofaults caused by the southward propagation of the Juan de Fuca rift (*Hey*, 1977, 2005). One such pseudofault is projected to lie beneath the Olympic Peninsula roughly coincident the upper mantle seismicity there (Figure 5.1). Could this pseudofault be related to this intraslab seismic lineament? To address this possibility, some understanding of upper mantle earthquake source mechanisms and pseudofault characteristics is needed. Additionally, the pseudofault projection is nearly coicident with the seismicity, but not exactly. For them to be related, uncertainty in the pseudofault location must be sufficient to allow colinearity.

5.1.1 Pseudofault Position Uncertainty

We first consider the uncertainty in pseudofault position. Sea-floor magnetic anomaly data exists to isochron 4A (Figure 5.1) so we are primarily interested in the isochron uncertainties between 4A and 5B (9 to 14 Ma). Isochrons beneath the North American plate were projected by assuming symmetric and orthogonal spreading and are subject to uncertainties in plate motion and spreading rate. These uncertainties are estimated at $3 - 5°$ in plate motion and 10-15% in full spreading rate (*Wilson, pers. comm.*). Combining these effects results in the uncertainties shown in Figure 5.2. Within uncertainties, then, the pseudofault zone in question and the lineament of upper mantle seismicity are coincident.

5.1.2 Upper Mantle Earthquake Source Process: Dehydration Embrittlement

Several authors have suggested dehydration embrittlement of hydrated upper mantle peridotite as the primary mechanism for intermediate-depth mantle earthquakes (*Kirby et al.*, 1996; *Wang*, 2002). A key element of this hypothesis is the presence of hydrous minerals, requiring fluid pathways to mantle depths. The low-porosity of basalt and gabbro in the oceanic crust requires that fracture related permeability be the controlling factor for water penetration to mantle depth (*Lowell and Rona*, 2005).

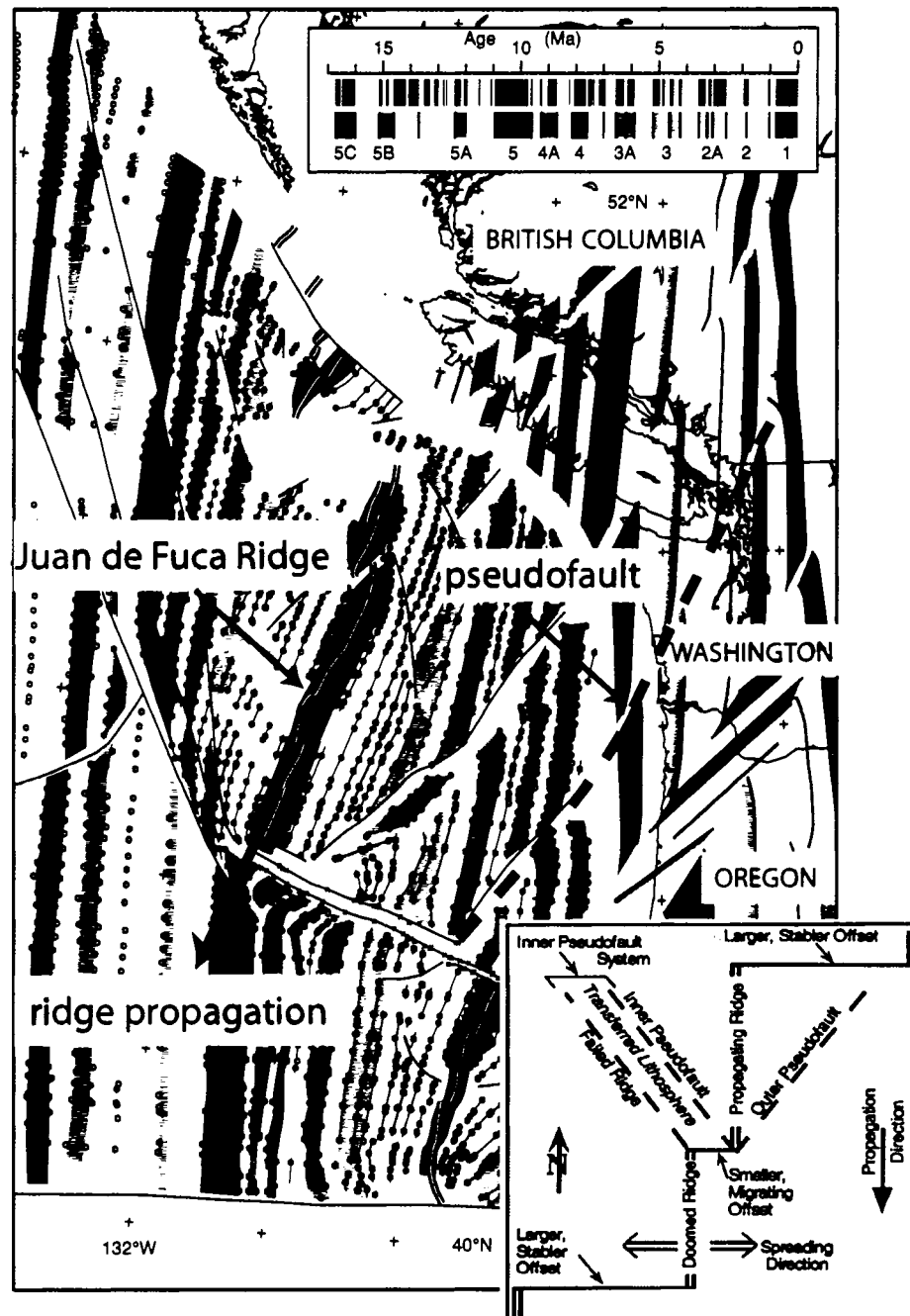Figure 5.1: Sea-floor age map from magnetic anomalies (taken from *Wilson* (2002)). Propagating Juan de Fuca ridge creates pseudofaults, one of which subducts beneath the Olympic Peninsula.
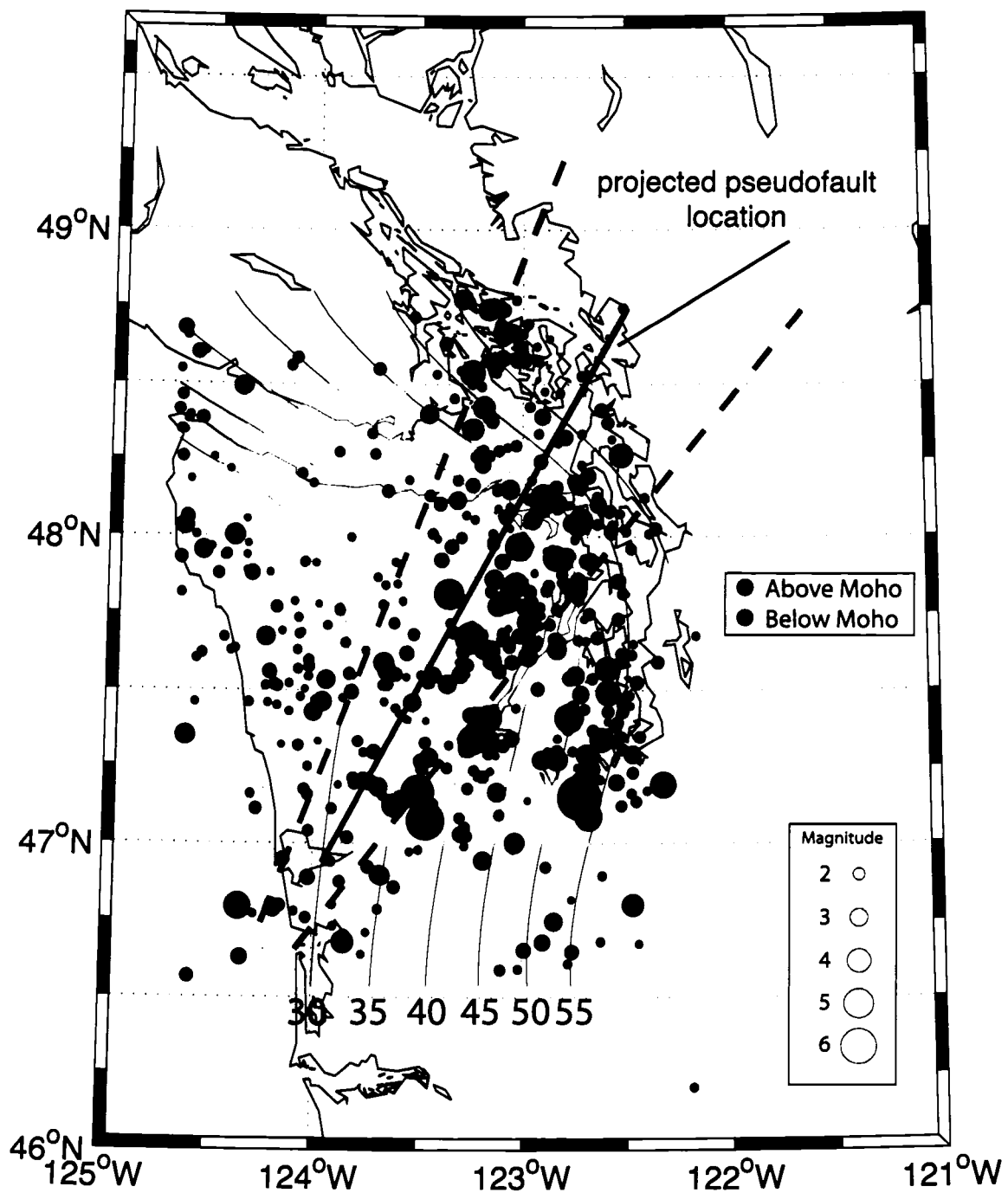
Figure 5.2: Solid line is projection of pseudofault with dashed lines representing approximate uncertainty due to uncertainty in convergence direction and rate. Zone of upper mantle seismicity lies within pseudofault zone uncertainty.

If indeed dehydration embrittlement is the primary source of upper mantle seismicity, it is reasonable to assume high levels of seismicity would occur in heavily hydrated portions of subducting slabs.

5.1.3 Serpentine Along Juan de Fuca Pseudofaults

Pseudofaults are characterized by a zone of highly deformed lithosphere and potentially provide the deep fractures necessary for upper mantle hydration. *McClymont and Clowes* (2005) modeled anomalously low P-wave velocities and gravity lows along Juan de Fuca pseudofaults as the result of significant levels of serpentine in the upper mantle peridotite (25-30% by volume). This provides strong support for our hypothesis that the distribution of upper mantle seismicity in Cascadia is a direct manifestation of a subducting pseudofault.

5.2 Reflection Distribution

Wide-angle reflections are observed off the shallowest dipping section of the slab beneath western Washington. This is likely a geometric consequence of source and receiver positions. As the slab steepens, deeper sources are required to produce critical reflections which is limited by the hypocenter distribution of shallow and midcrustal earthquakes. This may also be indicative of eclogitization of the oceanic crust so that no appreciable velocity contrasts exists at its base. The depth range where eclogitization is thought to occur in Cascadia is also approximately where the slab steepens to the east beneath Puget Sound. It is therefore difficult to know how much of the observed absence of reflections in this region is due to geometric or rheologic effects.

The most southerly group of reflections are at the southern terminus of Puget Sound, in the vicinity of the Nisqually earthquake and directly west. It is just south of this latitude where a slab tear has been proposed. The lack of reflections to the south could indicate a fundamental change in the slab or is simply a result of

slab steepening creating the geometric limitations previously discussed. The abrupt absence of reflections to the south is therefore consistent with a slab tear, but is not direct evidence of one.

5.3 Oceanic Crustal Earthquakes

Preston et al. (2003a) give a detailed presentation of current models for seismogenesis in the downgoing crust and slab upper mantle of subduction zones. The basalt to eclogite transformation with its associated densification and dewatering is believed to be at least partially responsible for earthquakes in the oceanic crust (*Kirby et al.*, 2002), but since crustal earthquakes are not ubiquitous in Cascadia, other conditions must be present.

The lack of oceanic crustal earthquakes across the top of the arch indicates that the basalt to eclogite transformation is occurring aseismically since we assume the phase change is occurring. This may be related to the shallow dip of the slab since the basaltic crust enters the eclogite P-T field more gradually. Also because of a more shallow dip, the slab along the top of the arch in the 45-60 km depth range is further from the trench than material at the same depth on the flanks, providing more time to gradually release water prior to entering the eclogite field.

This explanation does not, however, explain why seismicity in the oceanic crust is low or absent at the steeper dipping regions of the slab beneath the northern Georgia Strait, southwest Washington and Oregon. *Rogers* (1983) argued that in the more steeply dipping regions, basalts and gabbros in the crust persist metastably to higher temperature regimes such that the phase change to eclogite occurs at temperatures where rocks are heated beyond their ability to support brittle failure.

It is reasonable to also assume increased deviatoric stress caused by the warping of the slab in the vicinity of the arch may also be playing a role. *Chiao and Creager* (2002) produced a strain-rate model of the Cascadia arch assuming Newtonian rheology and it predicts anomalous strain rates across the entire arch.

It would appear that earthquakes caused by brittle failure due to the basalt to eclogite phase change are the exception rather than the rule in Cascadia, made possible only by 1) entering the eclogite field at the correct rate and 2) the increased strain rate on the arch.

5.4 Secondary P-wave

5.4.1 Eclogitization, Serpentinizaton and Seismicity

Our interpretation of the secondary P phase observed from some intraslab earthquakes as SP conversions at the top of the JDF plate requires a velocity contrast at the interface. In Alaska (*Helffrich and Abers*, 1997) and Japan (*Matsuzawa et al.*, 1990), SP conversions at the top of the subducting plate were attributed to a relatively low-velocity crust capped by higher-velocity mantle wedge. In contrast, our model suggests a high-velocity crust and low-velocity wedge. The existence of the the secondary phase indicates eclogitization of the oceanic crust, increasing S-wave velocities to $\approx$ 4.6 km/s combined with serpentinization of the mantle wedge which significantly decreases S-wave velocities to $\approx$ 3 km/s (*Bostock et al.*, 2002). Because eclogitization involves dewatering of the basaltic crust and serpentinization requires hydration of peridotite, it is not surprising to have these two lithologies juxtaposed as required by our model. The location of the type I events imposes constraint on the minimum westward extent of the mantle wedge and where the oceanic crust has transformed to eclogite (Figure 5.3).

What does this tell us about the seismicity where type I earthquakes occur? Our slab depth model could not resolve whether type I events occur in the oceanic crust or slab mantle and our secondary phase interpretation does not depend on the position of earthquakes relative to the slab Moho. Our secondary phase interpretation does, however, require an associative relationship between eclogitization of the crust and the location of type I events, suggesting a causal relationship. What about the
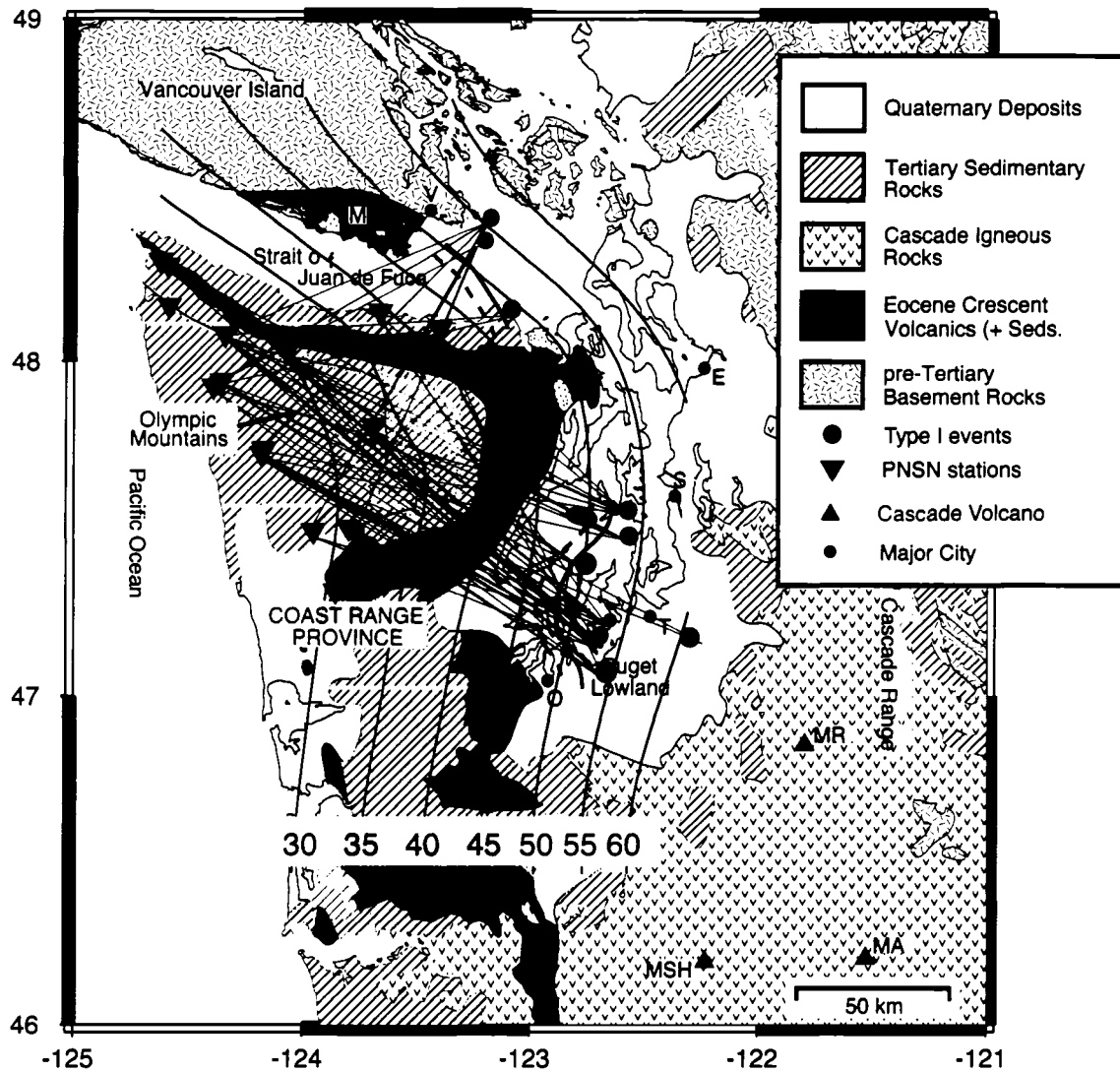
Figure 5.3: Source-receiver geometries producing X are indictated by red connecting lines. All paths travel below the Cresent basalts and through the Olympic Core. The blue lines indicate our inferred minimum updip extent of oceanic crust eclogitization (solid) and mantle wedge serpentinization (dashed).

largest recorded ($>$ $M6$) intraslab earthquakes? They have all occurred within the "type I regions" but no secondary phase is observed due to their large magnitude (Section 4.1.1). Furthermore, relative earthquake relocations show the largest events to be occurring deeper (*Cassidy and Waldhauser*, 2003) relative to the subducting slab, than smaller events . If the largest events are at least partially rupturing in the crust, this would suggest they are associated with eclogitization of the gabbros which perhaps are able to support greater stress than the more fractured pillow basalts of the upper crust. This would not, however, preclude these events from rupturing across the Moho.

5.4.2 Influence of Cresent Basalts

Ray-tracing (Section 4.2) showed that SP converted energy, even for near critical refractions, would not be observed at the offsets of the Olympic Peninsula stations without directing it toward horizontal for part of its path. Our interpretation is that a wave-guide is formed, not from the oceanic crust, but from accretionary sediments underthrusting the Eocene volcanics (Cresents), and acts to focus energy to Olympic Peninsula stations. To summarize, X is only observed when three criteria are met: 1) eclogitization of the oceanic crust has occurred 2) the overlying mantle wedge is serpentinized and 3) a low-velocity wave guide is formed by sediments underthrusting high-velocity volcanics (Figure 5.3).

At the northeast tip of the seismic lineament attributed to the subducting pseudo-fault (Section 5.1), earthquakes occur within the eclogitization depth range and locate within the oceanic crust, but do not produce an observable X phase on Olympic stations. Cresent basalts lie between these events and Olympic stations so the wave-guide "cap" exists if low-velocity sediments are present. Tomography shows evidence of sedimentary "lobes" being subducted (Crosson, *pers. comm*) so perhaps this region is "lobeless" such that no wave-guide is produced. Another possibility is that no appreciable SP energy is produced at the plate interface due to the lack of a velocity

discontinuitiy. Because this part of the plate is further from the trench than the plate on the arch flanks at the same depth, and therefore has been subducting longer, it may be that the oceanic crust has dewatered prior to contact with the mantle wedge such that serpentinization is minimal. Or, perhaps eclogitization is delayed because of warmer temperatures across the slab arch. Additional investigation would be necessary to answer this question.

5.5 Future Work

An improved slab geometry was produced in this study by including reflection data from earthquakes and produced some intriguing results, however the data was sparse and of mixed quality. Four key results provide an impetus for future work: 1) the apparent tightening of the arch beneath the Olympic Mountains 2) upper mantle seismicity as the result of a subducting pseudofault 3) a secondary P phase as an indication of eclogitization of the oceanic crust and serpentinization of the the upper mantle and 4) the absence of reflections south of the intraslab earthquake region.

Juan de Fuca slab geometry could be further constrained beneath the Olympic Peninsula by firstly improving the 3-D velocity model. 3-D tomography studies, e.g. *Preston et al.* (2003a), suffer poor ray coverage through the Olympic Core, severely reducing resolution. Models derived from forward travel-time calculations, such as our slab model, though the Olympics are therefore subject to this uncertainty. Difficult terrain and a dearth of seismicity on the Olympic Peninsula have thus far prevented the desired high-resolution tomography.

The addition of earthquake-source reflections has highlighted regions where we expect to see slab reflections and regions that we would like to know more about. In particular, a causal relationship between the slab arch and formation of the Olympic Mountains is suggested by the shallow dip of the arch directly beneath them. An improved slab model in this region could presumably resolve this important question.

Additionally, the possibility of a slab tear near the southern terminus of Cascadia

seismicity remains unresolved and could be investigated with targeted active and passive experiments. This southern Puget Sound region, containing the largest intraslab earthquakes remains a focus of interest. Unresolved is whether these large earthquakes are confined exclusively to the oceanic crust or rupture partially or entirely in the subducted mantle. Such knowledge would help place upper magnitude bounds on future earthquakes. Refinement of the slab geometry and improved hypocenter locations could eventually lead to an event by event determination of which earthquakes occur in the oceanic crust and which are in the upper mantle. This is a key component to further our understanding of Cascadia intraslab seismicity in terms of why earthquakes occur where they do.

Finally, the causal relationship we presented between a subducted pseudofault and upper mantle seismicity is exciting because it presents a new view of Cascadia seismicity and the role of fluids. Are the largest intraslab earthquakes also the result of highly hydrated regions of the plate? Much work has been done recently with so-called silent earthquakes and deep tremor in Cascadia (*Rogers and Dragert*, 2003). Hypotheses about the nature of these phenomena have included fluid migration. Could the excess hydration of this and other subducted pseudofaults be a driving mechanism? This remains a very active field of research.

BIBLIOGRAPHY

Abers, G. A., and G. Sarker (1996), Dispersion of regional body waves at 100-150 km depth beneath Alaska; in situ constraints on metamorphism of subducted crust, *Geophys. Res. Lett.*, *23*(10), 1171–1174.

Adams, J., and S. Halchuk (2000), Knowledge of in-slab earthquakes needed to improve seismic hazard estimates for southwestern british columbia, in *Proceedings of the Geological Society of America Penrose Conference: Great Cascadia Earthquake Tricentennial.*

Aki, K., and P. G. Richards (2002), *Quantitative Seismology*, 2nd ed., University Science Books.

Baker, G. E., and C. A. Langston (1987), Source parameters of the 1949 magnitude 7.1 south Puget Sound, Washington, earthquake as determined from long-period body waves and strong motion, *Bull. Seism. Soc. Am.*, *77*, 1530–1557.

Bebout, G. E., D. W. Scholl, S. H. Kirby, and J. P. Platt (1996), Preface, in *Subduction Top to Bottom*, edited by G. E. Bebout, D. W. Scholl, S. H. Kirby, and J. P. Platt, Geophysical Monograph Series, American Geophysical Union.

Bostock, M. G., R. D. Hyndman, S. Rondenay, and S. M. Peacock (2002), An inverted continental Moho and the serpentinization of the forearc mantle, *Nature Lett.*, *417*, 536–538.

Brocher, T. M., T. Parsons, A. M. Trehu, C. M. Snelson, and M. A. Fisher (2003), Seismic evidence for widespread serpentinized forearc upper mantle along the cascadia margin, *Geology*, *31*(3), 267–270.

Calvert, A. J., and R. M. Clowes (1990), Deep, high amplitude reflections from a major shear zone above the subducting Juan de Fuca Plate, *Geology*, *18*, 1091–1094.

Cassidy, J. F., and R. M. Ellis (1993), S wave velocity structure of the northern Cascadia subduction zone, *J. Geophys. Res.*, *98*(B3), 4407–4421.

Cassidy, J. F., and F. Waldhauser (2003), Evidence for both crustal and mantle earthquakes in the subducting Juan de Fuca plate, *Geophys. Res. Lett.*, *30*(2), 1095, doi:10.1029/2002GL015511.

Chiao, L.-Y., and K. C. Creager (2002), Geometry and membrane deformation rate of the subducting cascadia slab, in *The Cascadia Subduction Zone and Related Subduction Systems; Seismic Structure, Intraslab Earthquakes and Processes, and Earthquake Hazards*, edited by S. Kirby, K. Wang, and S. Dunlop, pp. 47–54, U.S. Geological Survey Open-File Report 02-328 and Geological Survey of Canada Open File 4350.

Christensen, N. I. (1996), Poisson's ratio and crustal seismology, *J. Geophys. Res.*, *101*(B2), 3139–3156.

Cohee, B. P., P. G. Somerville, and N. A. Abrahamson (1991), Simulated ground motions for hypothesized M_w =8 subduction earthquakes in Washington and Oregon, *Bull. Seism. Soc. Am.*, *81*(1), 28–56.

Crosson, R. S. (1977), Seismic studies related to regional tectonics in the Pacific Northwest (abstract), *Abstracts with Programs - Geol. Soc. Am.*, *9*(7), 940.

Crosson, R. S. (1983), Review of seismicity in the Puget Sound region from 1970 through 1978, in *Proceedings of Workshop XIV, Earthquake Hazards of the Puget Sound Region, Washington, U.S. Geol. Surv., Open-File Rept. 83-19*, edited by

J. C. Yount and R. S. Crosson, pp. 6–18, U.S. Geological Survey, Menlo Park, California.

Crosson, R. S., and T. J. Owens (1987), Slab geometry of the Cascadia subduction zone beneath Washington from earthquake hypocenters and teleseismic converted waves, *Geophys. Res. Lett.*, *14*(8), 824–827.

DeMets, C., R. G. Gordon, D. F. Argus, and S. Stein (1990), Current plate motions, *Geol. J. Int.*, *101*(2), 425–478.

Flück, P., R. D. Hyndman, and K. Wang (1997), 3-d dislocation model for great earthquakes of the Cascadia subduction zone, *J. Geophys. Res.*, *102*(B9), 20,539–22,550.

Flueh, E.-R., et al. (1998), New seismic images of the Cascadia subduction zone from cruise so108; ORWELL, *Tectonophyics*, *293*, 69–84.

Fukao, Y., S. Hori, and M. Ukawa (1983), A seismological constraint on the depth of basalt-eclogite transition in a subducting oceanic crust, *Nature*, *303*(5916), 413–415.

Goldfinger, C., et al. (2003), Holocene earthquake records from the Cascadia subduction zone and northern San Andreas Fault based on precise dating of offshore turbidites., *Annual Review of Earth and Planetary Sciences*, *31*, 555–577.

Helffrich, G., and G. A. Abers (1997), Slab low-velocity layer in the eastern Aleutian subduction zone, *Geophys. J. Int.*, *130*(3), 640–648.

Hey, R. (1977), A new class of "pseudofaults" and their bearing on plate tectonics; a propagating rift model, *Earth and Planet. Sci. Lett.*, *37*(2), 321–325.

Hey, R. N. (2005), Tectonics; propagating rifts and microplates at mid-ocean ridges,

in *Encyclopedia of Geology*, vol. 5, edited by R. C. Selley, R. M. Cocks, and I. R. Plimer, pp. 396–405, Elsevier Academic Press, Oxford, United Kingdom.

Hori, S., H. Inoue, Y. Fukao, and M. Ukawa (1985), Seismic detection of the untransformed "basaltic" oceanic crust subducting into the mantle, *Geophys. J. R. astr. Soc.*, *83*, 169–197.

Kirby, S., E. R. Engdahl, and R. Denlinger (1996), Intermediate-depth intraslab earthquakes and arc volcanism as physical expressions of crustal and uppermost mantle metamorphism in subducting slabs, in *Subduction Top to Bottom*, edited by G. E. Bebout, D. W. Scholl, S. H. Kirby, and J. P. Platt, Geophysical Monograph Series, pp. 195–214, American Geophysical Union.

Kirby, S. H., R. E. Engdahl, and A. Villasenor (2002), Warm-slab subduction as a global process, in *The Cascadia Subduction Zone and Related Subduction Systems; Seismic Structure, Intraslab Earthquakes and Processes, and Earthquake Hazards*, edited by S. Kirby, K. Wang, and S. Dunlop, pp. 79–80, U.S. Geological Survey Open-File Report 02-328 and Geological Survey of Canada Open File 4350.

Langston, C. A., and D. E. Blum (1977), The April 29, 1965, Puget Sound earthquake and the crustal and upper mantle structure of western Washington, *Bull. Seism. Soc. Am.*, *67*(3), 693–711.

Lapp, D. B., T. J. Owens, and R. S. Crosson (1990), P-waveform analysis for local subduction geometry south of Puget Sound, Washington, *Pure Appl. Geophys.*, *133*(2), 349–365.

Lin, J. W. (1973), A study of upper mantle structure in the Pacific Northwest using P waves from teleseisms, Ph.D. thesis, University of Washington.

Lowell, R. P., and P. A. Rona (2005), Tectonics; hydrothermal activity, in *Encyclo-*

pedia of Geology, vol. 5, edited by R. C. Selley, R. M. Cocks, and I. R. Plimer, pp. 362–372, Elsevier Academic Press, Oxford, United Kingdom.

Matsuzawa, T., T. Kono, A. Hasegawa, and A. Takagi (1990), Subducting plate boundary beneath the northeastern Japan Arc estimated from SP converted waves, *Tectonophyics*, *181*, 123–133.

McClymont, A. F., and R. M. Clowes (2005), Anomalous lithospheric structure of northern juan de fuca plate - a consequence of oceanic rift propagation?, *Tectonophysics*, *406*, 213–231.

McCrory, P. A., S. R. Walter, and R. S. Crosson (2001), Possible discontinuity in Juan de Fuca plate in the vicinity of the 2001 (M6.8) Nisqually earthquake, *Seismol. Res. Lett.*, *72*(3), 91, abstract.

McCrory, P. A., J. L. Blair, D. H. Oppenheimer, and S. R. Walter (2004), Depth to the Juan de Fuca slab beneath the Cascadia subduction margin - A 3-D model for sorting earthquakes, *U.S. Geological Survey Data Series*, *91*.

McKenzie, D. P., and R. L. Parker (1967), The north Pacific; an example of tectonics on a sphere, *Nature (London)*, *216*(5122), 1276–1280.

McNeill, A. F., M. G. Bostock, G. C. Rogers, and J. C. Shragge (2004), The effect of forearc mantle serpentinization on ground motions from megathrust and intraslab events in the Cascadia subduction zone, *Bull. Seism. Soc. Am.*, *94*(1), 147–154.

Michaelson, C. A., and C. S. Weaver (1986), Upper mantle structure from teleseismic P wave arrivals in Washington and northern Oregon, *J. Geophys. Res.*, *91*(B2), 2077–2094.

Miller, K. C., G. R. Keller, J. M. Gridley, J. H. Luetgert, W. D. Mooney, and H. Thybo (1997), Crustal structure along the west flank of the Cascades, western Washington, *J. Geophys. Res.*, *102*(B8), 17,857–17,874, doi:10.1029/97JB00882.

Mundal, I., M. Ukawa, and R. S. Crosson (1990), Normal and anomalous P phases from local earthquakes, and slab structure of the Cascadia subduction zone, unpublished, part of Master's thesis.

Owens, T. J., R. S. Crosson, and M. A. Hendrickson (1988), Constraints on the subduction geometry beneath western Washington from broadband teleseismic waveform modeling, *Bull. Seism. Soc. Am.*, *78*(3), 1319–1334.

Parsons, T., et al. (1998), A new view into the Cascadia subduction zone and volcanic arc; implications for earthquake hazards along the Washington margin, *Geology*, *26*(3), 199–202.

Preston, L. A. (2003b), Simultaneous inversion of 3D velocity structure, hypocenter locations, and reflector geometry in Cascadia, Ph.D. thesis, University of Washington.

Preston, L. A., K. C. Creager, R. S. Crosson, T. M. Brocher, and A. M. Trehu (2003a), Intraslab earthquakes; dehydration of the Cascadia slab, *Science*, *302*, 1197–1199.

R., H. B., S. M. Peacock, G. A. Abers, and S. D. Holloway (2003b), Subduction factory 2. are intermediate-depth earthquakes in subducting slabs linked to metamorphic dehydration reactions?, *J. Geophys. Res.*, *108*(B1), 2030, doi: 10.1029/2001JB001129.

Riddihough, R. P. (1984), Recent movements of the Juan de Fuca plate system, *J. Geophys. Res.*, *89*(B8), 6980–6994.

Rogers, G., and H. Dragert (2003), Episodic tremor and slip on the Cascadia subduction zone; the chatter of silent slip, *Science*, *300*(5627), 1942–1943.

Rogers, G. C. (1983), Seismotectonics of british columbia, Ph.D. thesis, University of British Columbia.

Rogers, G. C., and R. S. Crosson (2002), Intraslab earthquakes beneath Georgia Strait/Puget Sound, in *The Cascadia Subduction Zone and Related Subduction Systems; Seismic Structure, Intraslab Earthquakes and Processes, and Earthquake Hazards*, edited by S. Kirby, K. Wang, and S. Dunlop, pp. 65–67, U.S. Geological Survey Open-File Report 02-328 and Geological Survey of Canada Open File 4350.

Sambridge, M. S., and B. L. N. Kennett (1990), Boundary value ray tracing in a heterogeneous medium; a simple and versatile algorithm, *Geophys. J. Int.*, *101*(1), 157–168.

Satake, K., K. Wang, and B. F. Atwater (2003), Fault slip and seismic moment of the 1700 Cascadia earthquake inferred from Japanese tsunami descriptions, *J. Geophys. Res.*, *108*(B11), 2535, doi:10.1029/2003JB002521.

Shragge, J., M. G. Bostock, and G. C. Rogers (2002), Modeling post-critical Moho reflections from intraslab earthquakes in the Cascadia subduction zone, in *The Cascadia Subduction Zone and Related Subduction Systems; Seismic Structure, Intraslab Earthquakes and Processes, and Earthquake Hazards*, edited by S. Kirby, K. Wang, and S. Dunlop, pp. 43–45, U.S. Geological Survey Open-File Report 02-328 and Geological Survey of Canada Open File 4350.

Strang, G. (1980), *Linear Algebra and Its Applications*, 2nd ed., Harcourt Brace Jovanovich, Inc.

Taber, J. J., and B. T. R. Lewis (1986), Crustal structure of the Washington continental margin from refraction data, *Bull. Seism. Soc. Am.*, *76*(4), 1011–1024.

Taber, J. J., and S. W. Smith (1985), Seismicity and focal mechanisms associated with the subduction of the Juan de Fuca Plate beneath the Olympic Peninsula, Washington, *Bull. Seism. Soc. Am.*, *75*(1), 237–249.

Tatel, H. E., and M. A. Tuve (1955), Seismic exploration of a continental crust, in *Crust of the earth - a symposium*, edited by A. Poldervaart, pp. 35–50, Geol. Soc. Am.

Trehu, A. M., I. Asudeh, T. M. Brocher, J. H. Luetgert, W. D. Mooney, J. L. Nabelek, and Y. Nakamura (1994), Crustal architecture of the Cascadia Forearc, *Science*, *266*(5183), 237–243.

Trehu, A. M., T. M. Brocher, K. C. Creager, M. A. Fisher, L. A. Preston, and G. Spence (2002), Geometry of the subducting Juan de Fuca Plate; new constraints from SHIPS98, in *The Cascadia Subduction Zone and Related Subduction Systems; Seismic Structure, Intraslab Earthquakes and Processes, and Earthquake Hazards*, edited by S. Kirby, K. Wang, and S. Dunlop, pp. 25–32, U.S. Geological Survey Open-File Report 02-328 and Geological Survey of Canada Open File 4350.

Vidale, J. E. (1990), Finite-difference calculation of traveltimes in three dimensions, *Geophysics*, *55*(5), 521–526.

Wang, K. (2002), Unbending combined with dehydration embrittlement as a cause for double and triple seismic zones, *Geophys. Res. Lett.*, *29*(18), 1889, doi: 10.1029/2002GL015441.

Wang, K., and G. C. Rogers (1994), An explanation for the double seismic layers north of the Mendicino triple junction, *Geophys. Res. Lett.*, *21*, 121–124.

Wannamaker, P. E., J. R. Booker, A. G. Jones, A. D. Chave, J. H. Filloux, H. S. Waff, and L. K. Law (1989), Resistivity cross section through the Juan de Fuca subduction system and its tectonic implications, *J. Geophys. Res.*, *94*(10), 14,127–14,144.

Weaver, C. S., and G. E. Baker (1988), Geometry of the Juan de Fuca Plate beneath

Washington and northern Oregon from seismicity, *Bull. Seism. Soc. Am.*, *78*(1), 264–275.

Wilson, D. S. (1993), Confidence intervals for motion and deformation of the Juan de Fuca Plate, *J. Geophys. Res.*, *98*(B9), 16,053–16,071.

Wilson, D. S. (2002), The Juan de Fuca plate and slab: Isochron structure and Cenozoic plate motions, in *The Cascadia Subduction Zone and Related Subduction Systems; Seismic Structure, Intraslab Earthquakes and Processes, and Earthquake Hazards*, edited by S. Kirby, K. Wang, and S. Dunlop, pp. 9–12, U.S. Geological Survey Open-File Report 02-328 and Geological Survey of Canada Open File 4350.

Yamazaki, T. (2000), Interaction between subducting seamounts and overriding fore-arc wedges, and its relation to large earthquakes; a review, *Bull. Geol. Surv. Japan*, *51*, 103–111.

Zelt, C., and R. Smith (1992), Seismic traveltime inversion for 2-d crustal velocity structure, *Geophys. J. Int.*, *108*, 16–34.

Appendix A

TYPE I RECORD SECTIONS
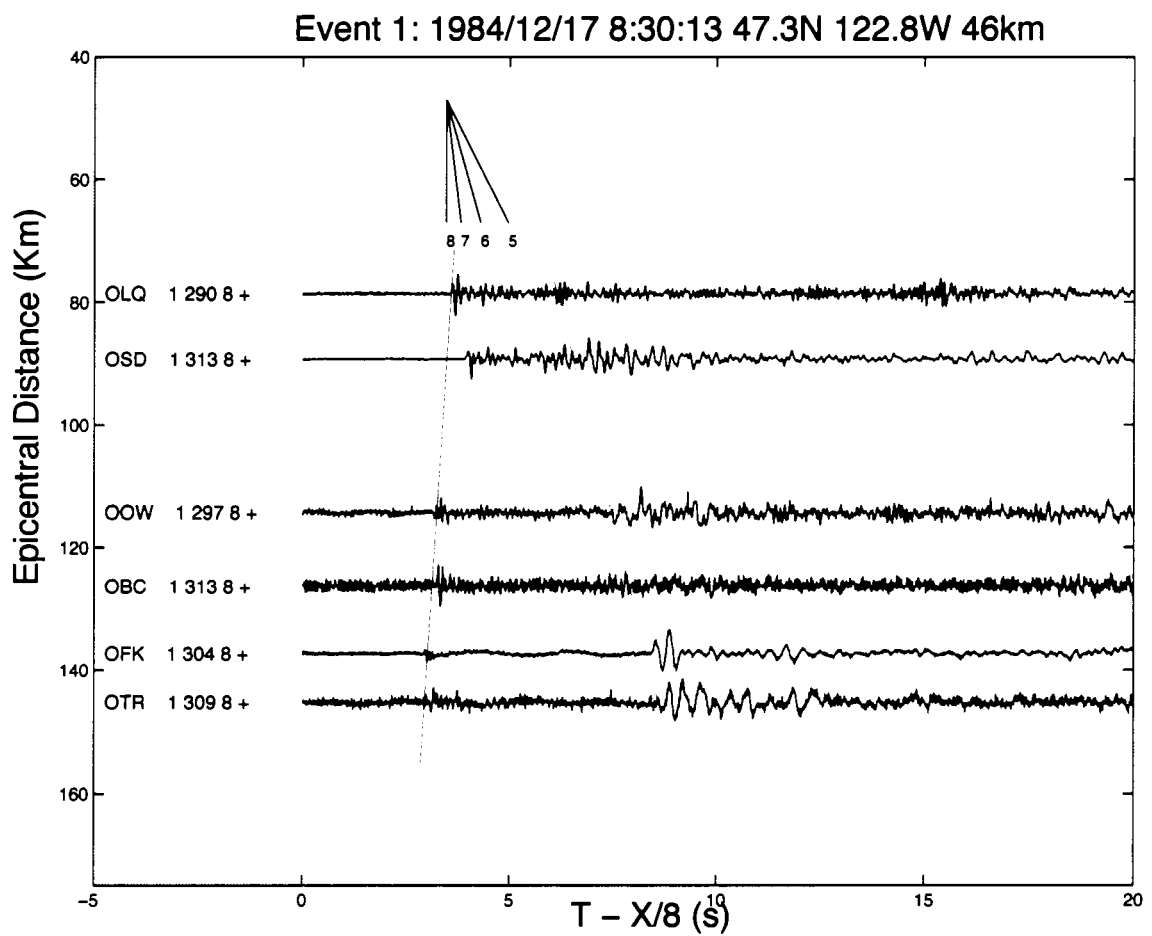
Figure A.1: Event 1: 84121708300
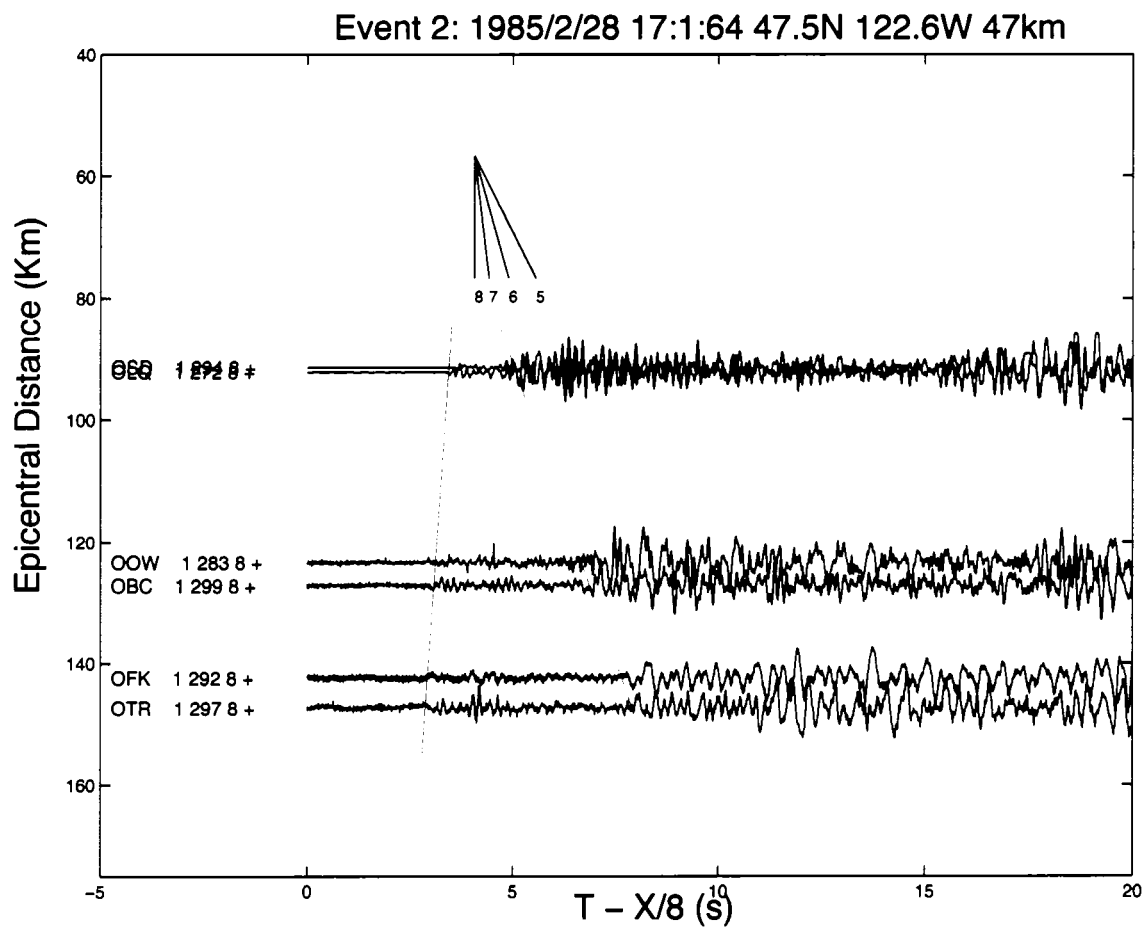
Figure A.2: Event 2: 85022817015

Event 3: 1988/3/11 10:1:26 47.2N 122.3W 65km
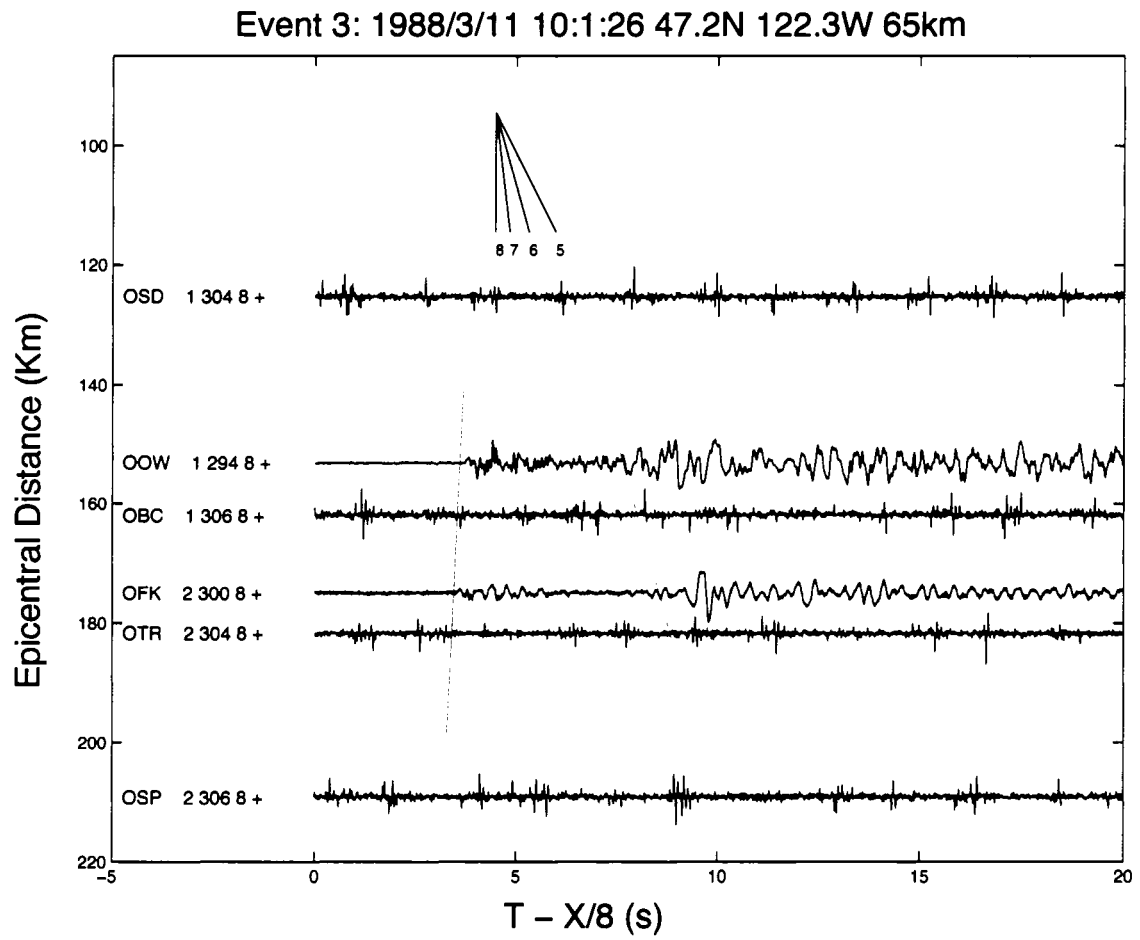
Figure A.3: Event 3: 88031110011
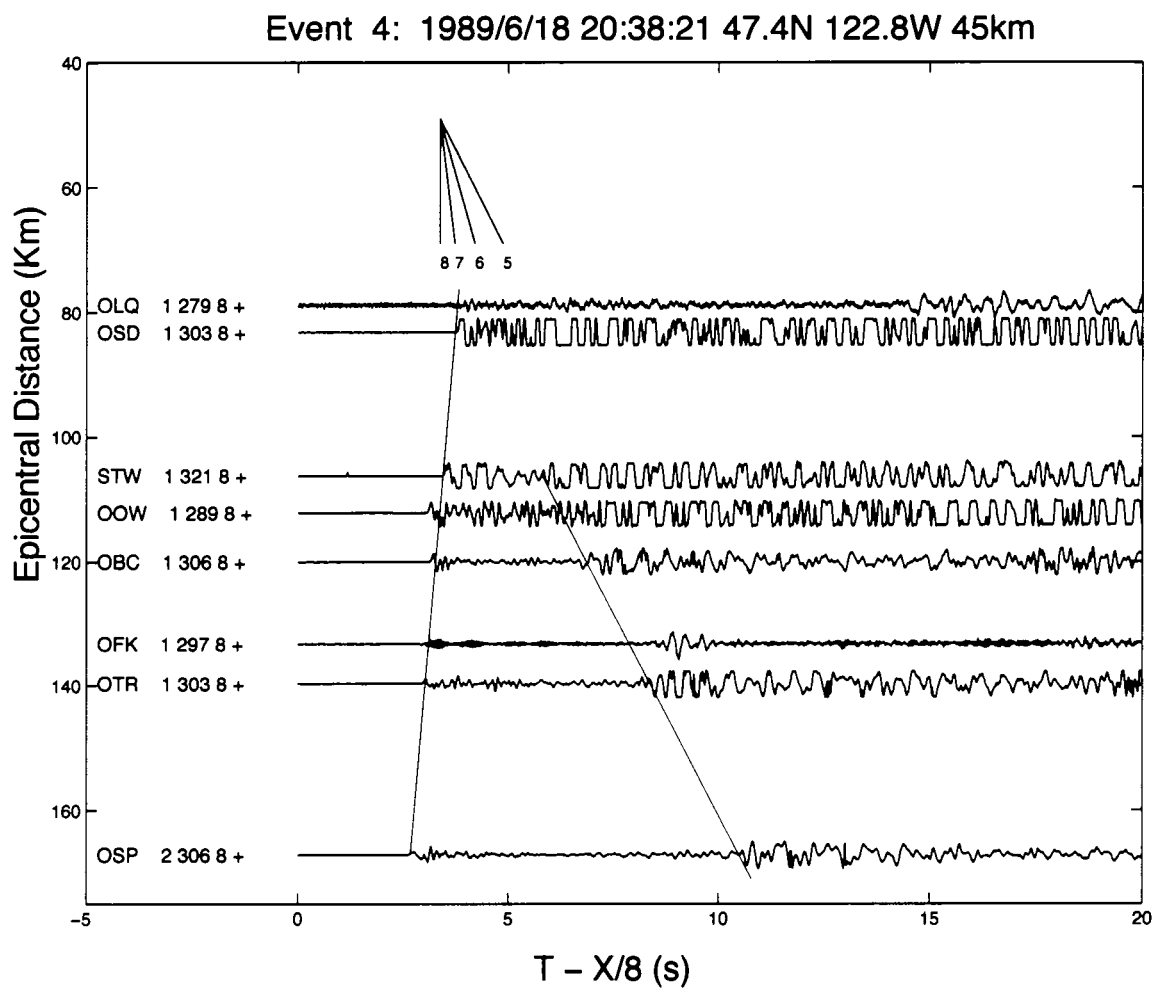
Figure A.4: Event 4: 89061820382

Event 5: 1991/3/16 20:16:59 47.2N 122.7W 49km
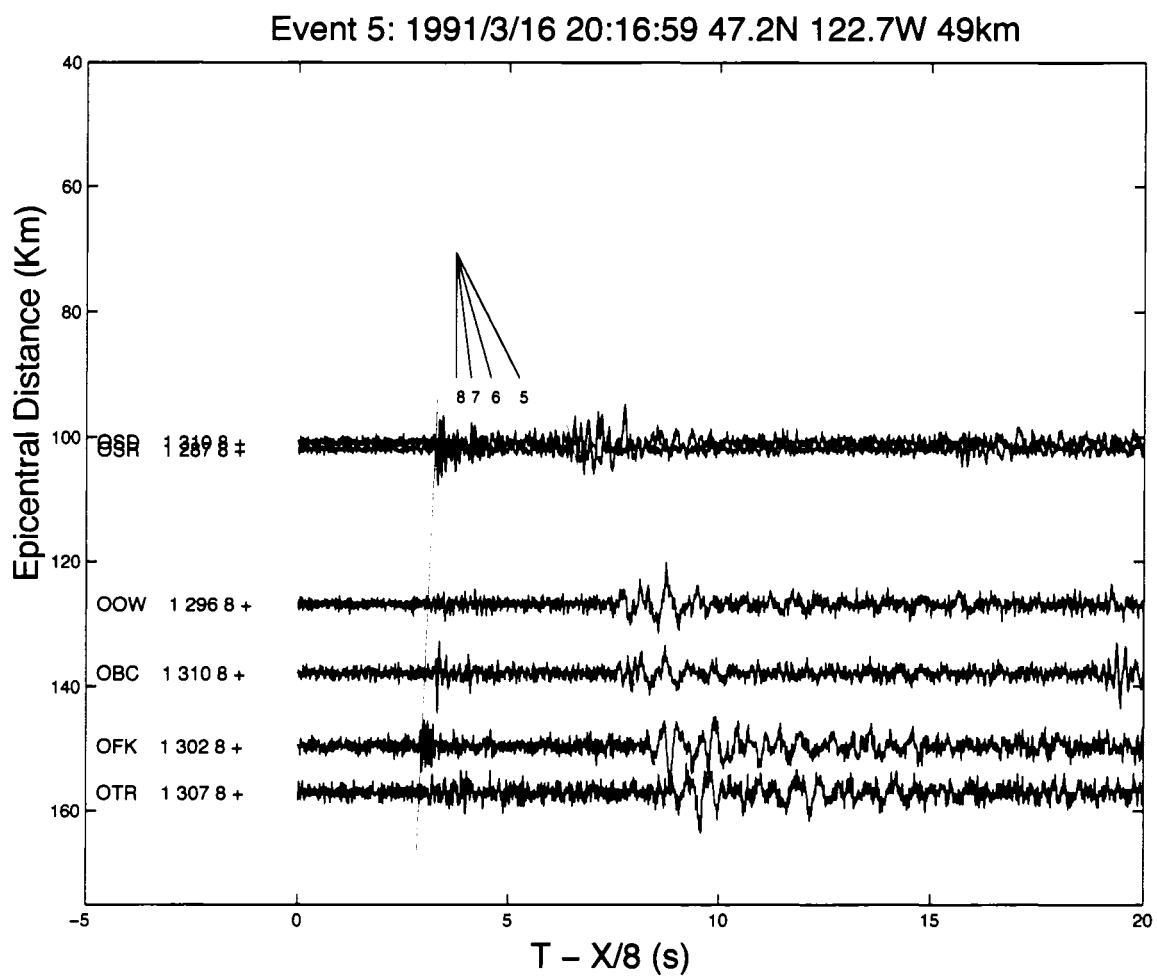
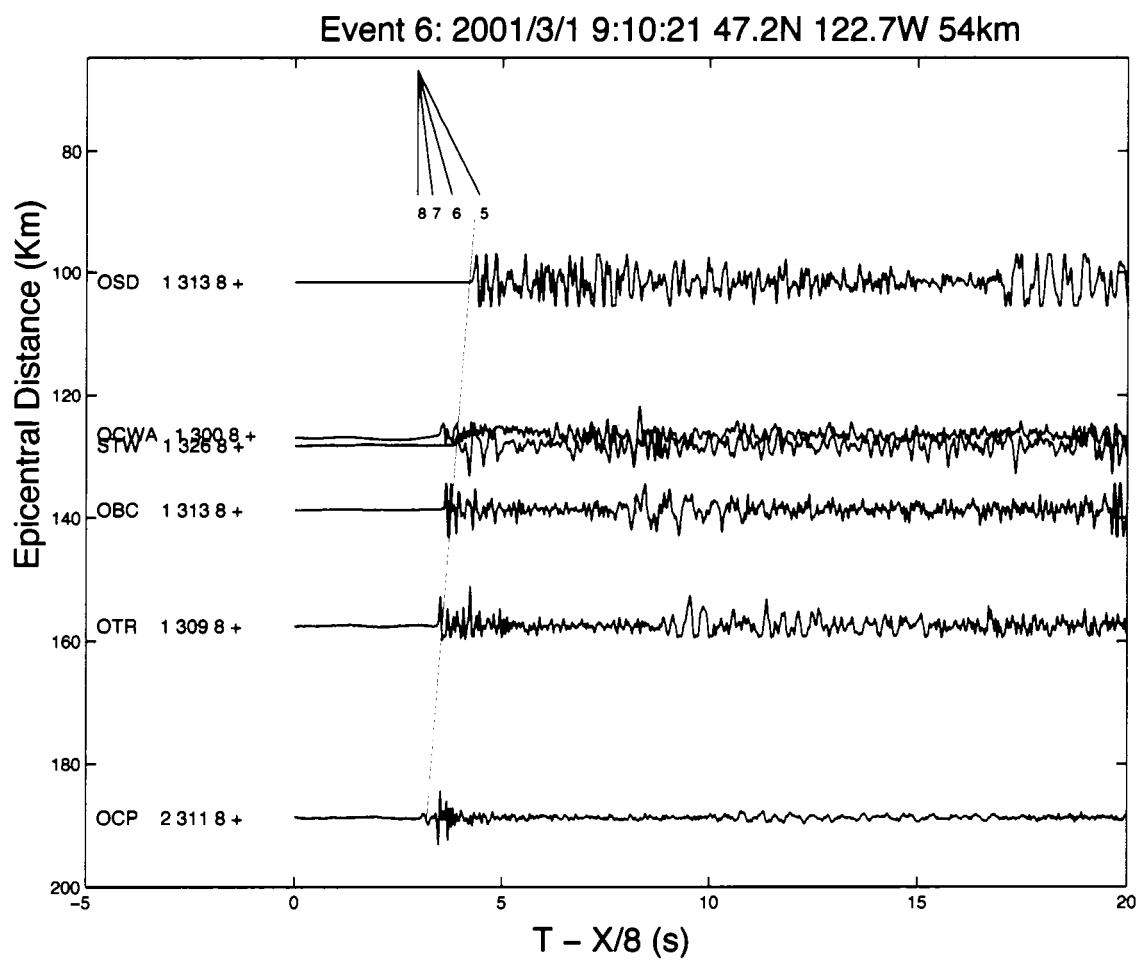

Figure A.5: Event 5: 91031620165
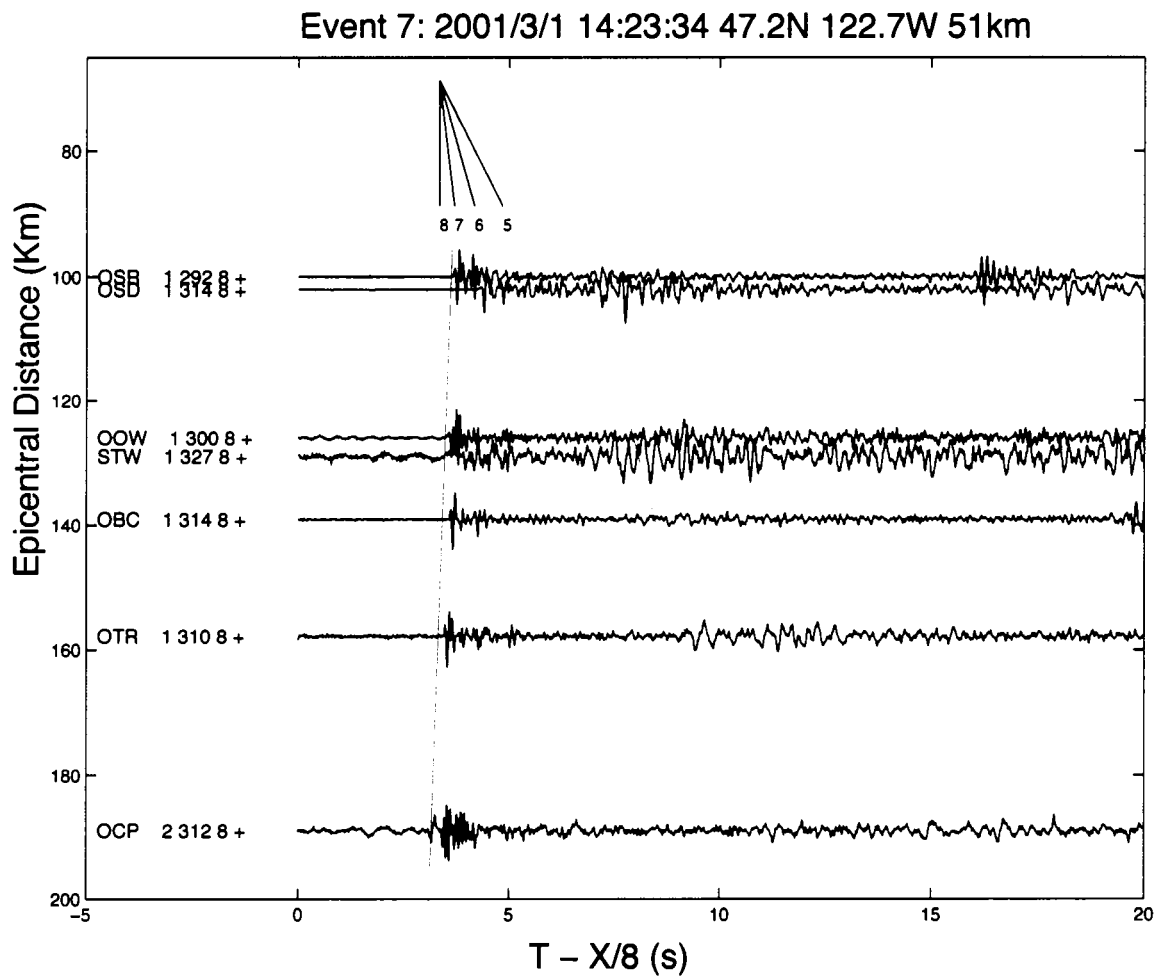
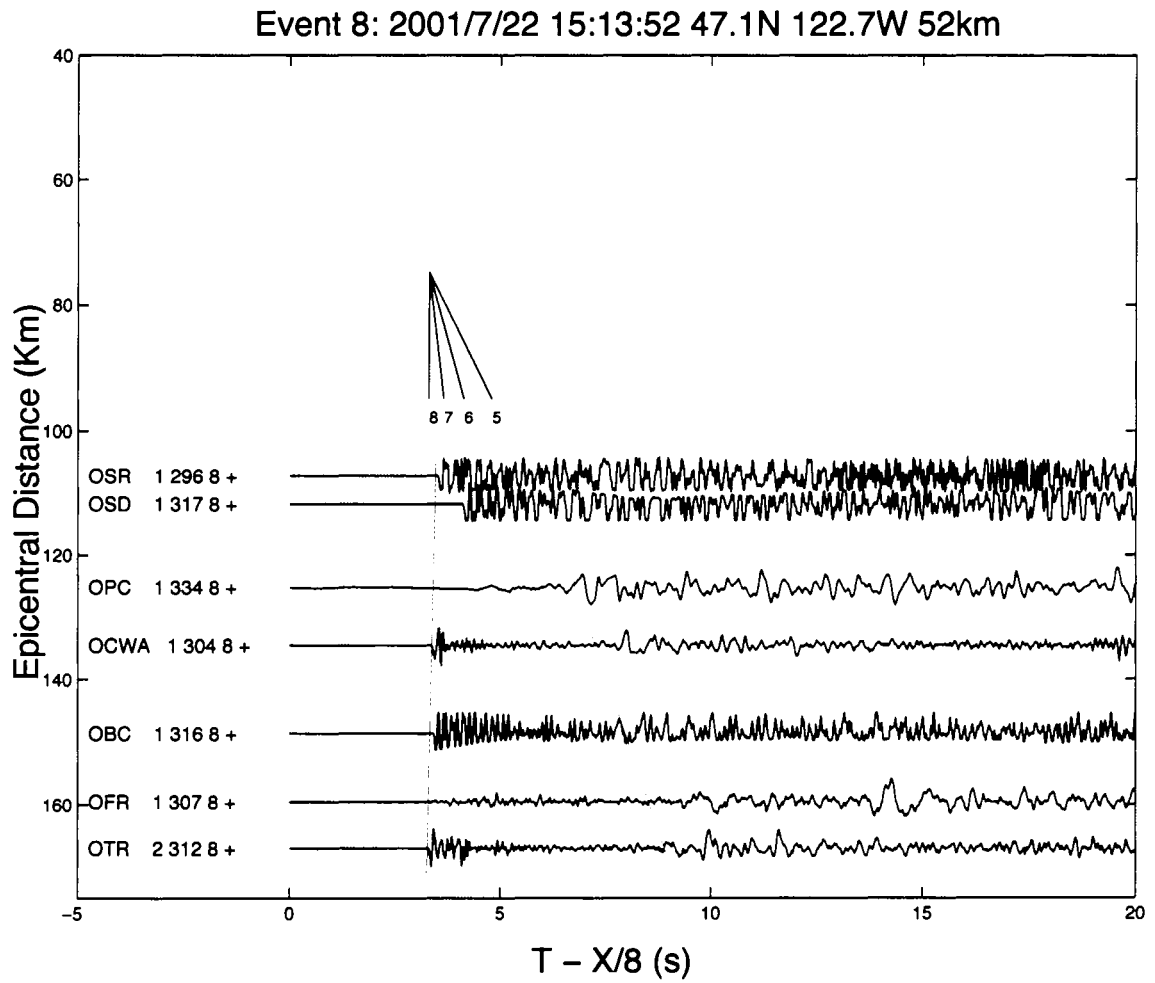Figure A.6: Event 6: 01030109102

Figure A.7: Event 7: 01030114233

Figure A.8: Event 8: 01072215135
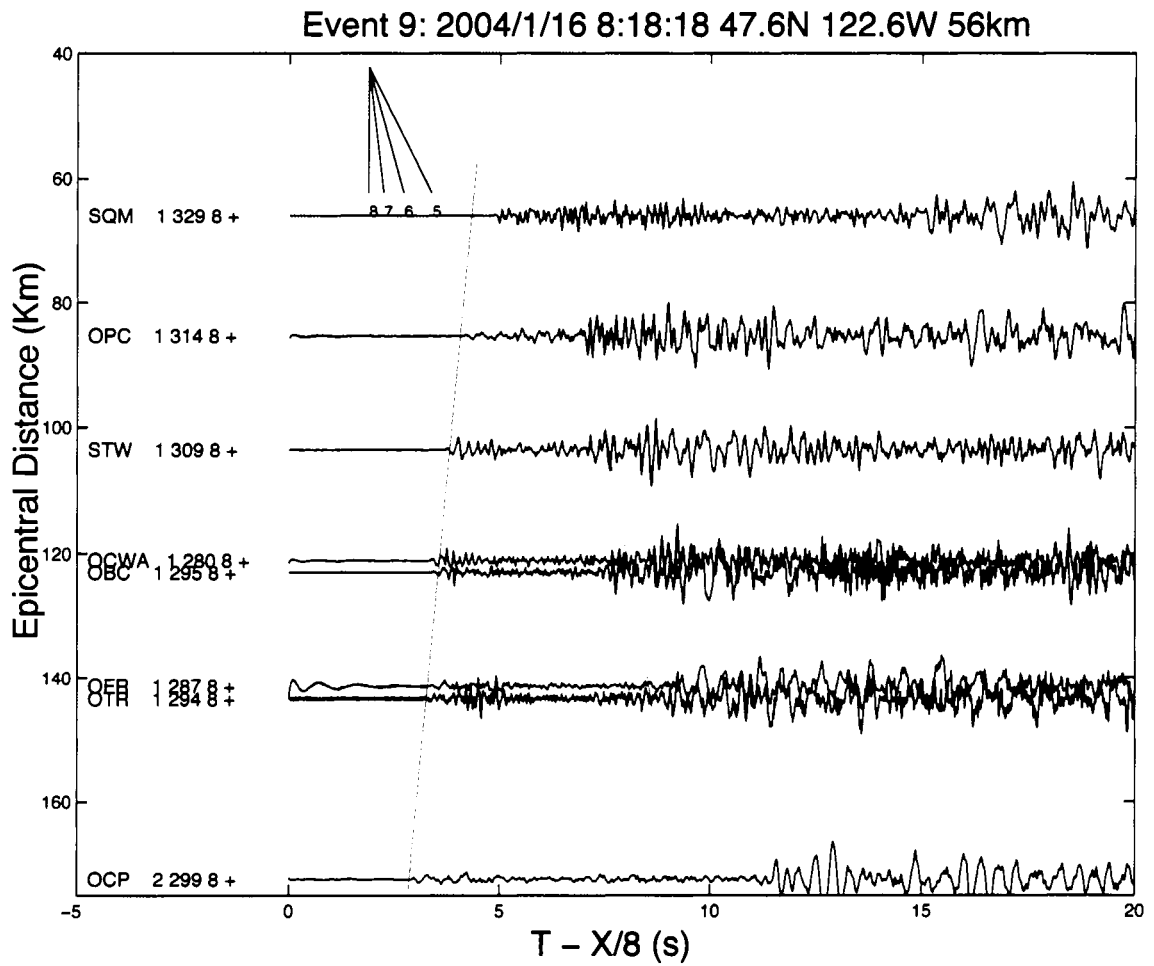
Figure A.9: Event 9: 04011608181
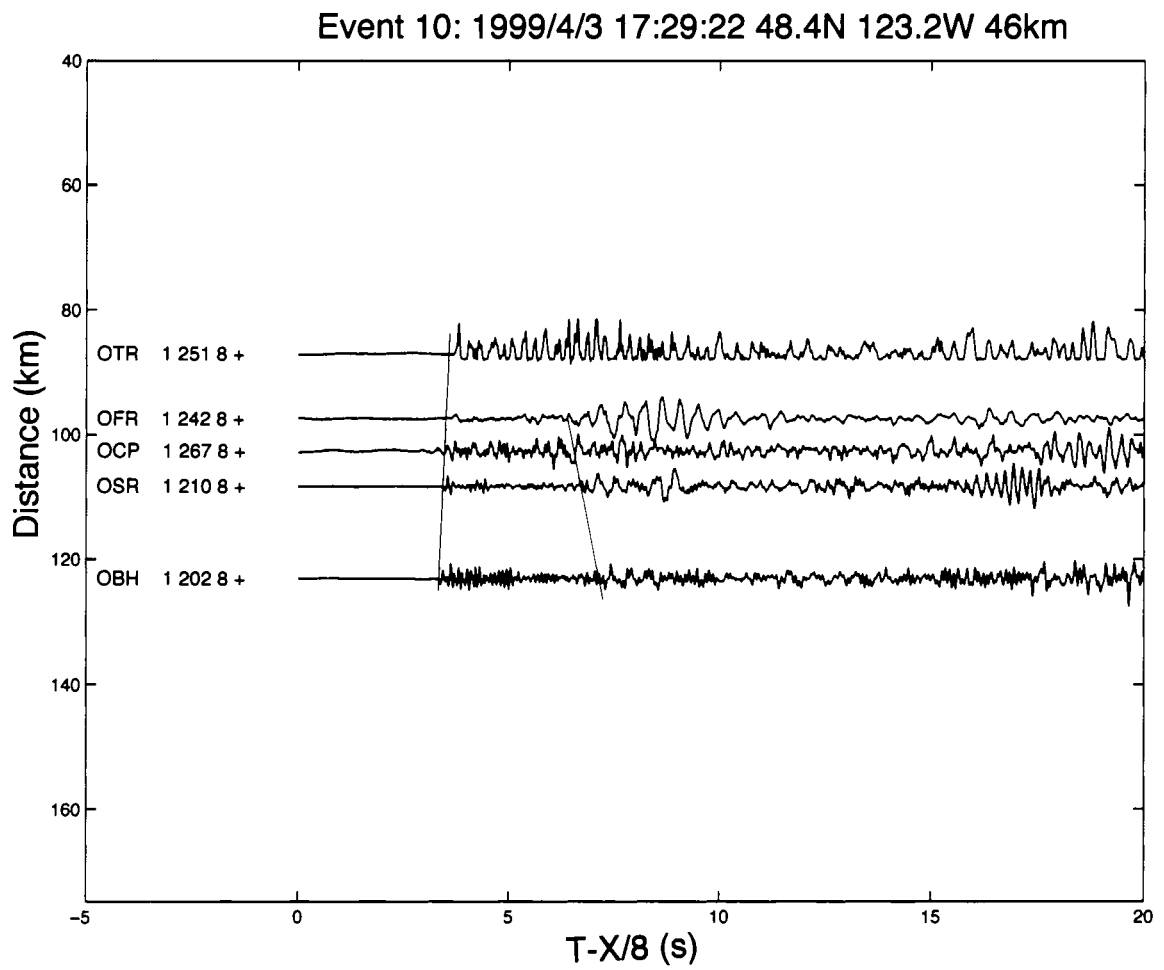
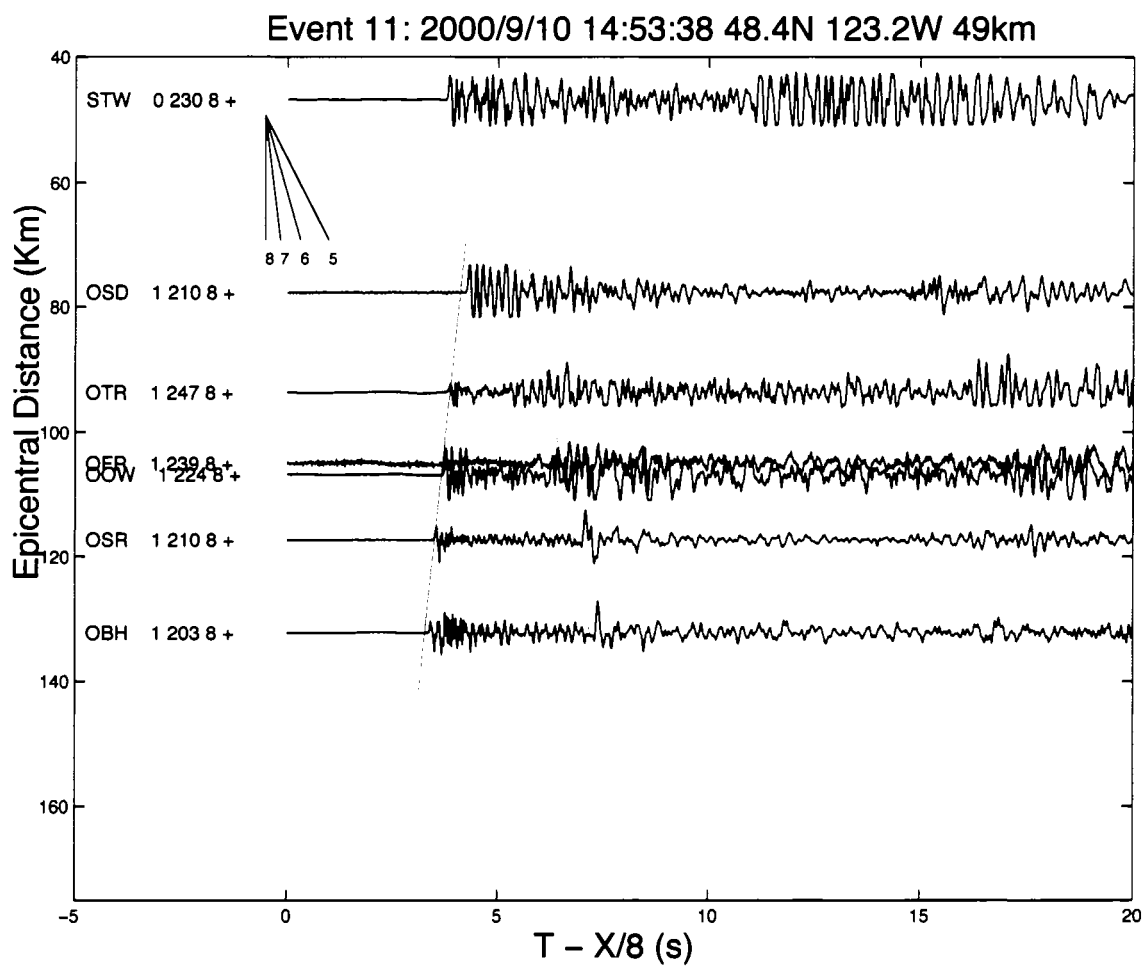Figure A.10: Event 10: 99040317292

Event 11: 2000/9/10 14:53:38 48.4N 123.2W 49km

Figure A.11: Event 11: 00091014533

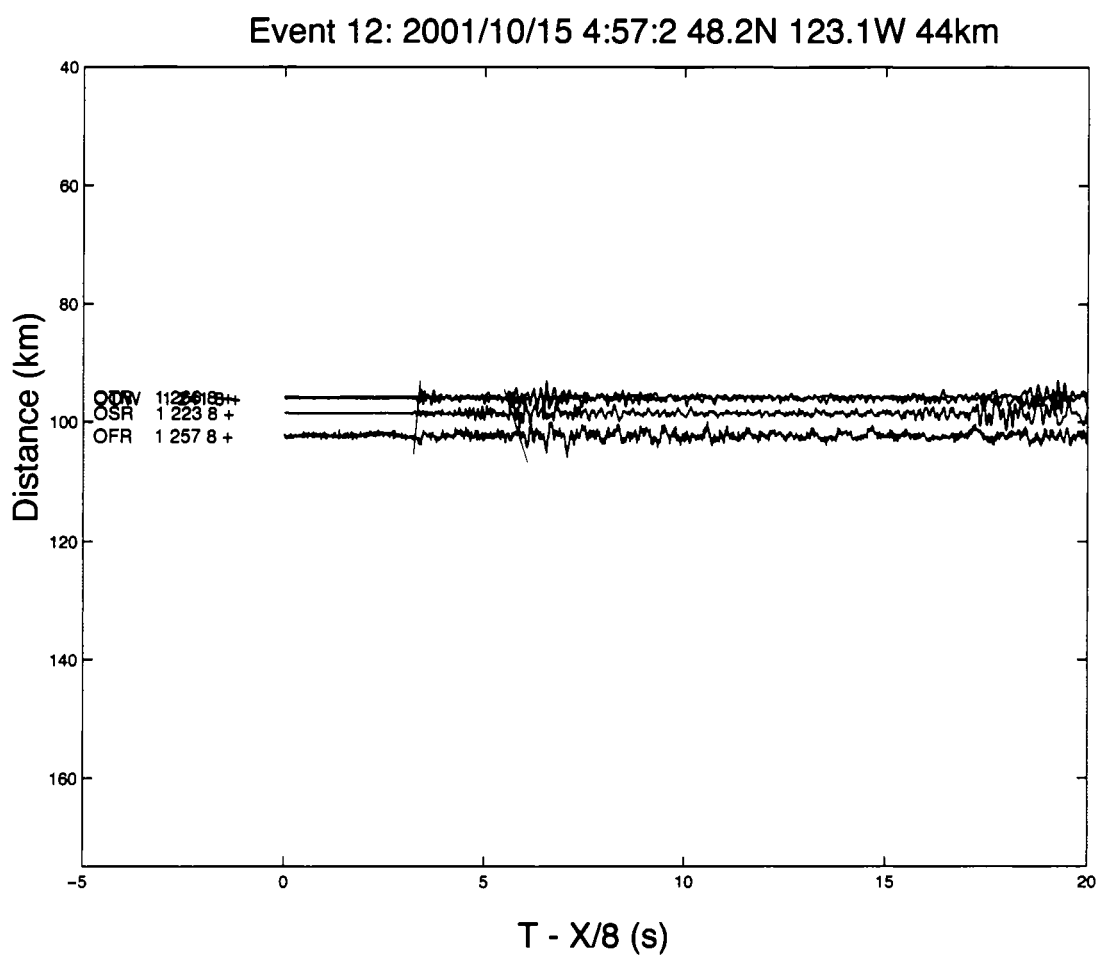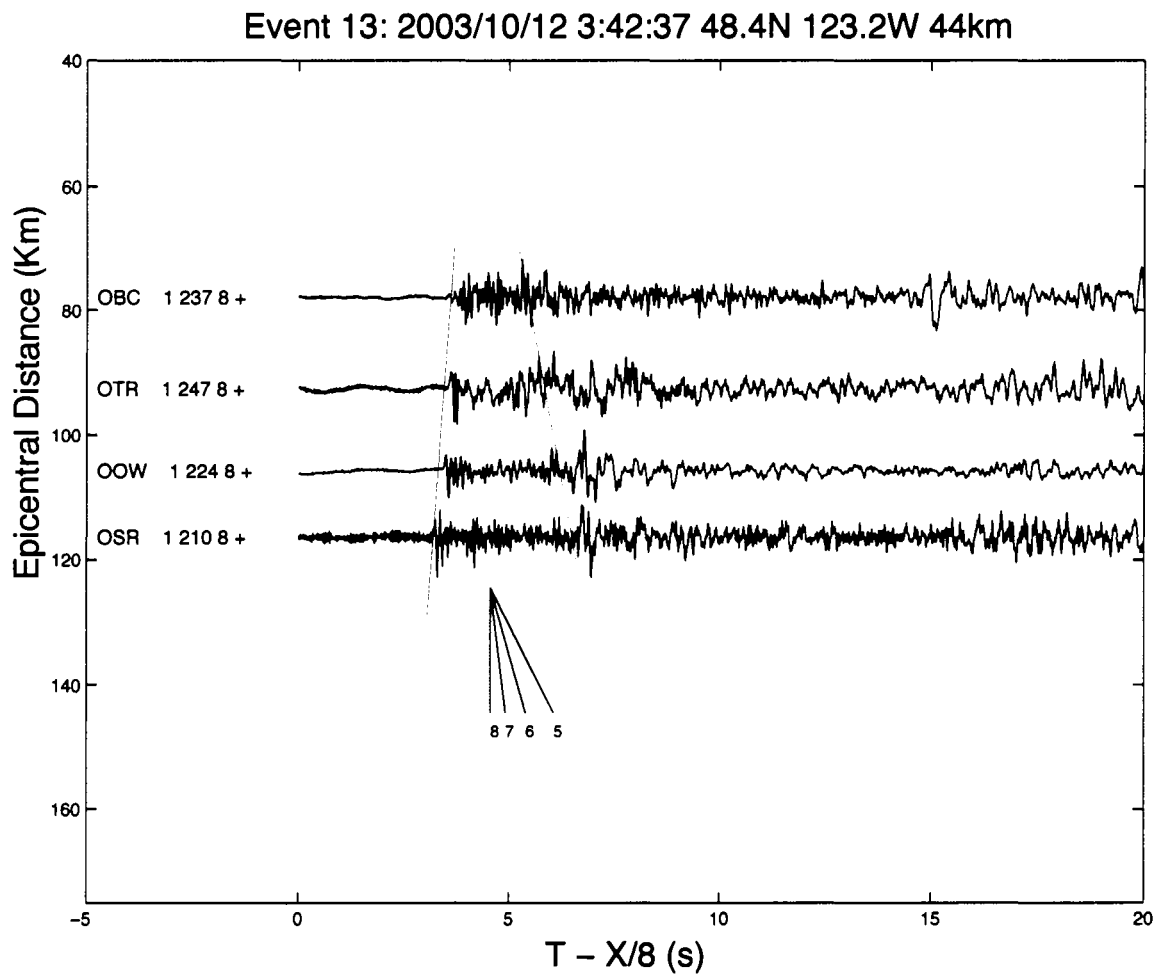Figure A.12: Event 12: 01101504570

Figure A.13: Event 13: 03101203423

VITA

Guy Medema was born in Quincy, Washington. He earned a Bachelor of Science degree in Physics/Astronomy at the University of Washington, Seattle then taught high school math and science for five years. He earned his Doctor of Philosophy in Geophysics at the University of Washington, Seattle. He is currently employed as an exploration geophysicist for the ExxonMobil Corporation in Houston, Texas.